BROADBAND OPTICAL DETECTION OF ULTRAFAST STRAIN WAVES IN METALS

THOMAS J. VAN DEN HOOVEN

BROADBAND OPTICAL DETECTION OF ULTRAFAST STRAIN WAVES IN METALS THOMAS J. VAN DEN HOOVEN 2025

Broadband Optical Detection of Ultrafast Strain Waves in Metals

THOMAS J. VAN DEN HOOVEN

This work was conducted at the Advanced Research Center for Nanolithography (ARCNL), a public-private partnership between the University of Amsterdam (UvA), Vrije Universiteit Amsterdam (VU), University of Groningen (RUG), the Netherlands Organisation for Scientific Research (NWO), and the semiconductor equipment manufacturer ASML.

Broadband Optical Detection of Ultrafast Strain Waves in Metals

ISBN 9789492323781

PhD Thesis, Univeriteit van Amsterdam, 2025

An electronic copy of this thesis is available at: dare.uva.nl & ir.arcnl.nl

Broadband Optical Detection of Ultrafast Strain Waves in Metals

ACADEMISCH PROEFSCHRIFT

ter verkrijging van de graad van doctor
aan de Universiteit van Amsterdam
op gezag van de Rector Magnificus
prof. dr. ir. P.P.C.C. Verbeek
ten overstaan van een door het College voor Promoties ingestelde commissie,
in het openbaar te verdedigen in de Agnietenkapel
op maandag 16 juni 2025, te 14.00 uur

door Thomas Jan van den Hooven
geboren te Geldrop

Promotiecommissie

Promotor:	prof. dr. P.C.M. Planken	Universiteit van Amsterdam
Copromotor:	prof. dr. A.J. den Boef	ASML
Overige leden:	prof. dr. M.D. Ackermann	Universiteit Twente
	prof. dr. D. Bonn	Universiteit van Amsterdam
	dr. G.J. Verbiest	Technische Universiteit Delft
	dr. N.J. van Druten	Universiteit van Amsterdam
	prof. dr. J. van Wezel	Universiteit van Amsterdam

Faculteit der Natuurwetenschappen, Wiskunde en Informatica

CONTENTS

1 Introduction 1
2 Theoretical Background 7
2.1 Generation of Ultrafast Strain Waves 8
2.1.1 Absorption in Thin Metal Layers 8
2.1.2 Temperature Evolution in Thin Metal Layers 11
2.1.3 Thermal Expansion 14
2.2 Optical Detection of Ultrafast Strain Waves 16
2.3 Surface Plasmon Polaritons 16
2.3.1 Excitation of Surface Plasmon Polaritons 17
2.4 White Light Generation 19
3 Experimental Methods 23
3.1 Optical Pump-Probe Measurements 24
3.2 Regenerative Laser Amplifier 25
3.2.1 Electronics of the experiment 26
3.3 Three-stage Optical Parametric Amplifier 27
3.4 Ultrafast Spectrometer 29
3.4.1 White Light Continuum Generation 30
3.4.2 Spectrometer 31
3.4.3 Calibration and Data Processing 33
4 SPP-Enhanced Strain-Wave-Induced Diffraction Changes 37
4.1 Introduction 38
4.2 Experimental setup 39
4.3 White light spectroscopy 40
4.3.1 Reflection 40
4.3.2 First-order diffraction 41
4.3.3 Second-order diffraction 42
4.4 Surface plasmon polaritons 42
4.4.1 SPP coupling to propagating light 43
4.5 Results 44
4.5.1 Reflection measurements 44
4.5.2 Minus first-order diffraction measurements 47
4.5.3 Plus first-order diffraction measurements 49
4.6 Discussion 51
4.6.1 Strain waves 51
4.6.2 Strain-wave-induced reflection and diffraction changes . . . 53
4.7 Conclusion 56
4.A Experimental setup 57
4.B Light coupling to surface plasmon polaritons 58
4.C Transient grating measurement 60
5 Optical Detection of Strain Waves near Optical Resonances 63
5.1 Introduction 64
5.2 Experimental Methods 65
5.3 Results and Discussion 65

5.4 Conclusion 70
5.A Experimental Setup 71
5.B Data Processing 72
5.C S-polarized probe 73
5.D Calculation of reflectance spectrum 74
6 Broadband Optical Detection of Strain Waves in a Thin Ruthenium Film 77
6.1 Introduction 78
6.2 Methods 79
6.3 Results 80
6.4 Discussion 83
6.5 Conclusions 86
6.A Electron dynamics 86
6.B Fourier transform of full time interval 90
6.C Scaling of the longer-wavelength measurement 90

Bibliography 93
Summary 101
Samenvatting 103
Publications 107
Acronyms 109
Acknowledgments 111

1 INTRODUCTION

When picking up an old science fiction book, readers may encounter scenes of people conversing with computers, refrigerators ordering groceries independently, or cars driving themselves. Today, such ideas are no longer fictional. Tools like ChatGPT and other large language models (LLMs) enable natural language interactions, the internet-of-things (IoT) connects everyday objects to the internet and self-driving cars, though not yet ubiquitous, are actively being tested.

These advancements, while seemingly unrelated, share a common foundation: computer chips, also known as integrated circuit (IC). Invented in the 1960s in what is now known as Silicon Valley, ICs rely on the physics of semiconductors such as silicon, hence the valley's name. Despite decades of evolution, the fundamental principles governing transistors have not changed.

One consistent driver of IC development has been scaling. By reducing the size of transistors within computer chips, several advantages are achieved: lower power consumption, increased computational capabilities and a reduced cost per transistor. This has dramatically lowered the cost of computing power and two extremes of this have enabled two of the examples mentioned above.

At one extreme, there are miniscule, low-power chips, with just enough capabilities to enable the IoT. In addition, these chips are cheap to manufacture, allowing many objects to be connected to the internet.

Opposed to that are the massive chips required to train LLMs. One example is the NVIDIA Blackwell B100, which contains 104×10^9 transistors on a single (monolithic) IC [1], measuring an area of over 800 mm^2. These will also cost several tens of thousands of dollars [2] and will consume up to 700 W [3]. The newest data centres will consist of many hundreds of these chips, as the LLMs need ever more parameters to increase their 'intelligence'.

The manufacturing process of chips has been refined over the years, but has not fundamentally changed. They are made in a layer-by-layer process revolving around (photo)-lithography, shown schematically in Figure 1.1. This begins with the deposition of a thin film on a wafer, a circular slab of monocrystalline silicon, followed by a coating of photoresist. This layer chemically changes where it is exposed to specific wavelengths of light. The design for this layer is projected onto it, which is known as the lithographic exposure step. Either the exposed or the unexposed areas are removed, transforming the resist layer into a mask on the underlying thin film. Then, the exposed parts of the thin film can be removed by etching, or ions can be implanted into them, for example. Finally, the remaining resist is removed and the wafer is ready for the next cycle.

The minimum feature size on a chip, also known as the critical dimension (CD), is determined by the smallest feature that can be projected in the lithography tool, which is given by [5]:

$$\mathrm{CD} = k_1 \frac{\lambda}{\mathrm{NA}}, \tag{1.1}$$

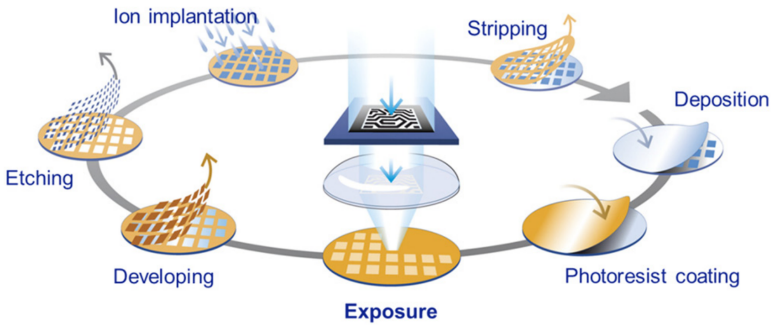

Figure 1.1: The photolithography process which is repeated for all layers in the semiconductor device, from [4].

where λ is the wavelength of the light used, NA is the numerical aperture, and k_1 is a parameter containing many factors related to the lithographic process. This equation is a modified version of the well-known Rayleigh's Criterion [6].

The newest generation of lithography tools, known as extreme ultraviolet lithography (EUVL), uses a wavelength of 13.5 nm, compared to the previous generation's 193 nm, to further decrease the CD. The decrease in wavelength is, unfortunately, accompanied by an increase in k_1 and a decrease in NA. The ultimate reduction in CD was therefore significantly less than the decrease in wavelength would suggest. The decrease in NA is mainly caused by the use of mirrors instead of lenses to focus and guide the light. Lenses cannot be used for light with this wavelength, as all materials absorb this light. Instead, special mirrors are used and, although manufactured to reflect as much of 13.5 nm light as possible, they still absorb about 30 % of the incident light.

Imec's roadmap [7] projects a decrease in CD from approximately 22 nm today to about 18 in 2029. After this, there is only a small reduction in the CD expected, to about 10 nm to 14 nm in 2039, due to the complexity of high-volume manufacturing and because quantum effects are expected to start having an effect. However, the density of transistors on chips is expected to continue to increase in spite of this. This is made possibly by changing the basic design of transistors and by using different materials, such as 2D materials, which allow some features to be closer to each other. For example, the area each transistor occupies can be decreased by stacking the components of the transistor vertically. Although this requires more production steps, the density of transistors can be increased this way, without reducing the CD.

Another important aspect in the lithography process, although not depicted in Figure 1.1, is metrology. In metrology, (parts of) the ICs or the wafer, on which the ICs are produced, are measured. For example, the thickness of layers deposited on the wafer is measured, or the width of the lines produced via the lithographic process. Another type of metrology is *alignment metrology*. Here, the position of the wafer substrate is measured with sub-nanometre accuracy to ensure that the features produced in every new layer are vertically aligned with the previous layers. The position is measured using several so-called alignment markers, which are

phase gratings etched into the wafer substrate during the production of the first product layer.

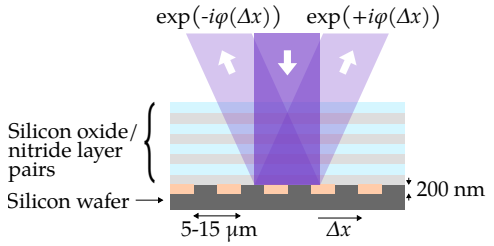

Figure 1.2: Example of a phase grating used for alignment metrology, the grating is buried underneath several (transparent) layers.

A sketch of such a marker is shown in Figure 1.2. The grating period is typically several micrometers, and, on top of the marker, several product layers are shown. The layers are never patterned above the marker, as the marker is placed outside the *die*, the area where the IC is fabricated, in what is called the scribe lane.

The position of the grating is measured using the diffraction orders, of which the plus and minus first order are shown in Figure 1.2. As the grating moves by distance Δx, in the direction perpendicular to the grating lines, as shown in the figure, the phase of the negative and positive order diffracted fields changes. This phase shift is exactly opposite for the negative and positive diffraction of the same order. In the latest lithography tools [4], the relative position of the grating is found by the interference of the negative and positive diffracted fields of the same order. To find the *absolute* position, the Nonius principle can, for example, be used.

In the manufacturing process of computer memory, the manufacturers have already made the switch to a higher-density architecture. Previously, the NAND memory transistors would be fabricated in a matrix on a single layer. Nowadays, the matrix is produced vertically and many of them are stacked next to each other, as is shown in Figure 1.3. The new architecture is therefore called 3D NAND. Today, the total number of layers is about 300 [8], but is expected to exceed 1000 in a few years [9, 10].

The production of 3D NAND is, not surprisingly, more difficult than its 2D predecessor. A critical part in this process is the etching of the vertical channels through the silicon oxide/nitride layers, which is shown schematically in Figure 1.4. To protect the layers, a so-called hard mask is deposited on top of them. This mask is etched very slowly compared to the oxide/nitride layers and is removed where the channels will be etched. This happens via patterning of a resist layer on top of the hard mask, shown in step 1 of the figure. Then, the hard mask is removed where the resist is cleared. In the third step, the silicon oxide/nitride layers are etched only where the hard mask is removed.

Since the channels need to connect to a wire at the bottom, shown in red in the silicon wafer in Figure 1.4, the positioning of the holes in the hard mask needs to be accurate. However, the hard mask is typically opaque, and prevents light from diffracting from the alignment markers. This prohibits accurately determining the position of the alignment markers. In contrast, acoustic waves, or strain waves, are not necessarily hindered and can, in fact, travel through opaque materials. This

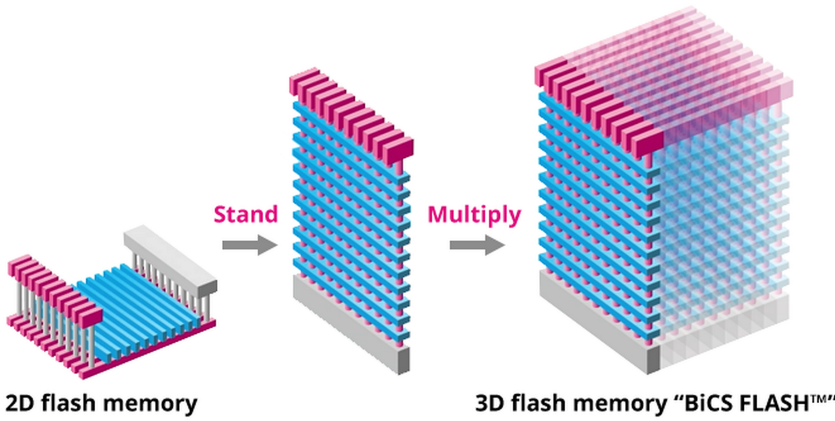

Figure 1.3: Transition of NAND memory from a planar architecture to 3D NAND, from [11].

insight lead to the idea to use light-induced ultrasound [12] to detect the alignment markers buried underneath opaque layers [13, 14].

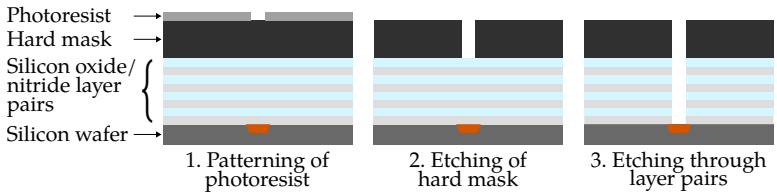

Figure 1.4: Etching of channels in 3D NAND, first the photoresist is patterned, such that a hole can be etched in the hard mask. In the last step, the silicon oxide and nitride layers are etched where the hard mask is removed.

The process is shown in Figure 1.5 and works as follows: First, a femtosecond pulse illuminates the opaque layer and is (partially) absorbed. The absorbed energy heats the opaque layer near the surface, where it starts to expand and generates a strain wave travelling down into the layer stack (panel 1). The strain wave propagates through the layer stack, towards the bottom (panel 2). At the bottom, the strain wave reflects at different times from the grating lines and spaces etched into the silicon wafer substrate (panel 3). In reflecting, the strain wave copies the periodic shape of the marker in its wavefront and the reflected strain wave propagates upward, to the surface. Here, it deforms the surface and, simultaneously, modifies the optical properties. At this moment, a second pulse, known as the probe pulse, can diffract from these modifications, as they have the same spatial periodicity as the alignment marker (panel 4). Ideally, the position of the *buried* grating can thus be determined from the diffraction of the probe pulse.

As shown in [15, 16], this actually works! Unfortunately, the diffraction efficiency from the strain-wave-induced grating is very low. If the diffraction is used to determine the position of the buried grating, it would result in a very rough estimate of the position only, while a very accurate one is required. A better estimate can be made by repeating the procedure and averaging the results. However, this takes

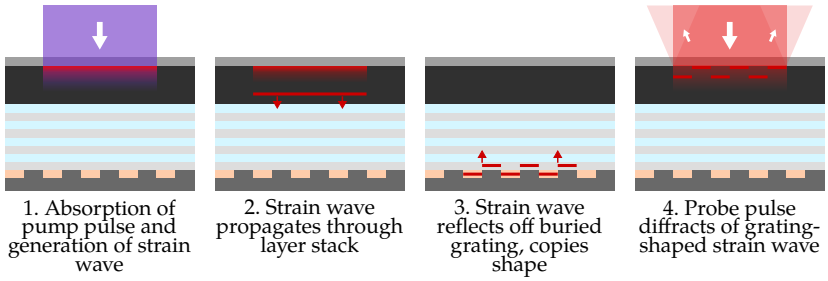

Figure 1.5: The four steps of photoacoustic detection of buried alignment markers: 1. Generation, 2. Propagation, 3. Reflection, 4. Detection.

more time, much more time than is available for the alignment procedure. So, for the photoacoustic detection of buried gratings to be viable, the diffraction efficiency of the probe pulse should be increased.

There are, in principle, several methods to increase the diffraction. First, increasing the strain wave amplitude could be considered. The diffraction efficiency scales quadratically with the changes in reflectance, which, in turn, depends (typically) linearly on the strain-wave amplitude. Thus, a higher strain wave amplitude can significantly improve the diffraction efficiency. However, strain waves are generated through a thermal process–specifically, the thermal expansion of the opaque layer near the surface. Since the pump fluence (energy per unit area) is usually set to be just below the damage threshold, further improvements are limited. Second, the amplitude and shape of the strain wave, its propagation, and its reflection are also determined by the material properties, as is explained in Chapter 2. Unfortunately, these are fixed as the materials used in the production of semiconductor devices cannot be changed solely to enhance photoacoustic characteristics. Consequently, the detection remains as the primary area where significant improvements can be made.

This is, at the same time, a relatively unexplored area of research, as ultrafast photoacoustics has few applications outside science. One of the few parameters that can be changed, is the probe wavelength, making it worth investigating. Another direction that may improve the diffraction is changing the shape of the alignment grating, for example, by segmenting the grating lines into smaller lines and spaces. As was found in earlier work conducted at ARCNL's Light-Matter Interaction group, probing with wavelengths around surface plasmon polariton resonances (SPRs) increases the strain-wave-induced changes in *reflectance* [17].

In Chapter 3, we investigate the changes in reflectance and in *diffraction*, as function of probe wavelength, of a so-called segmented grating. This grating combines a long-period alignment grating with a short-period grating, on which surface plasmon polaritons (SPPs) can be excited. A sketch of such a grating is shown in Figure 1.6. As the resonances of this grating, when covered by a 172 nm layer of gold are fairly narrow, we use an ultrafast probe pulse, tunable in the range 600 nm to 700 nm, in combination with a monochromator consisting of a grating, lens, and slit to detect wavelength-dependent changes in reflectance and diffraction. We find that, in reflection, the changes induced by the longitudinal waves are about a factor of thirty larger when probing with a wavelength close to an SPR compared to a

wavelength further away from the SPR. In diffraction, we find that the strain-wave-induced changes are up to a factor three larger than the changes in reflectance, for the same probe wavelength.

An interesting side note is that this segmented grating can be used to excite *three* SPRs. This is a result from the (amplitude) modulation of the short-period grating by the long-period grating. The modulation leads to sidebands in the spatial frequency domain. It is possible to also excite SPPs on these sidebands, located at the sum and difference spatial frequencies. As a result, the segmented grating exhibits *three* SPRs, at different wavelengths for a single angle of incidence.

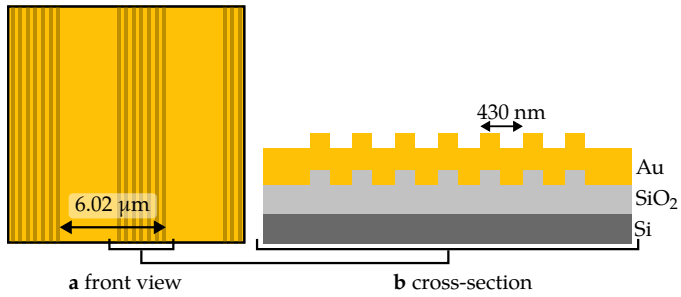

Figure 1.6: a. Front view of the segmented grating as used in Chapter 5. b. Cross-sectional view of the segmented grating. Adapted from Chapter 5 and [18].

However, the single-wavelength detection used in Chapter 4 is rather time-consuming. Hence, we built a spectrometer to simultaneously measure the (strain-wave-induced) changes in reflectance over a broad range of wavelengths. A white light continuum (WLC) pulse is used to probe the sample over this range. The details of this spectrometer, as well as the other parts of the experimental setup, are described in Chapter 3.

We use the new spectrometer in Chapter 5, where we investigate the gold-covered segmented grating, again. In addition to the three SPRs, we investigate also the interband transition (IBT) of gold, at a photon energy of 2.4 eV, corresponding to a wavelength of 520 nm, by probing with wavelengths between 470 nm and 760 nm. We compare the strain-wave-induced changes measured at the SPRs to those measured around the IBT. Surprisingly, the strain-wave-induced changes are comparable in amplitude near the IBT to those near the SPR, but their temporal shape is different. From these measurements, one of our conclusions is that currently the best way to determine the strain-wave-induced changes is to measure them, as the static reflectance spectrum, for example, is not a good predictor of the strain-wave-induced changes in reflectance.

In the last chapter, Chapter 6, we investigate the ultrafast changes in reflectance of a 30 nm ruthenium film. Ruthenium is gaining importance in the semiconductor manufacturing industry. It may replace copper in the future, as the material for thin interconnects [19], which are small connecting wires in a chip. In this chapter, we combine two measurements to compare the strain-wave-induced changes in reflectance over a range of 470 nm to 1000 nm. We find that the maximum strain-wave frequency that can be optically detected is inversely proportional to the penetration depth of the probe wavelength.

2 THEORETICAL BACKGROUND

ABSTRACT

This chapter provides the theoretical background for this thesis. In the first section, we describe generation of strain waves in metal layers. First, the absorption of an ultrashort laser pulse is described and examples of the absorption in ruthenium layers for different wavelengths and different layer thicknesses are shown. Second, the diffusion of energy in and the heating of metals on an ultrafast timescale, following illumination by an ultrashort pulse, is described using the two-temperature model. Also, the model is used to calculate the heating in layers of ruthenium and gold. Third, the heating of the layers causes the layers to expand and generate strain waves, following the elastic wave equation. Using the previously calculated temperature increases, the generation of strain waves is calculated using a forward difference model. Again, the two examples of ruthenium and gold are shown. Additionally, surface plasmon polaritons are introduced, essential to Chapter 4 and Chapter 5. Lastly, the generation of a white light continuum is described, used extensively in the last two chapters of this thesis.

2.1 GENERATION OF ULTRAFAST STRAIN WAVES

ULTRAFAST LASER-INDUCED STRAIN WAVES are generated by rapid heating of the metal after illumination by an ultrashort laser pulse. To understand how and where strain waves are generated, we investigate where in the layer the laser pulse is absorbed, how the absorbed energy diffuses in the layer and how this influences the heating of the layer. The heating of the layer ultimately determines how the strain waves are generated, as explained in the end of this section.

2.1.1 *Absorption in Thin Metal Layers*

We start by investigating the absorption of light in multilayer systems. We only consider linear absorption and ultimately the absorption profile as a function of depth is of interest, which can play an important role in the generation of strain waves.

Let us consider an electromagnetic plane wave perpendicularly incident, from the air side, on a thin metal layer on a (transparent) substrate:

$$E(z,t) = E_0 \exp\left[i(k_0 z - \omega t)\right] + \text{c.c.}, \tag{2.1}$$

where E_0 is the amplitude of the incident field, ω is the angular frequency of the electromagnetic field, $k_0 = 2\pi/\lambda_0$ is the wave number, where λ_0 is the wavelength in vacuum, c.c. stands for complex conjugate, which we need to add to get a *real* electric field. In what follows, we drop it from notation for simplicity. Such a three-layer system is shown in Figure 2.1.

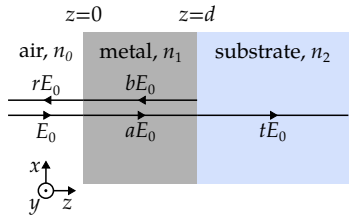

Figure 2.1: Schematic illustration of the three-layer system, the horizontal black arrows indicate the incident, transmitted and reflected fields in the system.

At the air/metal interface, part of the wave is reflected and part is transmitted. In general, the reflection and transmission coefficients, for the electric field, depend on the angle of incidence, the polarization of light, and the optical properties of both media. These coefficients can be calculated via the Fresnel equations [20]:

$$r_s = \frac{n_1 \cos\vartheta_i + n_2 \cos\vartheta_t}{n_1 \cos\vartheta_i + n_2 \cos\vartheta_t}, \text{ and } t_s = \frac{2n_1 \cos\vartheta_i}{n_1 \cos\vartheta_i + n_2 \cos\vartheta_t}, \tag{2.2}$$

$$r_p = \frac{n_1 \cos\vartheta_t + n_2 \cos\vartheta_i}{n_1 \cos\vartheta_t + n_2 \cos\vartheta_i}, \text{ and } t_p = \frac{2n_1 \cos\vartheta_i}{n_1 \cos\vartheta_t + n_2 \cos\vartheta_i}, \tag{2.3}$$

where $t_{s,p}$ and $r_{s,p}$ are the transmission and reflection coefficients for s- and p-polarized light, respectively, $n_{1,2}$ are the (possibly complex) refractive indices of media 1 and 2, respectively, $\vartheta_{i,t}$ are the angles of incidence and transmission,

respectively. In the example above, we assume that the wave is perpendicularly incident on the surface, so that the incident, reflected and transmitted angles are zero, and the coefficients are identical for *s*- and *p*-polarized light.

We can include the reflected field in the notation of the field in air, for $z < 0$:

$$E(z,t) = E_0[\exp(ik_0 z) + r\exp(-ik_0 z)]\exp(-i\omega t), \text{ for } z < 0 \tag{2.4}$$

where the second term describes the wave propagating in the $-z$ direction and r is the reflection coefficient, to which we will come back later. In the metal layer, we can write the transmitted electric field as:

$$E(z,t) = E_0 t_{12}\exp\left[i(k_1 z - \omega t)\right], \tag{2.5}$$

where $k_1 = \tilde{n}_1 k_0 = (n_1 + i\kappa_1)k_0$ is now a complex number, as the layer is absorbing. This means that the amplitude of the electric field inside the layer decays exponentially, as it propagates in the positive z direction, or:

$$E(z,t) = E_0 t_{12}\exp\left(-\kappa_1 k_0 z\right)\exp\left[i(n_1 k_0 z - \omega t)\right]. \tag{2.6}$$

The penetration depth of the electric field, δ_e is defined as the distance it takes for the field to decrease to $1/e$ of its original value, immediately behind the interface. From Equation 2.6, this distance can be easily calculated: $\delta_e = 1/(\kappa_1 k_0) = \lambda_0/(2\pi\kappa_1)$. However, most of the time, we are more interested in the *intensity* of the field, that is the square of the field. The intensity thus decays twice as fast, and the penetration depth for the intensity is half of the penetration depth for the field:

$$\delta_p = \frac{\lambda_0}{4\pi\kappa_1}. \tag{2.7}$$

For the rest of this thesis, we will only use the penetration depth of the intensity, unless explicitly stated otherwise.

Were the metal layer infinitely thick, Equation 2.6 would give us the field inside it, however, we are explicitly working with *thin* layers. So, after distance d, the wave encounters another interface, this time with the substrate, with refractive index n_2. Similar to the first interface, part of the wave reflects and part is transmitted to the substrate. So, the field inside the layer consists of a forward propagating (in the $+z$ direction) and a backward propagating wave.

The total field, both inside the layer and in the substrate, can be written, in general terms, as:

$$E(z,t) = E_0[\exp(ik_0 z) + r\exp(-ik_0 z)]\exp(-i\omega t), \text{ for } z < 0 \tag{2.8}$$

$$E(z,t) = [a\exp(ik_1 z) + b\exp(-ik_1 z)]\exp(-i\omega t), \text{ for } 0 < z < d, \tag{2.9}$$

$$E(z,t) = t\exp\left[i(k_0 z - \omega t)\right], \text{ for } z > d. \tag{2.10}$$

The question remains what the values of the coefficients r, a, b, and t are. For a simple system such as this, consisting of only a few interfaces and layers, one can work out the mathematics by hand. However, for a system which contains many layers, some of them absorbing, and for oblique angles of incidence, this gets complicated very quickly.

One efficient method to calculate the reflection and transmission of the multilayer system, is the transfer-matrix method (TMM) [21, 22]. This method describes every

layer in a multilayer system with a transfer matrix, containing information about the phase the wave accumulates when propagating through the layer (and also the absorption of the wave). Furthermore, it uses the relation between forward- and backward propagating waves in neighbouring layers (say $N-1$ and N), that can be described by [22]:

$$E^b_{N-1} = r_{N-1,N}E^f_{N-1} + t_{N,N-1}E^b_N, \tag{2.11}$$

$$E^f_N = t_{N-1,N}E^f_{N-1} + r_{N,N-1}E^b_N, \tag{2.12}$$

where E^f and E^b the forward- and backward-propagating fields, respectively, where the subscript denotes the layer number.

We use the TMM to calculate the absorption profile as a function of depth in the layer, in ruthenium layers on a sapphire substrate. Using a wavelength of 400 nm, we investigate the absorption in several (thin) layers. For a 30 nm layer of ruthenium, we calculate the absorption profile for several wavelengths. The refractive index of ruthenium, used in the following calculations, was retrieved from [23].

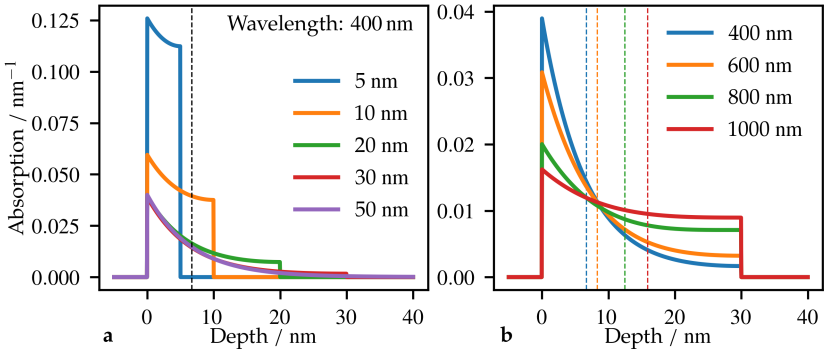

Figure 2.2: a. Absorption of 400 nm light as function of depth in ruthenium, for different layer thicknesses, for normal incidence. The vertical dashed line indicates the penetration depth of 400 nm light in ruthenium, $\delta_p = 6.68$ nm. b. Absorption in a 30 nm ruthenium layer as a function of depth, for different wavelengths. The penetration depths for the different layers are indicated by the vertical dashed lines in the colour of the respective wavelength. Calculated with the Python TMM package based on [22].

In Figure 2.2a, we plot the absorption of 400 nm light as a function of depth, for five layer thicknesses, 5 nm, 10 nm, 20 nm, 30 nm, and 50 nm. The most notable difference between the absorption in the different layers, is that the absorption just behind the air/ruthenium interface differs significantly for the different thicknesses. For a thickness of 5 nm, the absorption is three times as strong near the surface than for a thickness of 50 nm. Since the wavelength of the light is identical, the reflection coefficient for this interface, r_{12}, is also equal for these layers. However, the effect of the reflection from the second interface almost turns the layer into an anti-reflection coating. This can also be seen in the reflectance for the 5 nm layer, listed in Table 2.1, which is much lower than the reflectance of the other layers. Since the penetration depth, shown in the vertical dashed line, is only 6.68 nm, this effect is much less for the 10 nm thick layer, and almost negligible for the thicker

layers. For 50 nm, the absorption almost follows the exponential decay described in Equation 2.5.

In Figure 2.2b, we plot the absorption of a 30 nm thick ruthenium layer, as a function of depth for four different wavelengths, 400 nm, 600 nm, 800 nm, and 1000 nm. For 400 nm, most of the energy is absorbed close to the surface. The absorption profile becomes progressively more flat for the longer wavelengths. This is due to the increasing penetration depth, which is also shown in the figure, by the vertical dashed lines.

Table 2.1: Reflectance, transmittance, and absorbance of different ruthenium layers, for a wavelength of 400 nm. Calculated via the TMM package [22].

Layer Thickness	Reflectance	Transmittance	Absorbance
5 nm	28.0 %	13.6 %	58.4 %
10 nm	51.2 %	4.55 %	44.3 %
20 nm	68.6 %	0.88 %	30.5 %
30 nm	72.7 %	0.20 %	27.1 %
50 nm	73.2 %	0.01 %	26.8 %

So, we have seen that the absorption profile can differ significantly when the metal layer thickness changes, or when the wavelength of the light changes. Both have a distinct effect on the generation and, as we shall see later, on the detection of ultrafast strain waves.

2.1.2 *Temperature Evolution in Thin Metal Layers*

The absorption profile is an important factor in the formation of strain waves. However, it does not explain why the generated strain waves in different metals can be different, even if the absorption profile of the pump pulse is similar. For that, we have to look at the processes in the material, during and immediately after illumination by the pump pulse. In metals, we can describe the heating of the metal following illumination, by the two-temperature model (TTM).

The TTM [24, 25] separates the metal into two coupled subsystems: the free electron gas and the metal lattice. In the model, the absorbed energy is initially deposited into the free electron gas, where the deposited energy density follows the absorption profile of the metal. As a result, the electron gas heats up, which drives the two subsystems out of the initial thermal equilibrium in two ways. First, the electron gas temperature now depends on the position in the layer. Second, the electron gas temperature is now, for most of the layer, higher than the lattice temperature. The energy subsequently starts to redistribute (i) within the electron gas, via electron gas energy diffusion, (ii) to the lattice, via electron-phonon coupling. In the second process, energy is transferred to the lattice by collisions between electrons and lattice vibrations.

In one dimension, this can be written in two coupled equations:

$$C_e(T_e)\frac{\partial T_e}{\partial t} = \frac{\partial}{\partial z}\left[\kappa_e(T_e, T_l)\frac{\partial T_e}{\partial z}\right] - G(T_e - T_l) + S(z,t), \tag{2.13}$$

$$C_l\frac{\partial T_l}{\partial t} = G(T_e - T_l), \tag{2.14}$$

where $T_{e,l}$ are the temperatures of the electron gas and lattice, respectively, where the dependence on both z and t is omitted in our notation, $C_{e,l}$ is the heat capacity of the electron gas and lattice, respectively, κ_e is the electron thermal conductivity, G is the electron-phonon coupling constant and $S(z,t)$ is the absorbed laser energy density. The electron gas heat capacity is calculated by $C_e(T_e) = A_e T_e$, with A_e a constant, and the electron heat conductivity as $k_e(T_e, T_l) = k_0 T_e/T_l$. Typically, the electron gas and lattice temperatures are calculated using a finite difference method.

Before we show some results, it is important to realize that the TTM is only a model and has some limitations. First, it assumes that both electron gas and lattice are *thermalized*, meaning that they can have a temperature assigned to them. This is not always valid. Especially the electron gas cannot be described by the Fermi-Dirac distribution immediately after illumination. Second, ballistic motion of hot electrons is not included in the model, which can underestimate the depth to where energy can penetrate near-instantaneously. This mostly effects s/p-band metals [25], such as Au, Ag or Cu.

As an example, we show the evolution of the electron gas and lattice temperatures in ruthenium and gold layers, after illumination by a 400 nm, 60 fs FWHM pulse. For ruthenium, the pulse fluence is 10 mJ cm^{-2}, while in gold the fluence is 5 mJ cm^{-2}. Despite the difference in incident fluence, the *absorbed* energy in both metals is similar, as gold absorbs about 60 % at 400 nm, and ruthenium about 30 %. Both layers are 100 nm thick and the substrate, in both cases, is sapphire. The layers are thick enough that the absorption profile is almost an exponentially decaying function, as discussed earlier. Ruthenium and gold are chosen as examples, not only since they are investigated in the later chapters of this thesis, but also since they could not show a more different response to the pulse. The electron-phonon coupling constant in ruthenium is namely almost a factor of 100 larger than in gold. The (material) parameters used in the calculation of the TMM are listed in Table 2.2.

The electron gas and lattice temperatures at the surface of the ruthenium and gold layer are shown in Figure 2.3a and b, respectively. For the ruthenium layer, the electron gas temperature rises rapidly as the pulse illuminates the layer. After that, it starts to decay quickly, transferring its energy to the lattice. The lattice temperature starts to rise, and after about 1.5 ps, the lattice and electron gas temperature are in equilibrium at the surface, at about 800 K.

In gold, the electron gas temperature also starts to increase as the pulse illuminates the surface. However, this temperature peaks at about 4000 K, much higher than for ruthenium. After the peak, the electron gas starts to decay, but much slower than in ruthenium. The transfer rate of energy from electron gas to the lattice in gold is quite low, due to its much lower electron-phonon coupling constant, compared to ruthenium. At 15 ps, the electron gas and lattice are almost in thermal equilibrium. Lastly, the peak just after illumination, where the electron gas, for a short time,

Table 2.2: Parameters used in TTM calculation, all constants are taken from [26], except the refractive indices. These were interpolated at 400 nm, from [23] and [27], for ruthenium and gold, respectively.

Parameter	Unit	Ru	Au
Pulse fluence, F_0	$\mathrm{J\,m^{-2}}$	100	50
Electron-phonon coupling constant, G	$\mathrm{W\,m^{-3}\,K^{-1}}$	185×10^{16}	2.3×10^{16}
Electron specific heat constant, A_e	$\mathrm{J\,m^{-3}\,K^{-2}}$	400	71
Lattice heat capacity, C_l	$\mathrm{J\,m^{-3}\,K^{-1}}$	2.95×10^{6}	2.51×10^{6}
Electron heat conductivity, k_0	$\mathrm{W\,m^{-1}\,K^{-1}}$	117	317
Refractive index at 400 nm, $\tilde{n}$	-	2.4 + 4.6i	1.4 + 2.0i

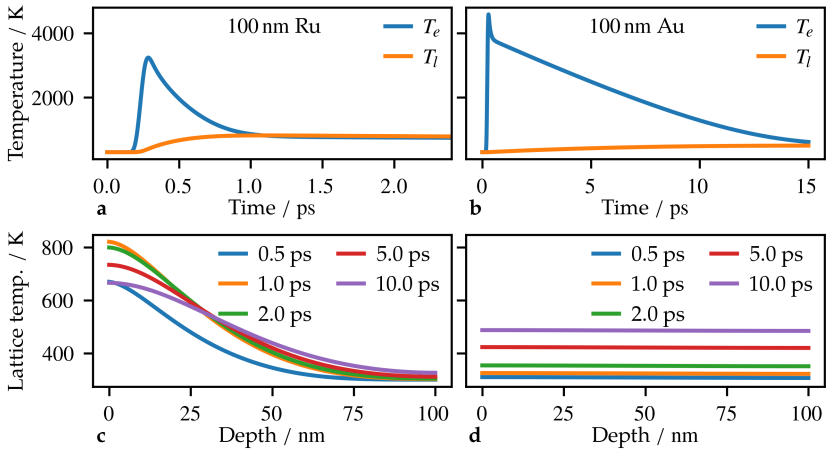

Figure 2.3: a. Calculated electron gas and lattice temperatures of a 100 nm ruthenium layer, illuminated by a 400 nm, 60 fs pulse with a fluence of 10 mJ cm^{-2}. b. Same as a. for a 100 nm gold layer, illuminated by similar pulse but with a fluence of 5 mJ cm^{-2}. c. Lattice temperature for the ruthenium layer, as function of depth, for several times. d. Same as c. but for the gold layer.

reaches a temperature over the 4000 K, is an artefact of the TTM not modelling the ballistic electrons. If these are taken into account, it disappears [25].

In Figure 2.3c and d, we plot the lattice temperature as a function of depth in the ruthenium and gold, respectively, for several times after excitation. For ruthenium, already at 0.5 ps, the lattice temperature has increased drastically. Near the surface, the temperature is then already above 600 K, and decreases as a function of depth almost like an exponential decay. This reflects the absorption profile of the 400 nm pulse. At 1 ps, the temperature at the surface peaks, and for later times, the energy starts to diffuse throughout the layer. For gold, at 0.5 ps, the temperature has hardly increased, for any position in the layer. At 5 ps, the temperature has reached 400 K, but is almost constant as a function of depth in the layer. This is due to the low electron-phonon coupling constant in combination with a high electron heat conductivity. Since the energy transfer rate from the electron gas to the lattice is low,

it takes quite some time. During this time, the energy deposited into the electron gas redistributes itself throughout the layer, such that the electron gas temperature is almost constant as a function of depth. Then, the energy is transferred to the lattice, which heats up more or less homogeneously as a function of depth.

The results show that, for some materials such as gold, the absorbed energy is distributed within the electron gas rapidly, such that the lattice of the layer heats up more or less homogeneously. For other materials, such as ruthenium, the increase in lattice temperature follows the absorption profile of the laser pulse more closely.

2.1.3 *Thermal Expansion*

As soon as the lattice heats up, it expands. Since the lattice is a solid material, we can use the elastic equations to describe its motion. When we assume that the layer is heated uniformly in the directions perpendicular to the layer interfaces, and that the layer is isotropic, we can write the elastic equations as [12]:

$$\sigma_{33} = (\lambda + 2\mu)\, B\eta_{33} - 3B\beta\Delta T_l(z,t), \tag{2.15}$$

$$\rho\frac{\partial^2 u_{33}}{\partial t^2} = \frac{\partial \sigma_{33}}{\partial z}, \tag{2.16}$$

where σ_{33} is the stress in the z-direction, λ is the first Lamé parameter, μ the shear modulus, B the bulk modulus, η_{33} the strain in the z-direction, β the linear expansion coefficient, $\Delta T_l(z,t)$ the temperature increase of the lattice, ρ the density of the material, and u_{33} the displacement in the z-direction. The first equation shows that the stress on an infinitesimal small slice of the layer consists of the term proportional to the strain of the slice, and of a term proportional to the change in temperature. The second equation is a modification of Newton's second law. The right-hand part indicates the net stress, which is force per area, on this slice, whereas the left part is its mass (in the form of density) and the acceleration of its displacement. Lamé's first parameter, λ, the shear modulus, μ, and the speed of sound, v_s, can be calculated via:

$$\lambda = 3B\frac{3B - E}{9B - E}, \tag{2.17}$$

$$\mu = \frac{3B - E}{6B}, \tag{2.18}$$

$$v_s = \sqrt{\frac{\lambda + 2\mu}{\rho}} \tag{2.19}$$

where B is the bulk modulus, E is the Young's modulus, and ρ is the density.

At a free interface, the stress is zero, since the interface is free to move. At an interface with another material, the stress and the displacement are continuous over the interface.

Now, we shall consider the strain waves generated in the layers of ruthenium and gold, with the lattice temperatures as shown previously in Figure 2.3. The strain has been calculated using Equation 2.15 and Equation 2.16 using a forward difference method. The increase in temperature is determined by subtracting the initial temperature, 300 K, from the lattice temperatures shown earlier. The strain is calculated from the displacement using $\eta_{33} = \partial u_{33}/\partial z$. Both the surface and the

back interfaces are considered to be free to move, i.e., the stress is zero at those interfaces. In Table 2.3, we list the elastic properties for ruthenium and gold that were used in the simulation.

Table 2.3: Elastic properties of ruthenium and gold, used to calculate the strain wave. Values from [28].

Parameter	Unit	Ruthenium	Gold
Young's modulus, E	GPa	447	78
Bulk modulus, B	GPa	220	220
Linear expansion coefficient, β	-	6.4×10^{-6}	14.2×10^{-6}
Density, ρ	$\mathrm{kg\,m^{-3}}$	12.37×10^{3}	19.3×10^{3}
Speed of sound, v_s, from literature	$\mathrm{m\,s^{-1}}$	5970 [29]	3240 [30]
Speed of sound, from Equation 2.19	$\mathrm{m\,s^{-1}}$	6207	3377

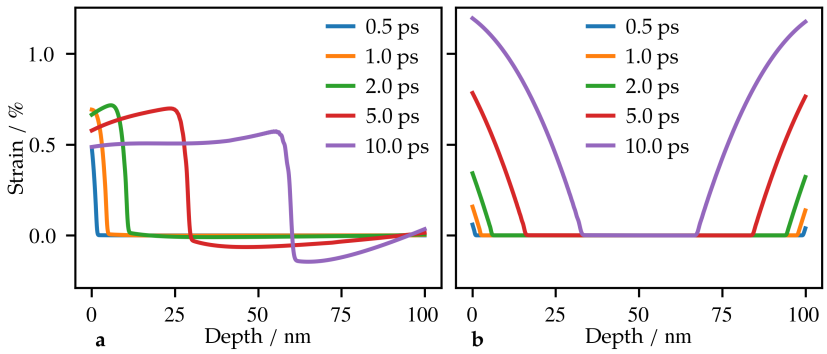

Figure 2.4: a. Strain in a 100 nm ruthenium layer, calculated from the lattice temperatures shown in Figure 2.3. b. Same for a 100 nm gold layer.

In Figure 2.4a and b, we plot the calculated strain in the ruthenium and gold layers, respectively, as a function of depth at several times after illumination by the 400 nm pulse. In the ruthenium layer, a single strain wave is generated at the surface. Already at 0.5 ps, the strain at the surface is almost 0.5 %. This is the result of the rapid heating of the lattice, at the surface, due to the strong electron-phonon coupling, in combination with the zero stress condition there. This implies namely that the strain is proportional to the increase in (lattice) temperature.

The shape of the strain wave is most clearly visible at 10 ps. Here, the strain of the leading part (at a larger depth) is negative, which means that the lattice is compressed, compared to its initial state. This is followed by expansion of the lattice.

In the gold layer, the strain has a radically different profile. Not one, but *two* strain waves are generated, from both the surface and the back interface, that is also assumed to be free to move. Two waves are generated because the layer heats up more or less homogeneously as a function of depth. The heating also happens at a slower rate, compared to ruthenium, resulting in a less steep strain profile,

although it is partially compensated by the lower speed of sound. The lower speed of sound can also be observed by viewing the sharp bend of the strain wave, which is, at 10 ps in gold at a depth of about 32 nm, while in ruthenium it is deeper, at about 60 nm. These positions are exactly where they should be, taking into account the speeds of sound listed in Table 2.3.

In conclusion, we have seen that the absorption profile of the (pump) pulse, but also the electron-phonon coupling and the thermal conductivity of the metal determine, for a large part, the characteristics of the strain wave(s) that is generated.

2.2 OPTICAL DETECTION OF ULTRAFAST STRAIN WAVES

Strain affects the optical properties of materials. This is typically modelled as a linear relation between change in the refractive index and the strain:

$$\tilde{n}(\eta) = \tilde{n}_0 + \frac{\partial \tilde{n}}{\partial \eta}\eta, \tag{2.20}$$

where $\tilde{n}_0$ is the static refractive index, η is the strain and $\partial\tilde{n}/\partial\eta$ is commonly referred to as the 'strain-optic' coefficient. Not surprisingly, the strain-optic coefficient, just as the refractive index itself, depends on the optical wavelength.

In opaque materials, the change in refractive index can only be detected if the strain wave is close to the surface, when it is at a distance from the surface, that is shorter than the penetration depth of the detection wavelength. Then, the change in refractive index (slightly) changes the reflection of light, reflecting from that surface.

If the strain-optic coefficient and the strain wave are known, the change in reflectance can be calculated via, for example, the TMM. For that, the layer, or a volume near its surface, is divided into many thin slices. The thicknesses and refractive indices of these slices are modified by the strain wave as it propagates in this volume. The TMM is then used to calculate the change in reflectance. However, strain-optic coefficients are, in general, not known. If they are known, then they typically have been obtained only for a single wavelength, by fitting of the change in reflectance, of a calculated strain wave, to the measured change in reflectance, using the strain-wave coefficient as the fitting parameter. For most materials, the coefficients as a function of wavelength are not known, unfortunately.

2.3 SURFACE PLASMON POLARITONS

Surface plasmon polaritons (SPPs) are quasiparticles where collective oscillations of the free electron gas of a metal (plasmons) are coupled to an electromagnetic wave, near the surface of a metal (interfacing with a dielectric). They are a solution to the wave equation for electromagnetic waves, where the electric field decays exponentially as a function of distance away from the interface of a metal (or conductor) and a dielectric (typically air). A schematic illustration of an SPP is shown in Figure 2.5

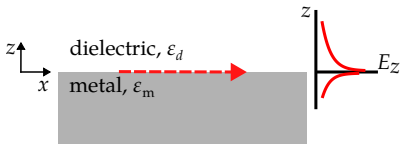

Figure 2.5: Schematic illustration of an SPP, also the amplitude of the electric field in the z-direction is shown, which decays exponentially as a function of the distance away from the interface.

The field of an SPP propagating along the surface, such as shown in Figure 2.5, is given by [31]:

$$\mathbf{E}_j = \begin{pmatrix} E_{j,x} \\ 0 \\ E_{j,z} \end{pmatrix} \exp\left(ik_x x - i\omega t\right) \exp\left(ik_{j,z} z\right), \text{ where } j = d, m \tag{2.21}$$

where $\mathbf{E}_{d,m}$ indicates the electric field in the dielectric or metal, respectively, $E_{j,x}$ and $E_{j,z}$ denote the electric field amplitude in both media in the x and z-directions, respectively, k_x is the wave vector in the x-direction, ω is the angular frequency of the field, and $k_{j,z}$ is the wave vector in the z-direction, in both media. There is no component in the y-direction. A full derivation can be found elsewhere [31–33]. The components of the wave vectors are given by:

$$k_x^2 = k_0^2 \frac{\epsilon_d \epsilon_m}{\epsilon_d + \epsilon_m}, \tag{2.22}$$

$$k_{j,z}^2 = \epsilon_j k_0^2 - k_x^2 = \frac{\epsilon_j^2}{\epsilon_d + \epsilon_m} k_0^2, \text{ where } j = d, m, \tag{2.23}$$

where $k_0 = 2\pi/\lambda_0 = \omega/c$ is the wave number in vacuum, $\epsilon_{d,m} = \epsilon'_{d,m} + \epsilon''_{d,m} i$ the (complex) dielectric function of the dielectric and metal, respectively, at the angular frequency ω. If we assume a real angular frequency ω, a dielectric with $\epsilon''_d = 0$, and that $\epsilon''_d < |\epsilon'_d|$, then we can write the x-component of the wave vector in a real and imaginary part:

$$k'_x = k_0 \sqrt{\frac{\epsilon'_m \epsilon_d}{\epsilon'_m + \epsilon_d}}, \tag{2.24}$$

$$k''_x = k_0 \left(\frac{\epsilon'_m \epsilon_d}{\epsilon'_m + \epsilon_d}\right)^{3/2} \frac{\epsilon''_m}{2\left(\epsilon'_m\right)^2}. \tag{2.25}$$

The real part is typically referred to as k_{SPP}, and we would like to note that $k_{\text{SPP}} > k_0$ by the assumptions we made earlier. Also, the existence of the *imaginary* part of k_x means that also the amplitude of the field of the SPP decays in the direction of propagation. This is due to Ohmic losses of the electron oscillations [31], which result in heating of the metal.

2.3.1 *Excitation of Surface Plasmon Polaritons*

To excite SPPs, we need light with both the same optical frequency as the SPP we want to excite, and the same wave vector. The first is a consequence of the conser-

vation of energy and the second a consequence of the conservation of momentum, when we want to transfer energy from light to an SPP. Furthermore, the incident electric field should contain a component which is polarized perpendicular to the metal surface. As we have seen, the wave number of the SPP is larger than the wave number of light *propagating* in the air. However, we can create evanescent waves with that wave vector, although they cannot propagate far and cannot carry energy. If the wave vector of such an evanescent wave matches that of the SPP, then the evanescent wave can transfer energy from the incident light to the SPP.

There are several ways to generate such an evanescent field, and thus to excite SPPs. The first two involve creating an evanescent field using the total internal reflection (TIR) of a prism, shown schematically in Figure 2.6. The most common is the Kretschmann geometry, where a thin metal layer is deposited on the interface of a prism where the TIR is. This layer should be thin enough so that the evanescent wave has not completely decayed, but actually extends beyond the layer, into the air (or dielectric). However, the layer should also be thick enough such that the SPP is not significantly affected the (refractive index of the) prism. In other words, the field of the SPP should not penetrate too far into the prism. The second method that involves a prism, is the Otto geometry, where there is an air gap between the prism and a flat metal layer. In this case, the evanescent wave does not have to penetrate through the metal and the metal can be (infinitely) thick. However, the air gap has to be in the order of several hundreds of nanometres, and should be constant.

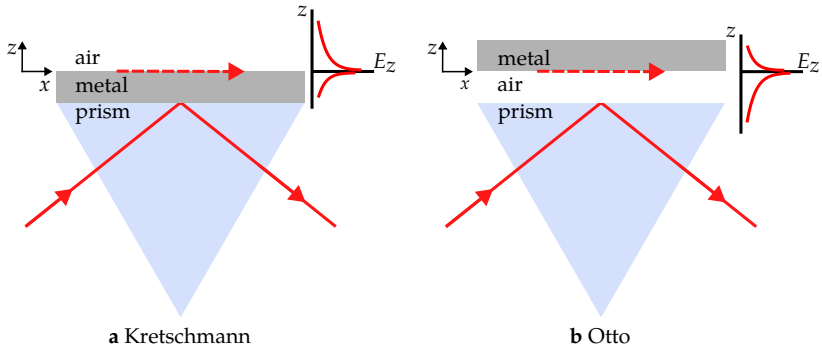

a Kretschmann **b** Otto

Figure 2.6: a. Kretschmann geometry, the SPP (red dashed arrow) is generated at the air/metal interface, by the TIR of the light in the prism. Also, the amplitude of electric field of the SPP perpendicular to the interface, E_z, is schematically indicated. b. Otto geometry, the SPP is generated at the air/metal interface, located a short distance from the surface of the prism is generated at the air/metal interface, by the TIR.

A third method to excite SPPs does not involve a prism, but instead relies on the near-field diffraction of a grating. Consider an electromagnetic wave, with $k_0 = 2\pi/\lambda_0$, incident on a metallic grating with period Λ, at angle ϑ with respect to the surface normal, as shown in Figure 2.7. The projection of the wave vector along the surface is denoted as $k_x = k_0 \sin\vartheta$. Near the grating, the field is modulated by the grating, with grating vector $k_{\text{grating}} = 2\pi/\Lambda$. Due to this modulation, the field near the grating also contains the sum- and difference spatial frequencies of k_x and

k_{grating}, or integer multiples of k_{grating}. If any of these new spatial frequencies equal the wave number of the SPP, i.e., if:

$$k_{\text{SPP}} = k_x \pm m k_{\text{grating}}, \tag{2.26}$$

then SPPs are excited on the grating.

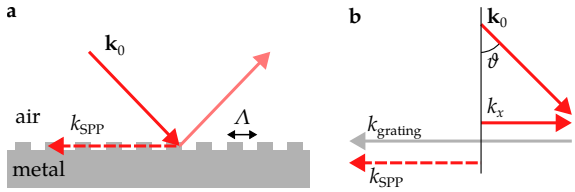

Figure 2.7: a. Illustration of coupling between light incident on the grating, with period Λ, and an SPP. b. Schematic depiction of the wave vectors of the incident light, grating vector and the SPP.

The opposite also happens, in other words, energy from the SPPs can also be coupled back to propagating light, which will be in the same direction as the reflection. However, part of the energy of the SPPs is lost due to Ohmic losses, so the reflectance is always lower than without SPPs. This is typically how SPPs are identified. Since only *p*-polarized light can excite SPPs, the difference in reflectance compared to *s*-polarized light can reveal surface plasmon polariton resonances (SPRs).

2.4 WHITE LIGHT GENERATION

In this section, the basic theory behind the generation of the white light continuum (WLC) is described. These broadband, but still short, pulses are used in this thesis to probe the change in reflectance over a broad wavelength range simultaneously. The implementation of WLC pulses in the setup is described in Section 3.4.1. This section also contains the spectra of WLC pulses generated in various crystals.

White light continuum (WLC) generation is a phenomenon where an ultrafast laser pulse is spectrally broadened in a medium. The broadened pulse is still coherent and its spectrum can span several octaves. The resulting spectrum also depends on the optical properties of the medium, such as the absorption of the medium for certain wavelengths.

There are multiple non-linear optical processes involved in the generation process. The optical Kerr effect, a third-order non-linear process, plays an important role. This effect describes the change in refractive index as function of intensity of incident light, via the non-linear refractive index n_2:

$$n(I) = n_0 + n_2 I, \tag{2.27}$$

where n_0 is the linear refractive index, and I is the intensity of the light. The non-linear refractive index is related to the third-order nonlinear susceptibility by [34]:

$$n_2 = \frac{3}{4 n_0^2 \epsilon_0 c} \chi^{(3)}, \tag{2.28}$$

where ϵ_0 is the vacuum permittivity, and c is the speed of light in vacuum. Here, we have dropped the dependence of n_0 and $\chi^{(3)}$ on the frequency of the incident light, ω. Note that n_2 itself also depends on the frequency. Typical values for the n_2 in solids that are used for WLC generation are in the order of $10^{-16}\,\mathrm{cm^2\,W^{-1}}$. In other words, we need a sufficiently high intensity beam for the non-linear refractive index to have an effect.

Let us consider pulses with a Gaussian spatial and temporal profile. The full-width at half maximum (FWHM) in time and space are denoted as τ and d, respectively. The intensity, as a function of position, r and time, t, can be written as:

$$I(r,t) = I_0 \exp\left(-4\ln(2)\frac{r^2}{d^2}\right)\exp\left(-4\ln(2)\frac{t^2}{\tau^2}\right), \tag{2.29}$$

where I_0 denotes the peak intensity. The refractive index change depends linearly on the intensity and will follow the same Gaussian spatial and temporal profile. This has several effects on the properties of the pulse.

Due to the Gaussian spatial profile, the centre of the beam, where the intensity is the highest, experiences a higher refractive index than the edges of the beam (considering a positive n_2). As a result, the central part accumulates more phase than the sides, slowing the phase front in the middle, leading to self-focussing. The phenomenon also used for mode-locking in laser oscillators.

Only at a particular laser power the beam starts to self-focus, and depends on material parameters and the wavelength of the light. The threshold power can be calculated using [35]:

$$P_{\mathrm{crit}} = \frac{3.8\lambda^2}{8\pi n_0 n_2}, \tag{2.30}$$

where λ is the wavelength of the light. When the power of a pulse exceeds this threshold, the focussing leads to a self-focus some distance away. After that distance, the light would collapse to a singularity. However, this does not happen as there are many processes counteracting the self-focussing. In solids, the main processes are group velocity dispersion and plasma defocussing. These effects get stronger when the intensity increases as the beam self-focusses. At some point, there is a balance between the self-focussing and defocussing effects. The beam will keep the same radius for some distance. This is called filamentation. In solids, a filament can be several millimetres long, with a diameter of several micrometers.

During filamentation, the Gaussian temporal shape of the pulse changes due to the Kerr effect. This effect, called self-steepening, causes the pulse to become shorter in time. The front and trailing part of the pulse experience a lower refractive index (and group index) than the centre of the pulse and therefore propagate faster. As a result, the trailing part will catch up with the centre and a steep slope forms at the end of the pulse.

Finally, for white light generation, the intensity-dependent refractive index is crucial as it leads to the phenomenon of self-phase modulation (SPM) Since the intensity is also time-dependent, the pulse will experience a refractive index changing in time. The phase ϕ of an electric field, with a Gaussian temporal intensity profile, propagating in a medium with nonlinear refractive index n_2, can be written as [36]:

$$\phi = -\omega_0 t + kz = -\omega_0 t + \frac{2\pi L}{\lambda}(n_0 + n_2 I(t)), \tag{2.31}$$

where ω_0 is the central frequency, k the wave vector, z the propagation distance, L the length of the nonlinear medium.

The instantaneous angular frequency is given by the time-derivative of the phase:

$$\omega = -\frac{\partial \phi}{\partial t} = \omega_0 - \frac{2\pi L n_2}{\lambda} \frac{\partial I(t)}{\partial t}. \tag{2.32}$$

It follows that lower frequencies are generated at the front of the pulse, while higher frequencies are generated after the peak amplitude of the pulse. Typical WLC spectra have an asymmetric spectrum, this can be explained by the different temporal shape due to the self-steepening effect [37].

3 EXPERIMENTAL METHODS

ABSTRACT

This chapter describes the experimental techniques and equipment used in this thesis. The general principle of ultrafast pump-probe experiments, that forms the foundation of this work, is explained. The Astrella amplified laser system, used to generate the high-energy fs pulses, and the optical parametric amplifier, used to change the central wavelength of the ultrashort pulses, are described. In the later experiments, we use a home-built transient reflection spectrometer, that used a white light continuum probe pulse to measure the (strain-wave-induced) changes in reflectance over a broad wavelength range simultaneously. Finally, the hardware of the spectrometer, its calibration and data processing, and the generation of the white light continuum pulse are described.

3.1 OPTICAL PUMP-PROBE MEASUREMENTS

THE MAJORITY OF experimental results, in this thesis, is obtained via pump-probe measurements. This powerful technique uses two optical pulses to investigate the ultrafast optical response of materials. The first, more intense pulse, known as the 'pump' pulse, excites the sample. A second, weaker pulse, known as the 'probe' pulse, is delayed by a controlled amount of time and is used to measure the sample's response. By varying pump-probe delay, the dynamic changes in the optical response can be measured. Depending on the experimental geometry, either the reflection, transmission, or diffraction (or a combination of them) of the probe pulse is measured by a detector.

One of the advantages of this technique is that the detector used does not need to be particularly fast, as the time resolution of the experiment is primarily determined by the probe pulse duration. Therefore, this technique is ideal for the investigation of ultrafast phenomena.

This method implicitly assumes that the effect of every pump pulse is identical. In that case, the experiment (using one pump and one probe pulse at a fixed delay) can be repeated indefinitely. Typically, thousands of experiments are averaged to increase the signal-to-noise ratio (SNR). However, this fails when the sample has not returned to its original state when a new pump pulse arrives. This can happen when the pump pulse permanently alters (damages) the sample, or when the sample has not cooled completely during the time between pump pulses. That will lead to the accumulation of heat and ultimately to permanent damage.

Figure 3.1a illustrates a simple pump-probe measurement setup. A pulsed laser generates a pulse train that is split into a 'pump' and 'probe' by a beam splitter. One part is frequency-doubled in a nonlinear optical crystal, and pumps the sample. The path length of this part, and thus the arrival time of the pulses, can be adjusted via the mechanical delay stage. The part transmitted by the beam splitter probes the sample. In this example, the wavelengths of the pump and probe pulses are different, hence a colour filter can easily separate the probe light from the pump light. This is useful, for example, to suppress randomly scattered pump light from entering the probe light detector.

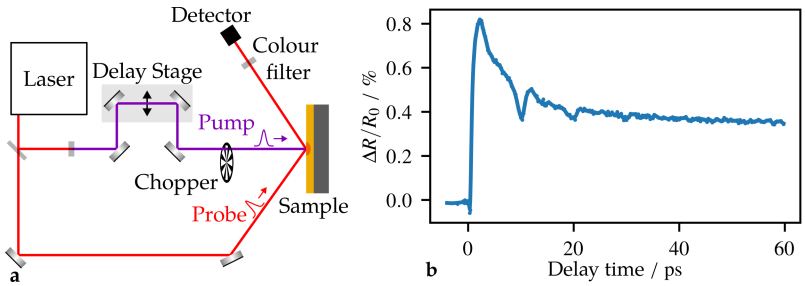

Figure 3.1: a. Illustration of pump-probe reflectance experiment. A colour filter prohibits any pump light from reaching the detector. b. Time-dependent changes in reflectance of a 30 nm ruthenium layer on sapphire, measured with a 400 nm pump pulse, and a 710 nm probe pulse.

Typically, the repetition rate of pump pulses is modulated by a mechanical chopper, so that the probe alternately samples an unperturbed, and a pumped sample. Lock-in detection can then be used to further increase the measurement sensitivity.

The time-dependent response is measured by changing the delay between the pump and probe pulse. At each delay, many probe pulses are measured and averaged, enabling the measurement of minute changes in the optical properties of the sample. Typically, the path length of either the pump pulse or the probe pulse is changed by moving the position of two mirrors, as shown in the figure. While this allows for very small steps in path length, resulting in small adjustments in delay time, the mechanical movement can also lead to a changing beam position at the sample, which is undesired.

Methods to vary the optical delay between pump and probe pulse without mechanical parts have been developed to address these issues. One of them is asynchronous optical sampling (ASOPS) [38], which uses two lasers, one for the pump pulses and another for the probe pulses, running at slightly different repetition rates. As it does not require a mechanical delay line, this method does not suffer from beam pointing issues when measuring longer delay times.

Figure 3.1b shows the result of a typical pump-probe measurement. For negative delays, the probe pulse arrives at the sample earlier than the pump pulse. Hence, it does not see any pump-induced change if the time between two consecutive pump-probe pair is sufficiently long for the previous pump (and probe) energy to dissipate. At $t = 0$, there is a rapid change in probe reflectance as the pump pulse is absorbed by the free electrons of the (metallic) sample. As explained in Section 2.1, the absorbed energy is transferred from the electron gas to the lattice. This results in lattice heating and expansion, and the generation of a strain wave, all giving rise to changes in the reflectance. The lattice cools on a nanosecond timescale, resulting in a slowly decaying thermal background. The strain-wave-induced changes in reflectance are superimposed on those caused by thermal effects. The strain waves can be observed as rapid changes in the reflectance at 10 ps and 20 ps.

3.2 REGENERATIVE LASER AMPLIFIER

The laser system (Astrella, Coherent) generates ultrashort, high-energy pulses by amplifying chirped pulses [39] from a laser oscillator, within a regenerative cavity. Figure 3.2 illustrates the components in the laser system and the electronics controlling them. The output pulses of an 80 MHz Ti:sapphire oscillator (Vitara-S, Coherent) are first stretched in a grating stretcher. The pulses are then directed into a Z-shaped cavity (not shown in the figure) by reflecting them off the Ti:sapphire crystal, that will amplify the pulses later.

The pulses are incident at the Brewster angle of the crystal, but are also reflected as they are *s*-polarized relative to the crystal interface (vertical in the frame of the laser). The first Pockels cell traps a single pulse in the regenerative cavity, by switching on before a pulse passes through it. During the first pass of the pulse, the cell changes the polarization to circular. The pulse reflects off the cavity end mirror and passes through the Pockels cell again, while the cell remains switched on. This second pass changes the pulse's polarization back to linear, but now it is rotated by 90° compared its original polarization (i.e. horizontally polarized). The cell is then switched off, trapping the pulse inside the cavity. The pulse, still

incident at the Brewster angle at both interfaces of the crystal, is now transmitted without reflection losses into the Ti:sapphire crystal.

In the meantime, the Nd:YAG laser is pumping the crystal, so that the pulse is amplified with each pass through the crystal. The pulse makes twelve round trips in the cavity, before the second Pockels cell is switched on. Similar to the first Pockels cell, it rotates the pulse's polarization by 90°. As a result, the polarizing beam splitter directs the now vertically polarized pulse into the compressor. Here, the pulse is compressed to its original pulse length of 35 fs, but with a significantly higher pulse energy of 6 mJ.

The timings of the Pockels cells and the Nd:YAG laser are controlled by the Synchronous Delay Generator (SDG). It receives an 80 MHz signal from the oscillator and sends out several 1 kHz signals synchronized with this. The delays of the 1 kHz outputs can be adjusted individually. The SDG also triggers the camera and the data acquisition by the analog-to-digital converter (ADC) in the computer.

The 6 mJ pulses generated by the Astrella are split into two by a beam splitter, reflecting about 85 % and transmitting the rest. The stronger, reflected part is used to pump a three-stage optical parametric amplifier (OPA) (see Section 3.3), and is ultimately used as probe.

The weaker, transmitted part is used to pump the sample. The second harmonic of this, with a wavelength of 400 nm, is generated in a β-barium borate (BBO) crystal. Several dichroic mirrors, reflecting 400 nm and transmitting 800 nm, remove any residual 800 nm light. A mechanical chopper, locked to a 1 kHz output of the SDG, blocks every other pulse, reducing the repetition rate to 500 Hz. A computer-controlled mechanical delay line varies the arrival time of the pump pulses with respect to the probe pulses, by changing the path length experienced by the former.

3.2.1 *Electronics of the experiment*

The most important electronic components, and the connections (in black lines) between them, of the setup are also shown in Figure 3.2. A 1 kHz output of the SDG triggers the electronics, such that they can measure the probe pulse. However, the Andor Zyla camera and the ADC (PCI-6281, National Instruments), reading out the photodiodes, need to be triggered at different times. The camera, when triggered, starts its acquisition for a set duration. To measure the probe pulse, it needs to be triggered *before* that pulse arrives at the sensor. In contrast, the photodiodes only produce a non-zero voltage, for some short time, *after* the pulse has reached their active areas. Hence, the ADC needs to be triggered later than the camera. Lastly, from the measured spectra, it is nearly impossible to determine if the sample was either pumped or unperturbed, so this also needs to be logged.

In the experiment, these tasks are handled by a trigger box, custom-built by the AMOLF electronic engineering department. This is done as follows: the box is first triggered by the SDG, a few μs before the laser pulse is amplified in the Astrella. Then, if the chopper is in its desired state (either on or off), the trigger box outputs a square wave with a 10 μs pulse duration. The rising edge of this pulse triggers the Andor camera and the falling edge triggers the ADC. The (probe) laser pulse is emitted and should be arriving at the camera and photodiodes within this interval as is shown in the inset in Figure 3.2.

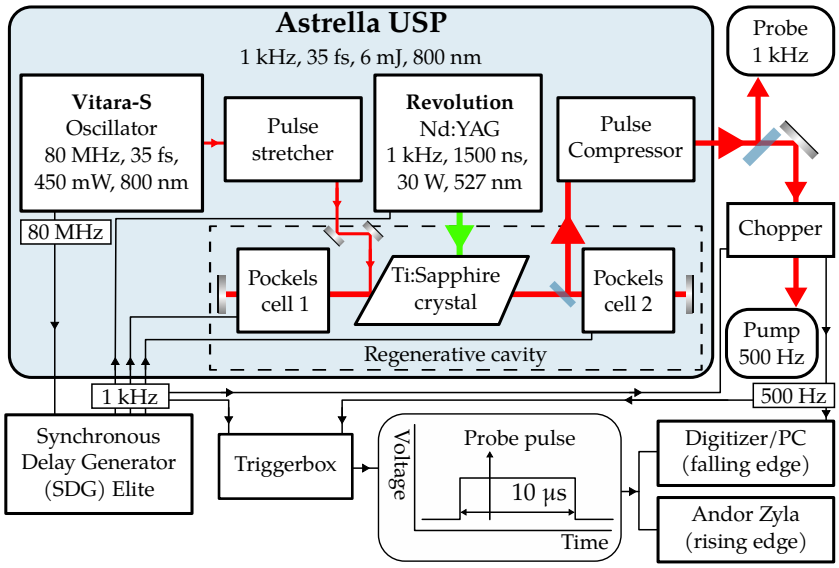

Figure 3.2: Illustration of the Astrella laser system and the electronics controlling the laser and triggering the setup. The voltage-time diagram indicates the square wave that triggers the Andor Zyla camera on the rising edge and the digitizer on the falling edge. The laser pulse arrives at the camera and the photodiodes during the trigger pulse width.

In the experiment, typically 2000 laser pulses are measured consecutively. The first pulse will always measure the same state of the sample, either pumped or unperturbed and the following pulses will be alternating between these states. This means that all the even measured pulses will have the same state, making the data processing easier.

3.3 THREE-STAGE OPTICAL PARAMETRIC AMPLIFIER

The optical parametric amplifier (OPA) converts the high-energy, femtosecond pulses with a central wavelength of 800 nm to pulses with longer wavelength, tunable between 1150 nm and 2600 nm with pulse energies of about 600 µJ to 1200 µJ. Parametric amplification is a second-order nonlinear process, based on three-wave mixing. In this process, a 'pump' photon is split into two lower-energy photons, whose energies combined are equal to the energy of the pump photon. Since the energy of a photon is proportional to its frequency, we can write this as:

$$\omega_p = \omega_s + \omega_i, \text{ where } \omega_s > \omega_i, \tag{3.1}$$

where ω_p is the frequency of the pump photon, and ω_s and ω_i are the frequencies of the 'signal' and 'idler' photon, respectively. In addition to conservation of energy, momentum has to be conserved as well, leading to the following condition for the wave-vectors of these photons:

$$\mathbf{k}_p = \mathbf{k}_s + \mathbf{k}_i, \tag{3.2}$$

where the amplitude of the wave-vector is defined as $k_{p,s,i} = \left|\mathbf{k}_{p,s,i}\right| = n_{p,s,i}\omega_{p,s,i}/c$. This condition is also known as *phase matching* and is not trivial, as most media have a frequency-dependent refractive index, i.e., $n_p \neq n_s \neq n_i$. As a result, Equation 3.2 is not satisfied easily and just having a second-order nonlinearity is not enough for parametric amplification.

To achieve phase-matching, birefringent nonlinear crystals, such as β-barium borate (BBO) or lithium triborate (LBO), are often used. Birefringent materials have different refractive indices for different polarizations of light. For example, uniaxial birefringent materials have an 'ordinary' refractive index (n_o) for light polarized perpendicular to the optical axis. Light polarized parallel to this optical axis experiences a different, 'extraordinary' refractive index (n_e).

This birefringence is exploited in optical parametric amplification by using a combination of the two orthogonal polarizations for pump, signal, and idler. One of these polarizations is in the plane formed by the propagation direction and the optical axis of the crystal, the other is perpendicular to this plane. The refractive index for a combination of the pump, signal, or idler can be controlled by adjusting the angle of the optical axis with respect to the propagation direction. By mounting the crystal on a (motorized) rotational mount, Equation 3.2 can be satisfied for multiple wavelengths and the OPA can be used to generate different signal and idler wavelengths. In Type I phase-matching, the signal and idler are polarized in the same direction, perpendicular to the pump polarization. For femtosecond OPAs, typically negative uniaxial crystals are used, where $n_e < n_o$. The pump is then polarized along the extraordinary axis [40]. In Type II phase-matching, the signal and idler are orthogonally polarized, and the pump is polarized in the same direction as either the signal or the idler. This results in four possible combinations, all (confusingly) named Type II [41]: pump and signal (idler) are polarized along the extraordinary axis, and the idler (signal) along the ordinary axis. Or the pump and signal (idler) are polarized along the ordinary and the idler (signal) along the extraordinary axis.

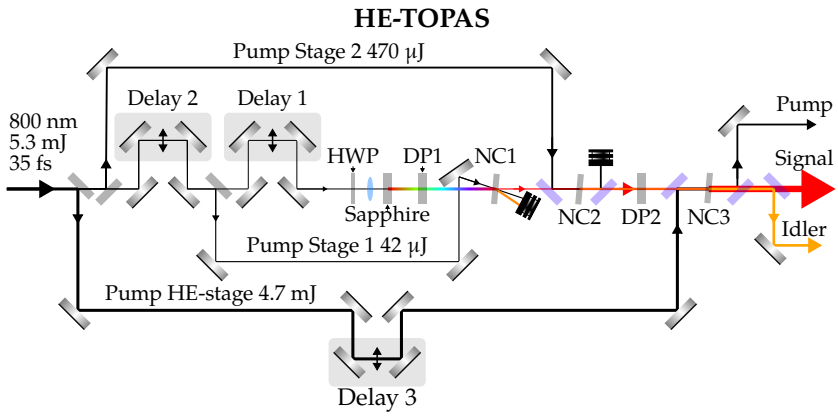

Figure 3.3: Schematic drawing of the three-stage OPA system. HWP: half-wave plate, DP: dispersive plate, NC: nonlinear crystal.

The optical parametric amplifier (OPA) used in the experiment is a HE-TOPAS from Light Conversion. It consists of three OPA stages and schematically shown in Figure 3.3. A fraction of the input of the input pulse generates a white light continuum (WLC) in sapphire, which serves as the seed for the optical parametric amplification. Before the WLC generation, a half-wave plate rotates the polarization of the light by 90°, such that it is vertical and perpendicular to the pump (and idler) polarization. This means that the HE-TOPAS uses Type II phase-matching, with pump and idler linearly polarized along the extraordinary axes of the crystals. This WLC pulse is chirped by a dispersive plate. By adjusting the arrival time of the chirped pulse with respect to the pump pulse, a different wavelength can be parametrically amplified in nonlinear crystal 1 (NC1). The amplification occurs in a noncollinear geometry, the signal pulse can therefore be separated easily from the depleted pump and idler pulses.

In NC2, the signal is further amplified by a collinearly propagating pump pulse that is removed afterwards by a dichroic mirror. A second dispersive plate separates the signal and the idler pulses in time.

In the power amplification stage, consisting of NC3, about 90 % of the input pulse energy is used to collinearly amplify either the signal or idler pulse. Finally, two dichroic mirrors separate the depleted pump and idler pulses from the signal.

The maximal signal pulse energy, at a wavelength of 1.3 μm is about 1.2 mJ, and about 650 μJ for the idler, at a wavelength of 2.08 μm. At other signal wavelengths, the conversion is less efficient.

3.4 ULTRAFAST SPECTROMETER

As discussed in Section 2.2, the detection of strain waves in materials is strongly dependent on the probe wavelength, in particular near surface plasmon polariton resonances (SPRs). In previous experiments [17, 42], the probe wavelength was adjusted by tuning the central wavelength of the output of the OPA, and only a single (central) wavelength was measured in an experiment. The experiment was then repeated for a different central wavelength. Additionally, the ultrashort pulses generated by the OPA have a bandwidth of approximately 15 nm to 20 nm, which limited the spectral resolution of these experiments. This limitation was too restrictive to accurately measure the surface plasmon polariton (SPP)-enhanced reflectance changes of the segmented grating.

As a temporary solution, a monochromator was constructed using a grating, lens, and slit, to reduce the bandwidth of the pulses after reflecting from the sample. This improved the spectral resolution significantly, which enabled us to measure the SPP-enhanced reflectance changes of the segmented grating (shown in Chapter 4). Despite the improvement in spectral resolution, the measurements were still time-consuming, since the experiment had to be repeated for each wavelength. However, multiple wavelengths can in principle be measured simultaneously by using a detector such as a linear photodiode array or a camera. By using a WLC pulse, this can be extended to a very broad wavelength range.

To implement this, an experimental setup was built consisting of three key components: the WLC generation, the spectrograph, and the detector (camera). They are described, in the order as they are mentioned, in the following section.

3.4.1 *White Light Continuum Generation*

Generating the ideal WLC pulse for use as a probe is challenging, as many parameters influence the generated spectrum and stability. Ideally, the generated WLC spectrum should be flat over the region of interest and stable over time. Section 2.4 provides some theoretical background behind the non-linear generation process.

Finding the right generation medium

The working range of the spectrometer is approximately 450 nm to 1000 nm, hence a pulse with a spectrum covering this wavelength range is required. The upper limit is determined by the sensitivity of the camera: At 1000 nm, the quantum efficiency (QE) of the Si-based complementary metal-oxide-semiconductor (CMOS) sensor is only about 10 % and drops to zero at longer wavelengths. The lower limit is set by the 400 nm light used to pump the sample. As it is an intense pulse, even scattered light can saturate the camera for those wavelengths. A long-pass filter with a cut-on wavelength of 450 nm blocks all pump light, effectively setting the lower boundary.

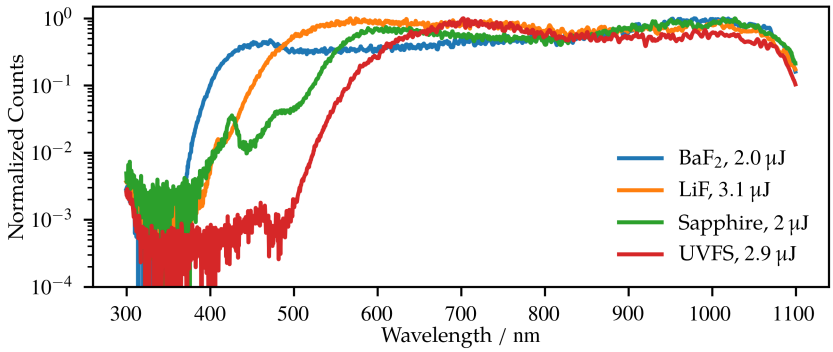

Figure 3.4: The visible/NIR part of the spectra of WLC pulses generated by a 1300 nm, 70 fs pulse in BaF_2, LiF, sapphire, and UVFS. The pulse energies are specified in the legend.

Reference [43] discusses some potential media in which we can generate a spectrum that covers this range. Among them are barium fluoride (BaF_2), lithium fluoride (LiF), sapphire (Al_2O_3), and UV grade fused silica (UVFS). For these media, the measured visible/near-infrared (NIR) parts of the spectra of the WLC pulses generated by 1300 nm pulses are shown in Figure 3.4 . The WLC spectra are relatively flat for wavelengths longer than 600 nm, but the blue parts of the spectra differ significantly. Based on these measurements, BaF_2 and sapphire were chosen as generation media. Barium fluoride generates the most blue light, down to 400 nm, even when pumping at 1300 nm. When measuring mostly longer wavelengths (between 700 nm and 1000 nm), sapphire can also be used, as it generates exceptionally stable WLC pulses.

Stability of the WLC

The spectra shown in Figure 3.4 are, unfortunately, only snapshots. Over time, the spectrum typically degrades as damage accumulates in the medium. The rate and extent of the degradation vary per material. For example, the WLC spectrum generated in LiF degrades particularly quickly, as illustrated in Figure 3.5. This figure shows the spectrum of WLC pulses generated in LiF crystal, recorded every minute for 14 minutes.

To reduce these effects, we mount the crystal on a motorized stage that moves the crystal in both x- and y-directions, at different speeds, creating Lissajous figures, as recommended by [44]. These figures maximize the coverage of the crystal by the pump pulses, such that all positions get as little exposure as possible.

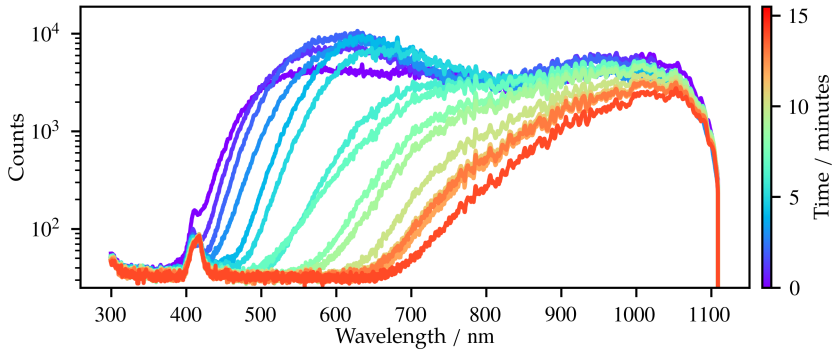

Figure 3.5: The visible/NIR part of the spectrum of the WLC generated by a 2 µJ, 1300 nm pulse in a 3 mm thick LiF crystal measured over 14 minutes with 1 minute intervals. Note that the LiF crystal is *not* moved during this measurement.

3.4.2 *Spectrometer*

A spectrometer consists of two main components: the spectrograph and the detector. The spectrograph separates the wavelengths using a *dispersive* element, such as a prism or grating and focuses them onto a detector using a lens system. Typically, the detector consists of several smaller detectors in a line, such as a linear photodiode array or a 2D camera sensor.

Detector

The setup and its intended uses requires that the detector has the following properties. First, and foremost, the detector needs to be able to record spectra at 1 kHz, the same rate as the probe pulses. Second, the pixel ADC must be at least 12 bit to be able to measure changes as small as 10^{-3}, the typical strain-wave-induced reflectance change. Third, the detector must have the ability to record two spectra simultaneously. This allows for referencing, reducing measurement noise.

Given these requirements, the Andor Zyla 4.2 PLUS from Oxford Instruments was considered the most suitable choice. The Zyla 4.2 is a scientific CMOS camera with 2048 × 2048 pixels with 16 bit resolution. The well depth of each pixel is 3.5×10^4

electrons. The quantum efficiency (QE) as function of wavelength is shown in Figure 3.6 and peaks at 560 nm with a QE of 82.2 %. The QE is larger than 60 % for wavelengths between 450 nm to 760 nm, making it ideal to use for visible light.

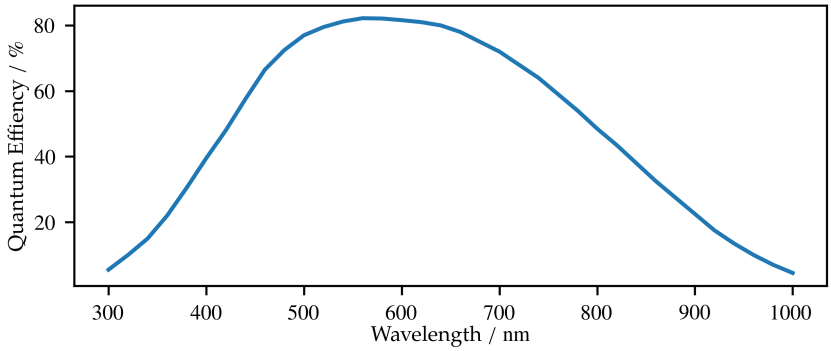

Figure 3.6: Quantum efficiency of Andor Zyla 4.2 PLUS, adapted from [45].

The camera has features specifically convenient for use as a spectrometer. For example, it has a multitrack mode, where multiple areas can be read out simultaneously. These tracks can be separated by several rows of pixels and the vertical pixels within each area can be summed on camera.

Spectrograph

In our setup, the spectrograph consists of a blazed reflection grating and two cylindrical lenses. The grating disperses the wavelengths, which are focused onto the camera sensor by the two lenses. The reflection grating (GR25-0305) has 300 lines per mm, a blaze wavelength of 500 nm and a blaze angle of 4°18′. The first cylindrical lens ($f = 150\,\mathrm{mm}$) focuses every wavelength onto a column of pixels in the plane of the sensor. This lens partly determines the spectral resolution of the camera. The second lens ($f = 75\,\mathrm{mm}$) is rotated by 90° with respect to the first, and focusses the spectrum onto a number of rows on the camera. By using a second lens for this, it is possible to change the focus such that the spectrum covers more pixels in the vertical direction, without sacrificing spectral resolution, since the focussing of different wavelengths onto different pixel columns is determined by the first lens. At the sensor, the change in wavelength, λ, as a function of position on the sensor, x, can be approximated by [46]:

$$\frac{\mathrm{d}\lambda}{\mathrm{d}x} = \frac{d}{nf} = \frac{1}{300 \times 10^{-3} \cdot 150 \times 10^{-3}} = 2.2 \times 10^{-5}, \tag{3.3}$$

where d is the period of the grating, which is the inverse of the number of lines per mm. Furthermore, n is the diffraction order, which is 1, and f the focal distance of the lens. This means that for a 13.3 mm wide sensor, we could measure over a range of about $2.2 \times 10^{-5} \cdot 13.3 \times 10^{-3}\,\mathrm{m} = 295.5\,\mathrm{nm}$.

Two spectra, the sample reflection ('signal') and a reference, are measured simultaneously. They are focused onto vertically separated areas on the camera, as shown schematically in Figure 3.7A. The camera reads out both areas at the same

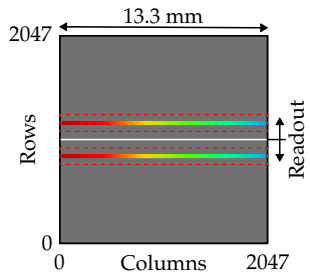

Figure 3.7: Illustration of the camera sensor showing two active areas (red dashed areas), a spectrum is projected onto each area. The bottom and top halves of the sensor are read out simultaneously, starting at the centre row.

time, with the rows within each area being summed. For each summed pixel value, the total count is transmitted as a 32 bit integer to the computer. As a result, for each probe pulse, the camera sends two spectra, each consisting of 2048 counts. In the following, we will refer to the 2048 columns of pixels as just 'pixels', for brevity.

3.4.3 *Calibration and Data Processing*

Calibration

The spectrometer is calibrated using a didymium glass reference material (RM-DG, Starna). The manufacturer has provided a list with the wavelengths of the absorption peaks of the material. The spectra on the camera are calibrated by measuring the absorbance of the reference material. The absorbance, in optical density (OD), is defined as follows:

$$A[i] = \log_{10}\left(\frac{I_0[i]}{I_{\mathrm{RM}}[i]}\right), \tag{3.4}$$

where i denotes the pixel number, I_0 is the sample reflection spectrum and I_{RM} is the transmission of the sample reflection spectrum through the reference material. Both spectra are typically averaged over 10 000 probe pulses and the average dark count of each pixel of the camera is subtracted.

Figure 3.8 shows the measured absorbance as a function of pixel number of the didymium reference material for wavelengths between 465 nm and 755 nm, measured in one of the experiments of Chapter 5. The pixel numbers from the maxima of the absorption peaks (shown with red circles) and the corresponding wavelengths are shown in Table 3.1. The wavelengths are taken from the Certificate of Calibration accompanying the reference material.

A linear fit through the points is ultimately used to map the pixel number to the corresponding wavelength. The wavelengths are shown on the top horizontal axis in Figure 3.8.

Data Processing

Let us consider a typical measurement performed using the spectrometer. We measure the change in reflectance using 2048 pixels of the camera, for delays

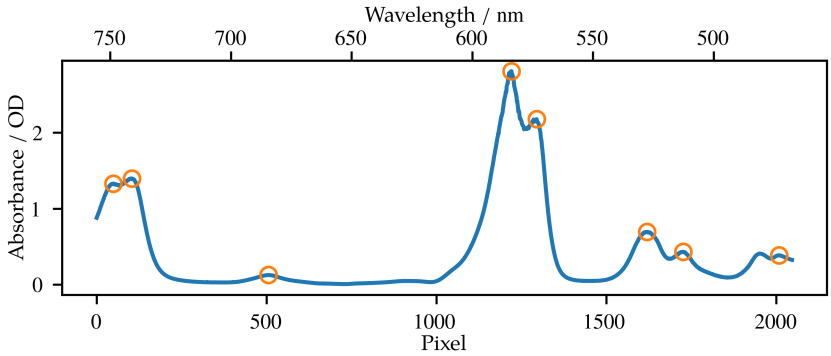

Figure 3.8: Absorbance of the didymium glass reference material, measured using the spectrometer. The open circles indicate the maxima of the absorption peaks. The calibrated wavelengths are shown on the top horizontal axis.

Table 3.1: Pixel numbers vs wavelength of absorption peaks. The two absorption peaks with the longest wavelength are not captured by the spectrometer, as well as the peak with the shortest wavelength.

Pixel number	-	-	49	104	506	1221	1295	1620	1727	2009	-
Wavelength / nm	879	807	749	741	685	585	573	529	513	472	431

ranging from −20 ps to 1000 ps, with a step size of 2 ps. The delays are scanned twice–first in ascending order, then in descending order. For each delay step, the sample reflection spectrum and reference spectrum from 2000 probe pulses are recorded. As mentioned earlier, each pixel returns a 32 bit (=4 Byte) number to the computer. For this single measurement, the spectrometer collects the following amount of data:

$$\begin{aligned} 2\ \text{spectra} \times 2048\ \text{pixels} \times 2000\ \text{pulses} \times 510\ \text{delay steps} \times 2\ \text{scans} \times 4\,\text{B} \quad (3.5)\\ = 33\,423\,360\,000\,\text{B} \approx 33.4\,\text{GB}. \end{aligned}$$

The data is saved as an unstructured binary file, with pixel counts saved in the order they are measured. Consequently, recovering the reflectance change per pixel at each delay step requires some preliminary knowledge. Fortunately, the measurement software (developed by AMOLF Software Engineering) generates a second file containing metadata, such as the number of pulses that are measured at every delay step and the corresponding delay steps (in order). A third file may be produced, containing data measured from other equipment, such as photodiodes. This binary file is ordered in the same way as the file containing the spectrometer data, but the other equipment typically returns only a single value per probe pulse, hence this file is easier to process.

In the data processing, we take into account the following factors. They are explained below:

1. Dark count subtraction

2. Referencing

3. Outlier exclusion

In a CMOS sensor, every pixel generates a small electric current, even when not exposed to any light. This is known as dark current and results in a dark count, as the current is converted into a number by the ADC. The dark count depends on the exposure time. Before the actual measurement, we measure the average dark current for each pixel and subtract this value from the pixel count recorded later.

Next, we take into account the reference spectrum of every probe pulse. We record the spectrum of the probe pulse that is split off before reflecting from the sample, allowing us to correct for pulse-to-pulse fluctuations in the probe spectrum. We divide the pixel counts from the sample reflection (the 'Signal' track) by the pixel counts from the 'Reference' track. It is crucial that the Reference pixel corresponds to the same wavelength as the Signal pixel, otherwise the referencing will introduce extra noise.

Before starting a measurement, we ensure that both spectra are optimally aligned. This is done using a didymium glass reference material (RM-DG, Starna) that provides well-defined absorption lines in the visible spectrum and serves as a tool for alignment. We focus particularly on ensuring that the two spectra have the same spatial dispersion on the camera sensor. Any shift between the two tracks can be corrected post-measurement, by linearly shifting the tracks with respect to each other. We use the shift with the lowest mean squared error (MSE) between the absorbance of the reference material measured by the two tracks.

Occasionally, WLC pulses contain significantly more or less light than the average pulse. We exclude these 'catastrophic' events [44] as follows: Before calculating the change in reflectance, we first calculate the average and the standard deviation of the sum of the pixel count of the Reference track, using all probe pulses in the measurement. If the sum of the pixel count of the Reference track of a single pulse deviates more than 5 standard deviations of the average, we exclude both that pulse and the corresponding blocked or pumped pulse.

4

SURFACE-PLASMON-ENHANCED STRAIN-WAVE-INDUCED OPTICAL DIFFRACTION CHANGES FROM A SEGMENTED GRATING

ABSTRACT

We report on surface plasmon polariton-enhanced, strain-wave-induced reflection and diffraction changes on a gold-covered, segmented grating. The segmented grating has a 6020 nm period, and its lines are segmented into 7 periods of a 430 nm period grating, which allows the excitation of surface plasmon polaritons. This grating has three surface plasmon polariton resonances at different optical wavelengths, for the same incident angle. Pump-pulse-induced strain waves are probed by measuring reflection and diffraction of a tunable probe pulse in a wavelength range that includes all three surface plasmon polariton resonances. surface acoustic waves and longitudinal waves are identified. When probing close to surface plasmon polariton resonances, the reflection changes from surface acoustic waves and longitudinal waves are strongly enhanced by factors of 23 and 36, respectively, compared with reflection changes observed when probing at off-resonance wavelengths. The relative surface acoustic wave- and longitudinal wave-induced diffraction changes are larger by additional factors of up to 3.3 and 2.6, respectively, compared to the reflection changes.

Parts of this chapter have been published in Photoacoustics 31 (2023) 100497 [47]

4.1 INTRODUCTION

WAFER ALIGNMENT is a crucial step in the semiconductor device manufacturing process. An important method to align wafers is to measure the phase difference between, for example, the minus and plus first-order diffracted beams of a so-called alignment grating, which is a phase grating etched into the silicon wafer. By measuring changes in this phase difference when the wafer with the grating is displaced along the grating vector, the position of the grating can be determined with (sub-)nanometre accuracy [4].

However, in semiconductor device manufacturing, many layers are deposited onto the wafer, also covering these alignment gratings. Unfortunately, some of these layers can be (partially) opaque to light. In that case, determining the position of the alignment grating can become very challenging. Previously, we have shown that such gratings, buried underneath opaque layers, can be detected using laser-induced strain waves [15, 16]. In these experiments, a pump pulse excites a strain wave near the surface, which travels downward through the stack of layers. The strain wave reflects off the buried grating and, due to the spatially periodic topography of the grating, becomes a strain wave 'copy' of the grating. The returning grating-like strain wave deforms the surface and/or changes the refractive index, forming a grating from which a delayed probe pulse can diffract. Although this is a promising technique to detect alignment gratings buried underneath opaque layers, the diffracted signal strength is currently too low for practical applications.

To increase signal strength, we recently showed that the optical detection of strain waves on metallic gratings can be enhanced by probing near a surface plasmon polariton resonance (SPR) [17]. Surface plasmon polaritons (SPPs) are electromagnetic waves, travelling along, and bound to, a metal/dielectric interface, coupled to plasma oscillations of the free electrons near the surface of the metal. To excite SPPs, both energy and wave vector conservation is required. For a given incident wavelength this is only achieved for a certain grating period and incident angle. The amplitude and central wavelength of the SPR are changed by the material density changes and by deformations of the grating shape, induced by strain waves. This leads to relatively large variations in the amount of absorbed and reflected light, thus enhancing the optical signal strength.

In this chapter, we extend this work to so-called segmented gratings. These gratings, often used in the semiconductor manufacturing industry, are segmented in the sense that the grating lines (ridges) are subdivided into multiple shorter period lines and spaces (valleys). This is typically done to increase the diffraction efficiency of specific orders [48, 49].

Here, the segmented grating consists of an Au-covered, 6020 nm period alignment grating, where each grating line is segmented into seven lines forming a 430 nm period grating that can sustain SPPs. This is mathematically equivalent to amplitude modulation of a high-spatial-frequency grating by a low-spatial-frequency grating, which leads to sidebands in the spatial frequency domain. As a result, white light spectroscopy shows that the segmented grating has not one, but *three* plasmonic resonances for a fixed angle of incidence. A tunable probe pulse is used to probe the segmented grating in the wavelength range from 600 nm to 705 nm, which includes the three plasmonic resonances at 611 nm, 650 nm, and 695 nm. In the experiment, we not only measure the reflection of the probe pulse from the sample as function

of the delay between pump and probe pulse, but also the plus and minus first-order of the probe light diffracted off the long-period alignment grating as a function of pump-probe delay.

Similarly to what was found in earlier experiments on *non*-segmented (plasmonic) gratings [17], we observe several types of strain waves, such as longitudinal waves (LWs) and surface acoustic waves (SAWs). We observe strong enhancements, both in the strain-wave-induced reflection changes and in the strain-wave-induced diffraction changes when tuning the probe wavelength around all three plasmonic resonances. In reflection, the enhancement is a factor of 23 to 36, depending on the type of strain wave, when probing with wavelengths close to the SPR wavelength compared with probing with off-resonance wavelengths. Diffraction measurements show a maximum relative change that is a factor of 3.3 larger for SAWs, compared to the reflection measurements. Surprisingly, we find that the measured SAW period increases with increasing probe wavelength. Furthermore, we observe that the sign of the SAW-induced diffraction, changes around certain probe wavelengths. Finally, we observe that the photo-acoustic signal associated with the longitudinal waves change sign when probing near the SPRs. This is caused by strain-wave-induced changes in the position of the SPR. Our results prove that SPPs can be used to enhance photo-acoustic signals on non-continuous, segmented gratings.

The structure of this chapter is as follows. In Section 4.2, the experimental setup and the segmented grating sample are briefly described. The results of white light spectroscopy of the segmented grating are presented in Section 4.3. In Section 4.4, an analysis of the white light spectroscopy results using a simple model for SPPs is presented. The results of the photo-acoustic experiments are presented and discussed in Section 4.5 and Section 4.6, respectively. In Section 4.A, more details on the experimental setup can be found. In Section 4.B, we discuss, in more detail, the existence of the three SPR on the segmented grating. Finally, in Section 4.C, we show a transient grating measurement on a flat part of the sample, where only LW can be excited. The frequency of the measured strain waves matches the frequency we assigned to the LW in the measurements on the grating.

4.2 EXPERIMENTAL SETUP

A schematic view of the experimental setup is shown in Figure 4.1(a). The sample is illuminated by a 400 nm, 50 fs pump pulse at an incident angle of about 5° with respect to the surface normal, which does *not* excite SPPs. A time-delayed probe pulse, with a central wavelength tunable between 600 and 705 nm, is incident at an angle of 27° with respect to the surface normal and excites SPPs at wavelengths of approximately 611, 650, and 695 nm. After illuminating the sample, an aperture selects one diffraction order and the light is spectrally filtered to reduce the bandwidth to about 2 nm full-width at half maximum (FWHM). For more details, we refer to Section 4.A.

The segmented grating was made by NanoPHAB BV (Eindhoven, the Netherlands) using e-beam lithography, and is etched into a layer of 200 nm SiO_2 on a Si substrate. Using thermal evaporation, a layer of Au with a thickness of 172 nm$\pm$3 nm is deposited onto the grating. This thickness was determined via a photo-acoustic measurement (see Section 4.C for more details). The amplitude of the grating is

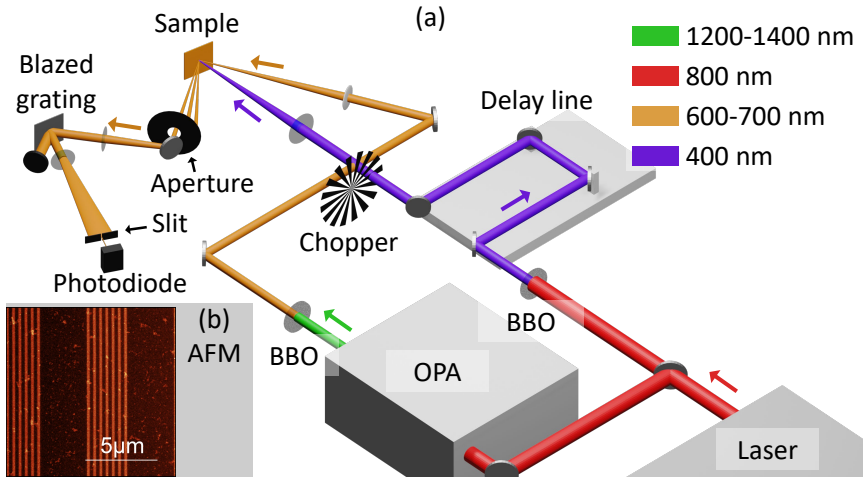

Figure 4.1: (a) A schematic view of the experimental setup with the used wavelengths, indicated by the differently coloured beams, OPA: optical parametric amplifier, BBO: β-barium borate crystal. (b) atomic-force microscopy (AFM) micrograph of the Au-covered segmented grating used in the experiments.

about 31 nm and the duty cycle of the 430 nm grating is 44 %. An atomic-force microscopy (AFM) image of the Au-covered grating is shown in Figure 4.1(b).

4.3 WHITE LIGHT SPECTROSCOPY

White light spectroscopy of the segmented grating is performed, where the spectra of the zeroth- (reflection), first-, and second-order diffracted beams were recorded, for both *s*- and *p*-polarized light. Both the plus and minus orders of the non-zero diffraction orders are recorded. In addition, these spectra were simulated using rigorous coupled wave analysis (RCWA) numerical calculations [50]. The RCWA numerical calculations were performed with at least five hundred harmonics, to ensure convergence. Figure 4.2 shows the measured and calculated spectra for these orders. The reflected spectrum is shown as the ratio of the *s*- and *p*-polarized reflected spectra, while the diffraction spectra shown are only for *p*-polarized light and are normalized to the maximum of each individual spectrum. The results of the white light spectroscopy for the plus and minus second-order diffraction are shown for completeness only. The measured strain-wave-induced changes in the second-order probe diffraction were also recorded but are not discussed in this paper.

4.3.1 *Reflection*

Figure 4.2(a) shows the ratio of the measured (solid line) *s*- and *p*-polarized reflection spectra. The dashed line shows the ratio of the *s*- and *p*-polarized reflection spectra as calculated by the RCWA code. We note that the SPPs are only excited with *p*-polarized light. By plotting the ratio of reflection spectra for *s*- and *p*-polarized

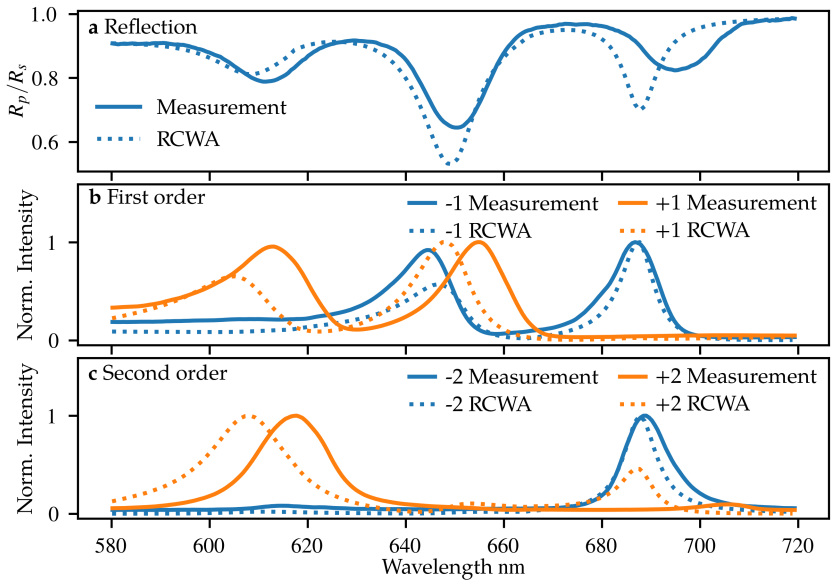

Figure 4.2: Measured and calculated spectra of the specular reflection, plus and minus, first- and second-order diffraction. (a) Measured (solid) and calculated (dashed) ratio of the reflection spectra of *s*- and *p*-polarized incident light. (b and c) Measured (solid) and calculated (dashed) individually normalized spectra of plus (red) and minus (blue), first-(b), and second-order (c) diffraction, for *p*-polarized incident light.

light, features common to both polarizations are suppressed, while SPPs are highlighted.

In Figure 4.2(a), three dips, at 611, 650, and 695 nm, are visible in the measured spectra. Each one corresponds to an SPR, which is explained in more detail in Section 4.B. We note again that, in contrast to these results, a *non*-segmented grating typically only shows *one* SPR, in lowest order [51, 52]. In the calculated spectrum, three dips are also present, but at the slightly different wavelengths of 608, 650, and 688 nm. Furthermore, the shapes and depths of the dips are somewhat different. The calculated dip at 608 nm, for example, is less deep than the measured resonance at 611 nm. At 650 nm, the calculated dip is much deeper than measured, and the dip at 688 nm is both narrower and deeper than the measured one. The difference between the calculation and the measurement may be due to deviations in the shape of the fabricated grating from the perfect rectangular shape used in the calculations.

4.3.2 *First-order diffraction*

The plus (red) and minus (blue) first-order diffraction spectra for *p*-polarized incident light are shown in Figure 4.2(b). The solid lines are the measured spectra and the dashed lines are calculated with the RCWA code. The measured, plus first-order diffraction spectrum has peaks at 613 and 654 nm, while the calculated spectrum

has peaks at 605 and 648 nm. The measured, minus first-order spectrum peaks at 645 nm and 687 nm, the calculated spectrum has peaks at 647 and 688 nm. Again, differences between calculated and measured spectra are attributed to deviations from a perfect rectangular shape of the grating used in the experiment.

4.3.3 *Second-order diffraction*

Figure 4.2(c) shows the plus (red) and minus (blue) second-order diffraction spectra for *p*-polarized incident light. The solid lines represent the measured spectra and the dashed lines the calculated spectra. In contrast to the first-order diffraction spectra, only one peak is visible in the second-order spectra. This peak is at 617 nm for the measured, and at 608 nm for the calculated plus second-order diffraction spectrum. The RCWA calculation shows a second peak in the plus second-order at 687 nm, which is not present in the measured spectrum. The minus first-order has its peak at 689 nm for the measured spectrum and at 688 nm for the calculated spectrum. As before, the difference between calculated and the measured spectra are attributed to deviations in the shape of the fabricated grating from a perfect rectangle. It is known that such deviations have a stronger influence on higher diffraction orders [53, 54].

4.4 SURFACE PLASMON POLARITONS

Surface plasmon polaritons (SPPs) of a specific (optical) frequency can be excited by light incident with a certain angle on a metallic grating, depending on the dielectric function of the metal and, more importantly, the grating period. The segmented grating is essentially a modulation of a short-period 'plasmonic' grating by a longer-period 'alignment' grating. As a result, 'sideband' gratings exist at the difference and the sum of the plasmonic and alignment (angular) spatial frequencies, which are k_{p1} and k_A respectively. Visible light can excite SPPs on the original plasmonic grating and the difference (with angular spatial frequency k_{p2}) and sum (with k_{p3}) gratings at the same incident angle of 27° with respect to the surface normal, but for different wavelengths. Table 4.1 shows the angular spatial frequency, associated grating period, the SPR wavelength calculated via Equation 4.5, and the measured SPR wavelength, for each of these three gratings. For a more elaborate description of SPPs on the segmented grating, we would like to refer to Section 4.B.

Table 4.1: Measured and calculated SPR wavelengths of the 'original' plasmonic grating (with angular spatial frequency k_{p1}) and the two 'sideband' gratings (k_{p2} and k_{p3}). The resonance wavelengths were measured at an incident angle of about 27° and were calculated using Equation 4.5 for an incident angle of 27.7°.

Grating angular spatial frequency	Period (nm)	SPP resonance wavelength (nm)	
		Calculation	Measurement
$k_{p1} = 14k_A$	430	650	650 ± 1
$k_{p2} = 13k_A$	463	695	695 ± 1
$k_{p3} = 15k_A$	401	612	611 ± 1

4.4.1 *SPP coupling to propagating light*

Surface plasmon polaritons, when propagating along a surface, can couple to free-space light modes when a grating is present at the surface. In this subsection, we investigate in which directions light can couple out when SPPs are propagating along the surface of the segmented grating. This analysis is similar to that shown in [55].

Consider a situation where an SPP is propagating along an Au/Air interface with a grating present, as shown in Figure 4.3. In this situation, the SPP travels to the left, similar to Figure 4.17, and couples out to light propagating in free space in the x- and positive z-direction, at an angle θ_{out} with the z-axis, when the following condition is met:

$$k_{\text{SPP}} = k_0 \sin\theta_{\text{out}} - k_g. \tag{4.1}$$

This equation is very similar to Equation 4.5, except that here, we describe the situation where light is coupled *out*.

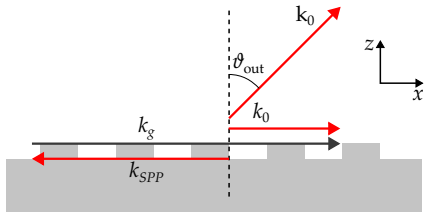

Figure 4.3: Sketch of the coupling of SPPs to free space light modes, which propagate in a direction with an angle θ_{out} with the z-axis and with wave vector k_0 using a sub-wavelength grating with angular spatial frequency k_g.

As an example, let us consider SPPs excited on the grating with angular spatial frequency $k_g = k_{p1}$, incident at an angle θ_{in}, and propagating along the segmented grating in the negative x-direction. In principle, three gratings with angular spatial frequency k_{p1}, k_{p2}, or k_{p3} can be used to couple to a freely propagating mode. Using Equation 4.1, the direction of the propagating light can be calculated. If we choose $k_g = k_{p1}$, and by substituting k_{SPP} in Equation 4.1 with the expression in Equation 4.5, the angle θ_{out} can be calculated with,

$$k_1 \sin\theta_0 - k_{p1} = k_1 \sin\theta_{\text{out}} - k_{p1}. \tag{4.2}$$

It follows that $\theta_{\text{out}} = \theta_{\text{in}}$. The light propagates in the direction of the specular reflection.

If light couples out using a different grating, for example, on the grating with $k_g = k_{p2} = 13k_A$, this results in:

$$k_1 (\sin\theta_0 - \sin\theta_{\text{out}}) = k_{p1} - k_{p2} = 14k_A - 13k_A = k_A. \tag{4.3}$$

This equation can be recognized as the equation for diffraction from a phase grating with angular spatial frequency k_A. Thus, light coupled in on grating k_{p1}, is coupled out through the grating with angular spatial frequency k_{p2}. It will propagate in the same direction as the plus first-order diffraction *from the long period grating*. Similarly, light coupled out on the grating with $k_g = k_{p3}$ will have the same k_x as

the minus first-order diffraction from the long period grating. SPPs excited on the sideband gratings with k_{p2} and k_{p3} will also couple out through the three gratings, in directions which coincide with the diffraction orders from the long-period alignment grating. Table 4.2 summarises which SPPs at the three resonance wavelengths are allowed to 're-scatter' in the direction of the lower order diffracted beams, from the 6020 nm period alignment grating. Every SPR can, in principle, couple to propagating modes using the three gratings which make up the segmented grating in lowest order.

Table 4.2: SPP coupling to propagating free-space propagating modes, calculated using the grating angular spatial frequencies shown in Table 4.1 and calculated using Equation 4.1. The propagating modes are in the same direction as the diffraction orders, diffracted off the 6020 nm period grating. The table shows the diffraction order and the (vacuum) wavelengths of the SPPs which are allowed to re-scatter in the direction of that order.

Diffraction order from 6020 nm period grating	SPP resonance wavelengths (nm)		
−2			695
−1		650	695
0	612	650	695
+1	612	650	
+2	612		

The re-scattered light can also interfere with light directly diffracted from the long period grating. The EM-field experiences a phase shift when it couples to SPPs and also when SPPs couple to propagating waves [56, 57]. The exact phase shift is, unfortunately, not a-priori known. The interference is (implicitly) taken into account by the RCWA calculations, as it numerically solves the Maxwell Equations. Separating the contributions from the diffracted and the re-scattered light is, however, not possible.

Looking at the results from the white light spectroscopy in Figure 4.2, our simple analytical model, which takes only terms of the product of the Fourier series in lowest order into account, correctly predicts the number of peaks in each spectrum. The central wavelengths of the calculated peaks are within 8 nm of the measured peaks. More importantly, this analysis helps to understand how changes in the SPRs, induced by strain waves, can affect the diffraction from the long period grating.

4.5 RESULTS

4.5.1 *Reflection measurements*

Figure 4.4 shows the measured time-dependent pump-induced reflection changes, $\Delta R/R_0$, where R_0 is the unperturbed reflection, for selected wavelengths between 600 nm and 700 nm. For all wavelengths, a sharp peak or dip is seen for a time delay around 0 ps. For longer delays, an oscillatory signal is observed, consisting of short (< 150 ps) and long (~ 400 ps) period oscillations. The oscillation amplitude

strongly depends on the probe wavelength. Furthermore, the short period oscillations change sign when probing with a wavelength at or just above the resonance wavelength, compared to a probe wavelength just below the resonance wavelength. This behaviour can most clearly be seen when comparing the trace measured using a probe wavelength of 650 nm (the SPR wavelength) with the one measured at 645 nm. Red arrows in Figure 4.4 indicate where this change of sign is most clearly seen. In addition to the oscillations, there is also an 'offset' present in the measurements for delays > 0 ps. This offset appears to decay to ~ 0 % reflection change on a timescale of several nanoseconds.

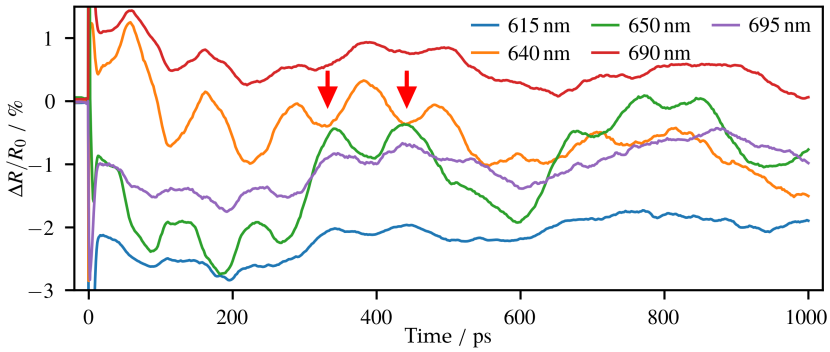

Figure 4.4: Measured probe-pulse reflection changes as function of time delay between the pump and probe pulse after excitation by the 400 nm central wavelength pump pulse, for selected probe wavelengths. Indicated with red arrows is the change in sign when measuring with a wavelength just below an SPR, at 645 nm (orange curve), compared to measuring at the SPR, at 650 nm (green curve). Note that sign changes can be seen for other time delays as well.

The sharp peak or dip observed around 0 ps delay time is caused by the effect that the fast heating and cooling of the electron gas has on the SPR, similar to what was observed in [58, 59]. The electron gas cools by heating the lattice. This leads to a rapid expansion of the lattice, which generates several types of strain waves [60]. The strain waves manifest themselves as a time-varying oscillatory change in the optical reflection [61, 62]. The slowly varying offset is likely caused by the effect that the heated (and slowly cooling) material has on the SPR via the thermo-optic effect [17]. We cannot completely exclude the possibility that the slowly varying offset could *partially* be caused by the effect of a surface acoustic wave at an acoustic frequency well below 1 GHz, associated with the periodicity of the alignment grating of 6020 nm. Only part of this surface-acoustic-wave period can be measured as the maximum time delay in our setup is limited to about 1 ns. The possible contribution from this surface acoustic wave cannot be separated from the thermally-induced change in the SPR.

The oscillatory signal shows several periodicities and we are able to identify two of them [17]: LWs at about 2.6 GHz, and LW, at 9.5 GHz. SAWs are strain waves travelling along the surface, in the direction perpendicular to the grating lines. For our Au layer thickness, the LWs manifest themselves as an expansion and contraction of the whole Au layer and have a frequency determined by the speed of sound in Au and the layer thickness. In Section 4.6, we explain the physical nature

of these different waves in more detail and how the LWs affect the probe reflection and diffraction.

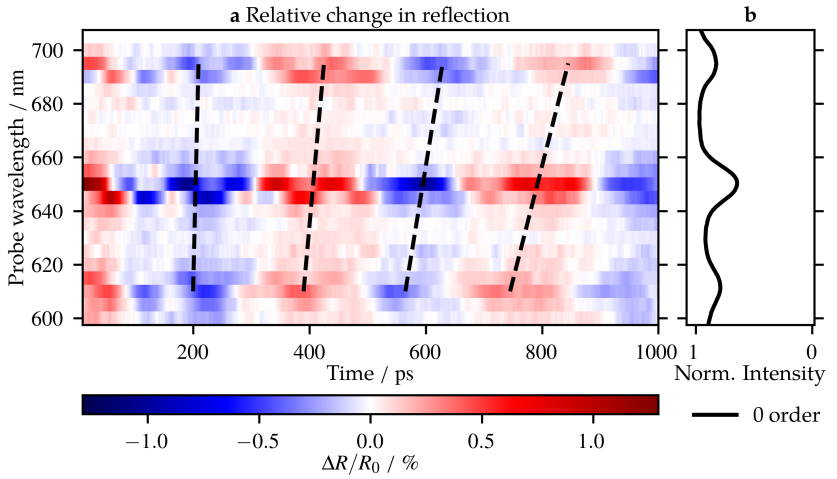

Figure 4.5: (a) Plot of the measured probe pulse reflection changes as function of time delay between the pump and probe pulse, where the slowly decaying background has been removed, for probe wavelengths between 600 nm and 700 nm. Indicated with black dashed lines is the increase in SAW period for increasing probe wavelength. (b) Ratio of measured *s*- and *p*-polarized reflection spectra.

To facilitate a comparison between the different traces, we have first removed the slowly-decaying background from each curve. This is done by subtracting a fitted decaying exponential function from these curves for times ≥ 10 ps. The results are shown as a 2D plot in Figure 4.5(a) where we plot the relative change in reflection $\Delta R/R_0$, indicated by the different colours, as a function of time (horizontal axis) after optical excitation, and as a function of probe wavelength (vertical axis). Blue indicates a decrease and red an increase of reflection with respect to the (removed) background. For ease of comparison, the ratio of the measured *s*- and *p*-polarized reflection spectra is shown on the right, in Figure 4.5(b). The figure clearly shows that the reflection changes are strongest at probe wavelengths of 610 nm, 650 nm, and 695 nm, which correspond to the SPRs. Surprisingly, Figure 4.5(a) clearly shows that the period of the SAW increases with increasing probe wavelength, as indicated by the black dashed lines.

Several oscillatory signals, with different amplitudes, frequencies, and phases, are present in the data. To extract spectra from the strain-wave signals from the time-domain data, we calculate the FFT of the curves, with the slowly-varying background removed, zero-padded from about 1 to about 32 ns. In Figure 4.6(a), we plot the amplitudes of the spectra, where the x-axis represents the strain-wave frequency, the y-axis the probe wavelength, and where the colour represents the amplitude of each frequency component (on a logarithmic scale). In Figure 4.6(b), the ratio of the *s*- and *p*-polarized reflection spectra is plotted again for comparison. For most probe wavelengths, there is a peak around a strain-wave frequency of 2.6 GHz, which is attributed to SAWs. The SAW frequency slightly decreases for

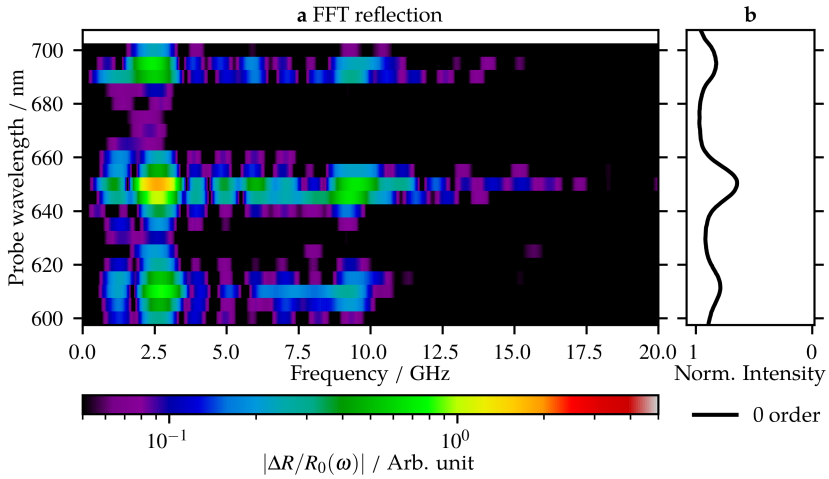

Figure 4.6: (a) Plot of the fast Fourier transform (FFT) spectra of the measured probe pulse reflection changes, for probe wavelengths between 600 nm and 700 nm. (b) Ratio of measured *s*- and *p*-polarized reflection spectra.

increasing probe wavelength, which can be seen more clearly in the time-domain data in Figure 4.5 as an increasing oscillation period with increasing probe wavelength. For probe wavelengths close to the SPRs, an additional peak is observed around 9.5 GHz, corresponding to the LWs. By comparing the FFT amplitudes of the SAW and LW of the measurement with the smallest reflection changes, at the probe wavelength of 675 nm, to those of the measurement with the largest changes, at 650 nm, we find that the SAW amplitudes are increased by a factor of about 23 and the LW amplitudes by a factor of about 36.

In previous experiments on non-segmented gratings [17], a third type of strain wave was identified, in addition to the SAW and LW. This was the (Quasi-)Normal Mode (NM), a vibration of the grating lines, with a frequency between that of the SAWs and LWs. The NM was identified by its frequency [63], and we expect a NM frequency of about 8 GHz for the small-period grating line size of this segmented grating. This is a higher frequency than observed in previous experiments, as the (short-period) grating line dimensions are smaller than in the earlier experiments [17]. While the amplitudes of the spectra for strain-wave frequencies between the SAWs and LWs are not zero, at least for probe wavelengths close to the SPRs, there is no clear peak around 8 GHz. Thus, these oscillatory signals cannot be attributed to NMs, and their origin is currently not known.

4.5.2 *Minus first-order diffraction measurements*

In our measurements, we observe first-, and second-order probe diffraction off the long-period alignment grating. The pump-induced relative changes in the minus first-order diffraction efficiency of the probe, $\Delta\eta/\eta_0$, where η_0 is the unperturbed diffraction efficiency, as a function of pump-probe delay time, are shown in Figure 4.7, for selected probe wavelengths. Similar to the time-dependent reflection

measurements, a sharp peak or dip is seen for all probe wavelengths around 0 ps time delay, and oscillatory signals with short and long periods are observed for longer delay times. A slowly-decaying thermal background is also present. In comparison to the reflection measurements, the strain-wave-induced changes in diffraction, as well as the diffracted signal from the initial thermal background are larger. In the reflection measurements, the maximum peak-to-peak change is about 2 %, while in the minus first-order diffraction the maximum peak-to-peak change is about 5 %. For probe wavelengths close to the SPR wavelengths, a change in sign is again observed for the LW oscillations, similar to what is seen in the reflection measurements.

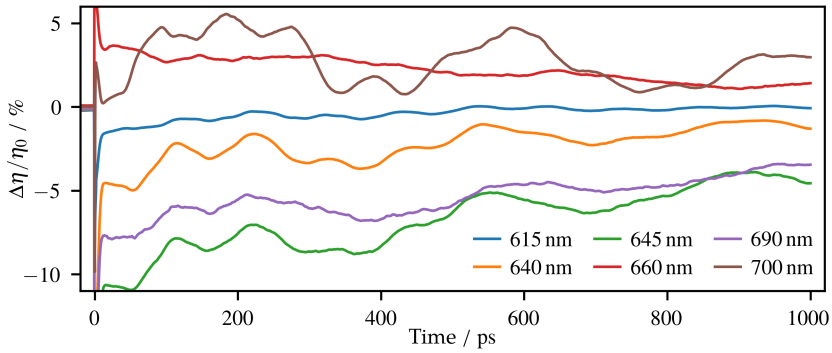

Figure 4.7: Measured changes in minus first-order probe *diffraction* as function of time delay between the pump and probe pulse after excitation by the 400 nm pump pulse, for selected probe wavelengths.

Figure 4.8(a) shows the changes in diffraction as a function of pump-probe delay time for all probe wavelengths, where the decaying thermal background was removed in a similar manner as in the reflection measurements. Figure 4.8(b) shows two measured spectra: the ratio of the *s*- and *p*-polarized reflection spectra and the minus first-order diffraction spectrum, all measured for an incident angle of 27° with respect to the surface normal. As in the reflection measurements, the long period SAW is clearly visible and has the largest amplitude. Interestingly, in contrast to the reflection measurements, strong signals are only seen around the two longer SPRs wavelength, at 650 and 695 nm. At the shortest SPR wavelength of 610 nm, there is neither a peak in the diffraction spectrum (Figure 4.8(a)), nor are there enhanced photo-acoustic signals. Furthermore, the peak wavelengths are slightly redshifted with respect to the peaks in the minus first-order diffraction spectrum, which are at 645 and 687 nm, as can be seen in Figure 4.8(b). Figure 4.8(a) also shows that the SAW period increases, similar as in the reflection measurements, when the probe wavelength increases from 650 to 705 nm. Interestingly, here the SAW also changes sign in between 660 and 675 nm, which was not observed in either the reflection measurement or in previous experiments on non-segmented gratings [17]. For probe wavelengths shorter than 645 nm, the shape of the traces remains similar, but the amplitude decreases with shorter probe wavelengths.

Figure 4.9(a) shows the amplitude of the FFT of the strain-wave signals, as a function of strain-wave frequency and probe wavelength. Figure 4.9(b) shows the

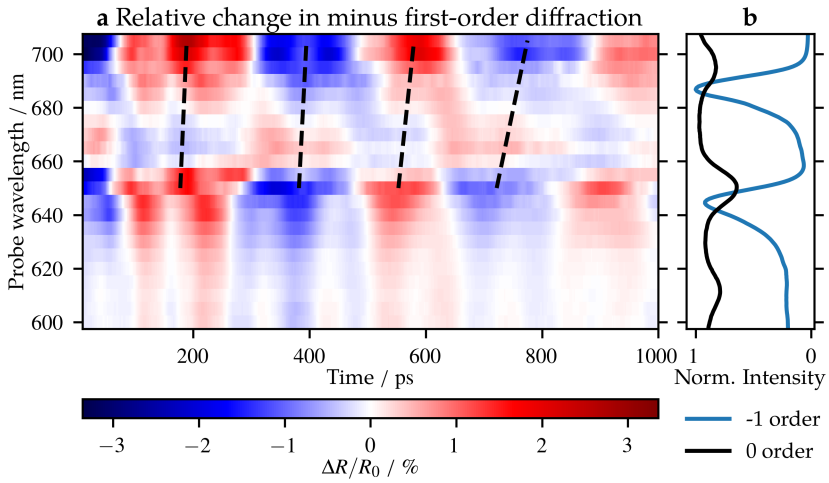

Figure 4.8: (a) Plot of the measured changes in minus first-order *diffraction* of probe light as function of time delay between pump and probe pulse, where the slowly decaying background is removed, for probe wavelengths between 600 nm and 705 nm. Indicated with black dashed lines is the increase in SAW period for increasing probe wavelength. (b) The ratio of measured *s*- and *p*-polarized reflection spectra and the minus first-order diffraction spectrum.

reflection spectrum and the minus first-order diffraction spectrum. At all probe wavelengths, the peaks due to the SAWs and the LWs are clearly observed at 2.6 and 9.5 GHz, respectively. For probe wavelengths around the two longer wavelength SPRs, between 640 and 655 nm, and between 690 and 695 nm, there are also strain waves observed with a frequency between 6.0 and 7.5 GHz. As discussed in Section 4.5.1, these frequencies have not yet been identified. We note that the measured frequency associated with the LWs, hints at a small shift from about 9.9 GHz to about 9.2 GHz, when the probe wavelength is increased from 665 nm to 680 nm. Finally, we compared the FFT amplitudes of the SAW and LW with the largest changes in the minus first-order diffraction, at a probe wavelength of 700 nm, with the FFT amplitudes of the measurement with the largest *reflection* changes, measured at 650 nm. We find that the SAW induced diffraction change is enhanced by an additional factor of about 2.4 and by a factor of about 2 for the LW. We note this is an enhancement in the relative change in diffraction, but that the absolute intensity of the diffracted light is at least one order of magnitude smaller than that of the reflection.

4.5.3 *Plus first-order diffraction measurements*

The strain-wave-induced changes in the *plus* first-order diffraction are very similar to those in the minus first-order diffraction. Therefore, Figure 4.10(a) directly shows the measured plus first-order diffraction changes as function of delay time for probe wavelengths between 600 nm and 700 nm, where the background has been removed in a similar manner as in previous 2D plots. Figure 4.10(b) shows the ratio of the *s*- and *p*-polarized reflection spectra and the plus first-order diffraction

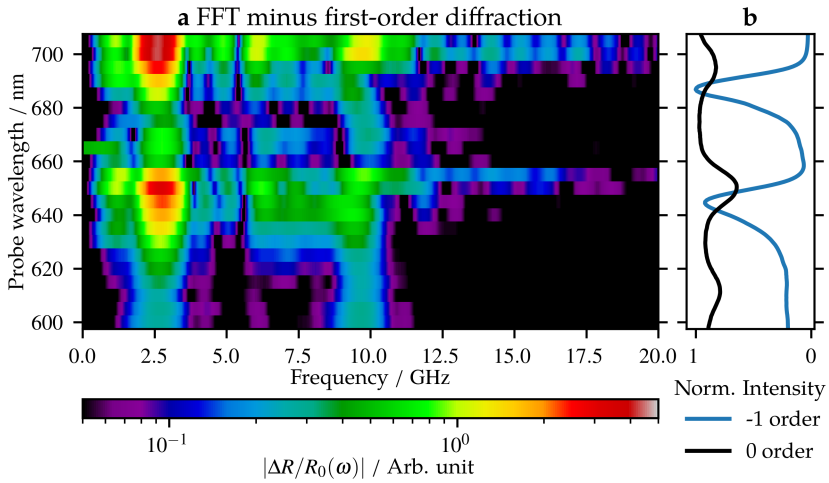

Figure 4.9: (a) Plot of the FFT of the measured changes in minus first-order diffraction of probe light, for probe wavelengths between 600 nm and 705 nm. (b) The ratio of measured *s*- and *p*-polarized reflection spectra and the minus first-order diffraction spectrum.

spectrum. When looking at how the diffraction changes between different probe wavelengths, we observe a similar trend as in the minus first-order diffraction measurements. For example, in the plus first-order diffraction measurements, a sign change of the SAW is observed, between the two shorter wavelength SPRs, at 620 nm and at 640 nm. In the minus first-order measurements, two sign changes are also observed, the first at 660 nm and the second at 680 nm, again in between two SPR wavelengths. We also note that the minus first-order diffraction spectrum has peaks at the two longer SPR wavelengths, at 645 nm and 687 nm, whereas the *plus* first-order spectrum has peaks around the two shorter SPR wavelengths, at 613 nm and 654 nm. Furthermore, the measurements with the probe wavelengths of 660 nm and 670 nm are completely opposite in sign, as is more clearly shown in Figure 4.11.

The FFT of the plus first-order time-dependent diffraction signals is shown in Figure 4.12(a). Figure 4.12(b) shows the reflection spectrum and the spectrum of the plus first-order diffracted beam. In Figure 4.12(a), at all probe wavelengths, signals at the two frequencies corresponding to the SAWs and the LWs are observed. Again, there are also still unidentified contributions to the signal at frequencies between 6 and 7.5 GHz. Similar to the minus first-order diffraction measurements, we see a hint of a shift in the frequency of the LW signal, when probing with a wavelength between the SPR wavelengths, between 625 and 645 nm. Here, the frequency shifts from about 9.9 to 9.4 GHz. The enhancement, when we compare the FFT amplitudes of the measurement with the largest plus first-order diffraction changes, at 670 nm, with the FFT amplitudes of the largest *reflection* changes (at a probe wavelength of 650 nm), is a factor of about 3.3 for the SAW and a factor of about 2.6 for the LW. Again, we note that these are measured as relative changes and

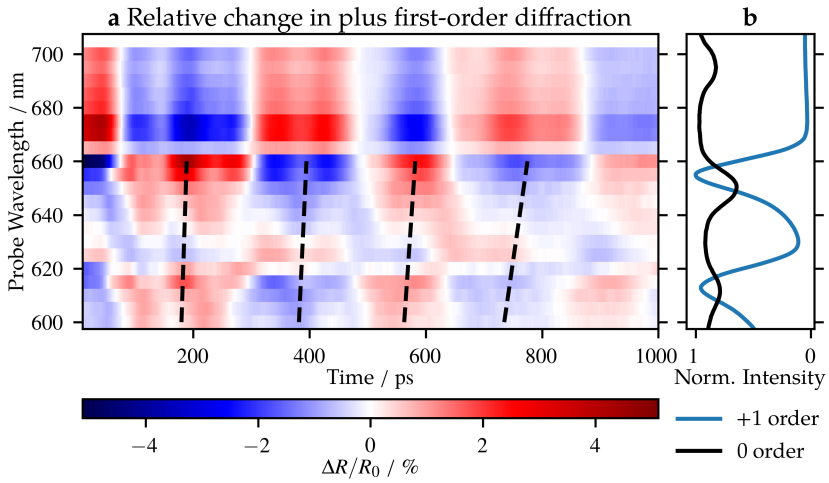

Figure 4.10: (a) Plot of the measured changes in *plus* first-order diffraction of probe light as function of time delay between pump and probe pulse, where the slowly decaying background is removed, for probe wavelengths between 600 nm and 700 nm. Indicated with black dashed lines is the increase in SAW frequency for increasing probe wavelength. (b) The ratio of measured *s*- and *p*-polarized reflection spectra and the plus first-order diffraction spectrum.

that the intensity of the diffracted light is at least one order of magnitude smaller than the intensity of the reflection.

4.6 DISCUSSION

In the experiments, we see two different dominant strain-wave frequencies, at about 2.6 and 9.5 GHz. As in our previous experiments, where we probed around a SPR with a non-segmented Au grating of similar Au layer thickness [17], we attribute the two frequencies to Surface Acoustic Waves (SAWs), excited on the short-period grating(s), and Longitudinal Waves (LWs), respectively. In the first part of this section, we discuss the generation and physical properties of the different waves. In the second part, we discuss how these strain waves can influence the probe signal.

4.6.1 *Strain waves*

Surface acoustic waves

Surface acoustic waves travel along a surface, and can be optically excited if there are spatially periodic inhomogeneities in either the excitation profile [64–66] or in the surface topography [60]. In similar, earlier experiments, we have concluded that the excited SAWs are likely to be shear waves [17]. This may have been wrong. The observed SAWs may in fact be Rayleigh waves. These propagate along the free surface of a solid, with a phase velocity typically somewhat lower than the transverse speed of sound [67]. Furthermore, they have both a longitudinal and a transversal motion component and their amplitude typically decays exponentially

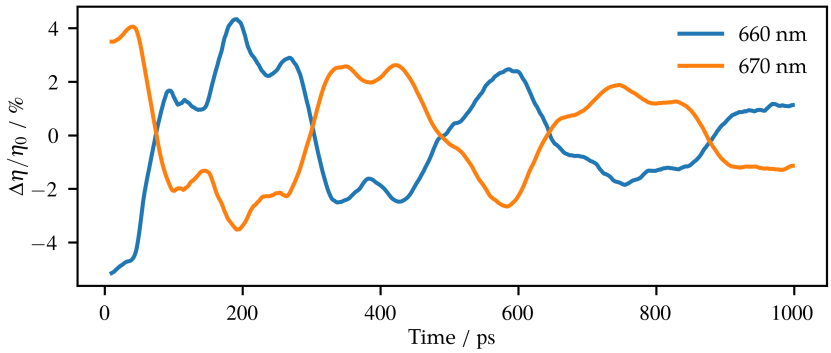

Figure 4.11: Comparison of the measured changes in plus first-order diffraction of probe wavelengths 660 nm and 670 nm, where the slowly-decaying background is removed, as function of pump-probe delay time.

with depth, at least for a single thick layer of material. The precise nature of these waves on our segmented grating containing multiple layers is currently not known.

In all experiments, we observe a SAW frequency of around 2.6 GHz. The time-domain data show that the SAW period is shorter for shorter probe wavelengths, and longer for longer probe wavelengths. This is indicated by black dashed lines in Figure 4.5a, Figure 4.8a, and Figure 4.10a. This is also observed in the second-order diffraction measurements (not shown). This behaviour was not seen in our earlier experiments on non-segmented gratings [17]. We note that the excitation conditions for the excitation of strain waves with the 400 nm pump pulse are identical for all measurements across different reflection and diffraction orders. However, rigorous numerical simulations are necessary to further investigate the different SAW frequencies. These simulations should include the excitation by the 400 nm pump pulse using near-field calculations, 2D election-energy diffusion, the time-dependent strain-wave formation and propagation on these square-wave gratings, and the diffraction of the probe pulse. This is currently beyond the scope of this paper in which we want to focus on LWs that may be used to detect buried gratings.

Longitudinal waves

Longitudinal waves are strain waves travelling between the free surface of the grating and the Au/SiO_2 interface. Due to the relatively large penetration depth of energy in the Au layer [15, 68], the 173 nm $\pm$ 3 nm thick Au layer heats up relatively homogeneously, even though the *optical* penetration depth is only a fraction of the layer thickness. The homogeneous heating leads to the generation of two strain waves, one at the Air/Au interface and another at the Au/SiO_2 interface, travelling in opposite direction. These two counter-propagating strain waves result in a standing wave, causing the layer to expand and contract. The frequency of the cycle of expansion and contraction is determined by dividing the speed of sound in Au by twice the thickness of the layer, $v_{Au}/2d_{layer}$, as both strain waves need to travel back to the same interface where they are generated. A measurement (shown in Section 4.C) on an unstructured part of the sample, where only LWs are excited,

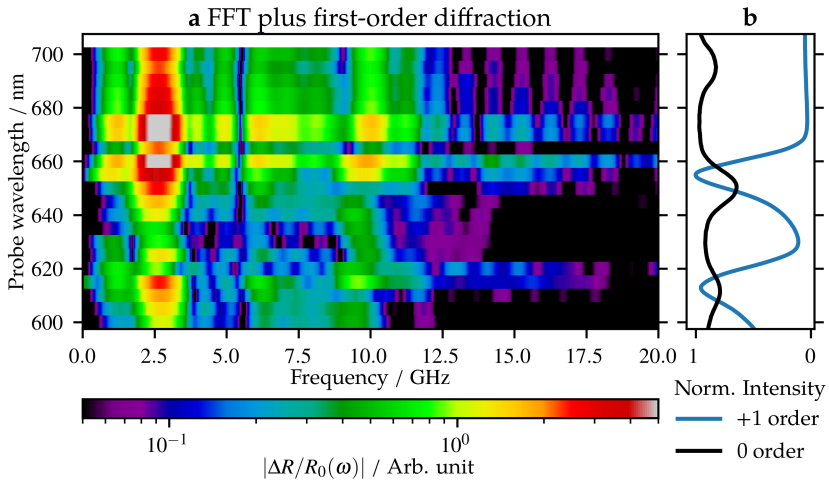

Figure 4.12: (a) Plot of the FFT of the measured changes in plus first-order diffraction of probe light, for probe wavelengths between 600 nm and 705 nm. (b) The ratio of measured *s*- and *p*-polarized reflection spectra and the plus first-order diffraction spectrum.

shows a frequency of 9.3 GHz $\pm$ 0.2 GHz. This matches with the peak at a frequency of about 9.5 GHz, supporting the identification of these waves as LWs.

4.6.2 *Strain-wave-induced reflection and diffraction changes*

Most types of strain waves change the density of the material as they propagate. In this case, strain waves change the material density of the Au and, as the electrons respond quasi-instantaneously [69], also the electron density, N_e. The change in electron density will shift the plasma frequency, given by $\omega_p = (e^2 N_e/\epsilon_0 m)^{1/2}$, where e is the electron charge, ϵ_0 is the vacuum permittivity, and m the effective electron mass. The shifting plasma frequency changes the relative permittivity of Au, and, according to Equation 4.4, the wavevector and the resonance wavelength of the SPP as well. Thus, strain waves can shift the central wavelength of an SPR [69–72]. They may also change the grating shape, such as its amplitude or grating line width.

As explained in [17], a strain wave affecting the central wavelength of an SPR can be recognized by a change in sign (or a π-phase shift) in the measured oscillation, when comparing a trace measured using a probe wavelength just below an SPR with one equal to or just longer than the SPR wavelength. This behaviour is also present in the segmented grating experiment for the frequencies associated with LWs, and is indicated by red arrows in Figure 4.4 and Figure 4.7, for the measured probe reflection and minus first-order diffraction changes, respectively. However, in the 2D plots, this is not clearly visible, as the LW oscillations are superimposed on the SAW oscillations, which are stronger. By spectrally filtering the obtained FFT spectra of the reflection and first-order diffraction changes to remove the SAW and transforming the filtered spectra back to the time domain, the sign changes

of these oscillations become more clearly visible. We have used a bandpass filter with a cut-on frequency of 8.5 GHz, just below the frequencies associated with the LWs at 9.5 GHz, and a cut-off frequency of 75 GHz, to suppress noise. Furthermore, the applied bandpass filter has sharp, but smooth transitions near the cut-on and cut-off frequencies, to reduce filtering artefacts.

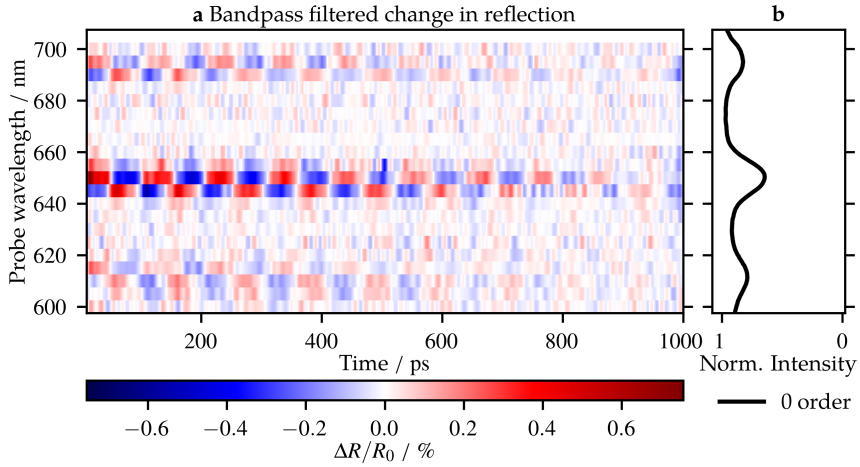

Figure 4.13: (a) Plot of the bandpass filtered changes in reflection, as function of time delay between pump and probe pulse, for probe wavelengths between 600 nm and 700 nm. Cut-on frequency: 8.5 GHz, cut-off frequency: 75 GHz. (b) The ratio of measured *s*- and *p*-polarized reflection spectra.

Figure 4.13(a) and Figure 4.14(a) show the bandpass filtered, time-dependent signals for all probe wavelengths, for the reflection and the plus first-order diffraction, respectively. Again, Figure 4.13(b) shows the reflection spectrum and Figure 4.14(b) shows both the reflection and plus first-order diffraction spectra. Starting with the filtered reflection changes (Figure 4.13(a)), we observe two clear sign changes, at probe wavelengths of 650 nm and 695 nm, and a third, much fainter one at 615 nm. These probe wavelengths are equal to, or just longer than, the SPR wavelengths of 611 nm, 650 nm, and 695 nm. In Figure 4.14, where the filtered plus first-order signals are shown, four sign changes are observed, at the probe wavelengths of 610 nm, 625 nm, 650 nm, and 665 nm. Of these, 610 nm and 650 nm are very close to SPRs, but the other two are not. Furthermore, the *absence* of sign changes for the bandpass filtered signals in the probe wavelength range of 680 nm to 700 nm is also surprising. In Section 4.4, we have explained that the peaks in the diffraction spectra can be explained by the multiple angular spatial frequencies present in the segmented grating, if we assume that SPPs excited through one grating can couple out through another. In our analysis, SPPs do not couple out in the direction of the plus first-order diffraction spectrum for wavelengths between 680 nm and 700 nm. Thus, at wavelengths where we observe a sign change associated with an SPR in the *reflection* measurements, we do not always observe this change in sign in the plus first-order diffraction at the same probe wavelengths. A similar behaviour is observed in the bandpass filtered minus first-order signals (not shown) in the

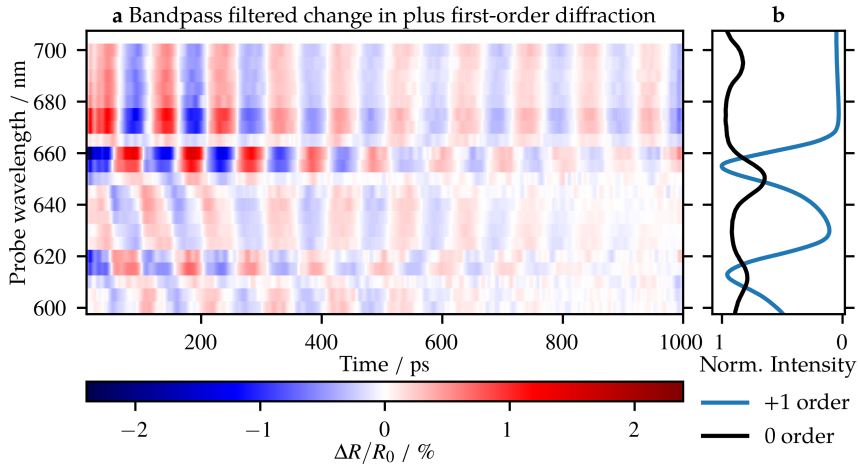

Figure 4.14: (a) Plot of the bandpass filtered changes in plus first-order diffraction, as function of time delay between pump and probe pulse, for probe wavelengths between 600 nm and 700 nm. Cut-on frequency: 8.5 GHz, cut-off frequency: 75 GHz. (b) The ratio of measured *s*- and *p*-polarized reflection spectra and the plus first-order diffraction spectrum.

wavelength range of 610 nm to 630 nm, where the reflection measurements show a sign change.

When comparing the starting phases of identical probe wavelengths of the bandpass filtered reflection and plus first-order diffraction signals, we observe another interesting feature. For example, the signal at the probe wavelength of 645 nm starts with a relative decrease in reflection, but shows an increase in the plus first-order diffraction. At 650 nm, where the sign is changed in both reflection and plus first-order diffraction, the reflection increases and the plus first-order decreases. This inverse behaviour of reflection and diffraction signals at the same wavelength is also observed near the probe wavelengths of 615 nm in the plus first-order diffraction and near the sign changes at 650 nm and 695 nm of the minus first-order (not shown). Thus, for LWs, we see that an decrease in reflection correlates with an *increase* in diffraction for probe wavelengths near SPRs, and we conclude that the reflection decreases and the diffraction increases as more light is coupled to SPPs, for probe wavelengths close to SPRs. We note that the *relative* changes in diffraction can be greater than the relative changes in reflection, but that the *absolute* changes in reflection are larger, as the unperturbed reflection is much larger than the unperturbed diffraction efficiency. For example, at the probe wavelength of 655 nm, the measured, unperturbed reflection at this wavelength is about 70 % and the measured, unperturbed diffraction efficiency, η_0, is about 3 %. Furthermore, the diffraction efficiency changes drastically as the probe wavelength changes, meaning that the large relative changes in diffraction, at probe wavelengths 670 nm and 675 nm are not as large as those around 655 nm, in absolute terms.

Strain waves can also affect the reflection and diffraction due to changes of the grating shape. If the grating shape change is known, the resulting changes in reflection and diffraction can also be calculated with the RCWA code. As an

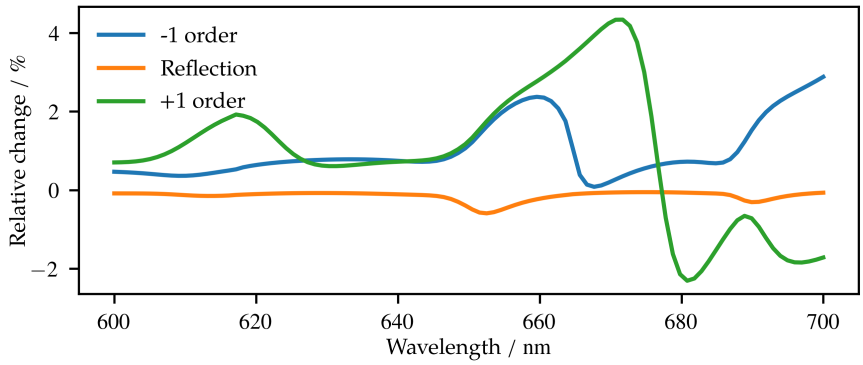

Figure 4.15: Calculated relative reflection and diffraction changes for a 100 pm increase in grating amplitude, as a function of probe wavelength.

example, Figure 4.15 shows the calculated, relative change in reflection and first-order diffraction as a function of wavelength, assuming a 100 pm increase in grating amplitude. The increase in grating amplitude yields a decrease in reflection, for all wavelengths. Furthermore, the decrease is largest at about 613 nm, 652 nm, and 690 nm. These are just a bit longer than the SPR wavelengths calculated with the RCWA code at 608 nm, 650 nm, and 688 nm. For the minus first-order diffraction, the diffraction increases for all wavelengths calculated, and the relative increase peaks at 660 nm and 700 nm, where the calculated, absolute diffraction efficiency is very low (see Figure 4.2(b)). Similar peaks are observed around 617 nm and 670 nm in the relative change in plus first-order diffraction efficiency. Again, the calculated, absolute diffraction efficiency is very low for these wavelengths. Surprisingly, the change in plus first-order diffraction quickly becomes negative for wavelengths longer than 677 nm.

It is unlikely that actual strain waves will uniformly change the grating amplitude, as we have used in the calculations, but the calculations illustrate that a grating deformation can result in opposite behaviour at different probe wavelengths within the same (non-zero) diffraction order. In other words, the effect of a grating shape change, in this example a height increase, does not give a diffraction increase for all wavelengths. For a more detailed understanding, finite element methods could potentially be used to calculate (time-dependent) grating deformations, which could be used as input for RCWA calculations to determine the changes in reflection and diffraction, perhaps even including the change in permittivity induced by strain.

4.7 CONCLUSION

We have studied the strain-wave-induced reflection and diffraction changes of a segmented grating, as a function of pump-probe delay time. The segmented grating consists of a short-period grating modulated by a longer-period grating, leading to two sidebands in the spatial frequency domain around the angular spatial frequency of the short-period grating. SPPs can be excited on the small-period grating and on the two 'sideband' gratings, leading to three separate SPRs. The presence of

three gratings leads to strongly enhanced diffraction off the longer-period grating, for wavelengths close to the SPR wavelengths. This is caused by SPPs re-scattering light in the same direction as light directly diffracted off the longer-period grating.

The time-dependent, strain-wave-induced reflection and diffraction changes were studied using probe light with wavelengths covering the three SPRs on the segmented grating. In reflection, the strongest strain-wave-induced oscillatory signals were observed at the SPR wavelengths. SAWs and LWs were identified by their frequency. In reflection, the enhancement when probing near SPR wavelengths was about a factor of 23 for SAWs and 36 for LWs, respectively. In the first-order diffraction measurements, oscillatory signals similar to the reflection measurements were observed, but the relative changes of the diffraction signals were larger by a factor of 3.3 for SAWs and by a factor of 2.6 for LWs, compared to the reflection measurements.

4.A EXPERIMENTAL SETUP

A schematic view of the experimental setup is shown in Figure 4.1(a). The output of an amplified Ti:Sapphire laser system (Astrella, Coherent) with a repetition rate of 1 kHz, a pulse length of about 35 fs, a central wavelength of 800 nm and a pulse energy of 6 mJ is split into two beams using an 85:15 (R:T) beam splitter.

The transmitted, weaker part of the beam is frequency doubled to 400 nm using a BBO crystal. It is reflected by several dichroic mirrors to filter out residual 800 nm light and passes a computer-controlled variable optical delay line. A mechanical chopper, synchronized with the 1 kHz pulse train, blocks every other pulse, reducing the repetition rate to 500 Hz. A lens is used to weakly focus the light onto the sample, such that the spot diameter is about 500 μm. The pump light is *p*-polarized, perpendicular to the grating lines, and incident at an angle of about 7° with respect to the surface normal. The pump light does *not* excite SPPs.

The reflected, stronger part of the output of the laser system is used as input for a three-stage optical parametric amplifier (OPA, TOPAS, Light Conversion). We tune the output of the OPA in a range from 1200 to 1410 nm. Another BBO crystal is used to frequency-double this to a range of 600 to 705 nm. Using a lens ($f = 20\,\text{cm}$), the probe beam is weakly focused onto the sample, to an elliptic spot with axes of about 140 μm and 80 μm. The probe light is also *p*-polarized and incident at an angle of approximately 27° with respect to the surface normal. For this incident angle, the probe pulse excites SPPs on the sample at wavelengths of approximately 611 nm, 650 nm, and 695 nm. The fluence of the pump pulse is 8.5 mJ cm^{-2}, about 60 % of the energy is absorbed by the sample.

The probe beam diffracts off the 6020 nm period grating and several diffraction orders are present. An aperture selects one order, which is collimated by a lens and is used to illuminate a blazed grating (GR25-1205, Thorlabs). The diffracted light is focused onto a movable slit. Using the slit, only a 1.5 nm to 2.0 nm wide band of wavelengths is transmitted to the photodiode detector (PDA100A2, Thorlabs), out of the full 15 nm FWHM bandwidth of the frequency-doubled pulses from the OPA. As an example, Figure 4.16 shows the unfiltered spectrum of a 687 nm central wavelength pulse from the frequency-doubled OPA output, together with six filtered probe spectra, all normalized to their individual maximum. The (specular) reflected, and the plus and minus first-order diffracted beams were measured as

a function of time delay between the pump and probe pulses. Within the broad spectrum of the probe pulse, of which the central wavelength is varied through adjustment of the OPA, five to six wavelength intervals of 2 nm are sequentially measured. The energy of the probe pulse was adjusted when the central wavelength of the output of the OPA was changed, but was kept constant when measuring within the bandwidth of the frequency-doubled output of the OPA.

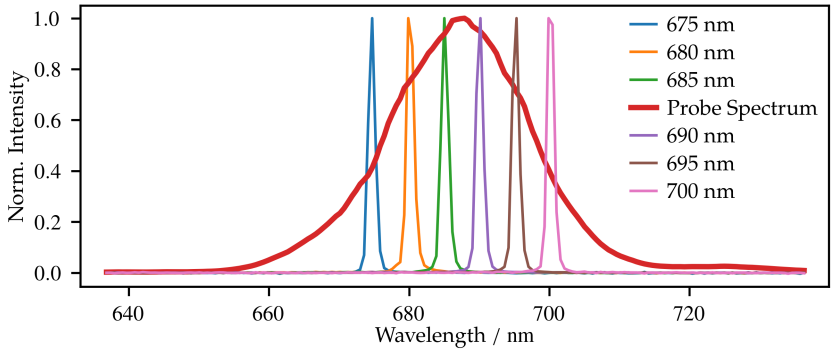

Figure 4.16: Example of the unfiltered probe spectrum (red line), with a 687 nm central wavelength, together with six probe spectra, obtained by filtering the original probe spectrum. All curves have been normalized to their maximum.

White light spectroscopy is performed using a fibre-coupled broadband white light source (AVALIGHT-HAL-S-MINI, Avantes) and a fibre-coupled spectrometer (AVASPEC-ULS-RS-TEC, Avantes). The light, coming from the white light source, is collimated (in free space), and passes through a wire-grid polarizer. It is focussed onto the sample, at an angle of about 27°, similar to the incident angle of the probe pulse in the photo-acoustic experiments. The polarizer allows us to investigate the difference between *s*- and *p*-polarized incident light, as only *p*-polarized light can excite SPPs. Using an aperture, a single diffraction order is selected, that is collimated and coupled into the fibre going to the spectrometer.

4.B LIGHT COUPLING TO SURFACE PLASMON POLARITONS

In Au, the angular wave number of SPPs, $k_{SPP} = |\bar{k}_{SPP}|$, for optical frequencies corresponding to a wavelength of 600 nm or longer, can be approximated by [31]:

$$k_{SPP} \approx \frac{\omega}{c}\sqrt{\frac{\epsilon'_{Au}\epsilon_{env}}{\epsilon'_{Au}+\epsilon_{env}}}, \tag{4.4}$$

where ω is the optical angular frequency, c the speed of light, ϵ'_{Au} is the real part of the permittivity of Au at ω, and ϵ_{env} is the permittivity of the environment, which is $\epsilon_{env} \approx 1$ for air.

Figure 4.17 shows a drawing of how SPPs are excited using a grating. Propagating light, incident at angle θ_{in} with respect to the surface normal, can be coupled to SPPs if the following condition is met [31]:

$$k_{SPP} = k_0 \sin\theta_{in} + mk_g, \tag{4.5}$$

where $k_0 \sin\theta_{\text{in}} = k_x$ is the projection of the wavevector of the incident light, $\bar{k}_0$, onto the sample surface, $k_0 = |\bar{k}_0| = 2\pi/\lambda$ is the wavenumber, $k_g = 2\pi/\Lambda_g$ is the angular spatial frequency of the grating with period Λ_g, and m is an integer. For our sub-wavelength period plasmonic gratings and used wavelengths, usually $m = -1$.

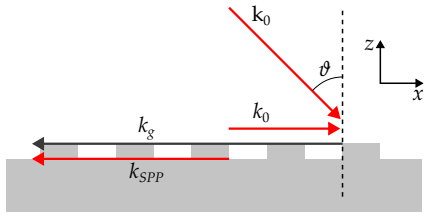

Figure 4.17: Schematic drawing of the excitation of SPPs by light, incident at an angle θ_0 with the z-axis, and with wave vector k_0 using a sub-wavelength grating with angular spatial frequency k_g. k_x is the projection of $\bar{k}_0$ onto the surface.

The segmented grating consists of a plasmonic grating ($\Lambda_{p1} = 2\pi/k_{p1} = 430\,\text{nm}$) and is modulated by an alignment grating ($\Lambda_A = 2\pi/k_A = 6020\,\text{nm} = 14\Lambda_{p1}$). The height of such a segmented grating as a function of the position x, assuming a 50 % duty cycle and a perfect square grating, can be written as:

$$f_{\text{sg}}(x) = \frac{h}{4}(1 + f_{p1}(x))(1 + f_A(x)), \tag{4.6}$$

where

$$\begin{aligned} f_{p1}(x) =& \frac{4}{\pi} \sum_{n=1,3,5,\ldots} \frac{\sin(nk_{p1}x)}{n} = \\ =& \begin{cases} +1 & \text{for } l\Lambda_{p1} < x < (l + \frac{1}{2})\Lambda_{p1}, \\ 0 & \text{for } x = \frac{1}{2}l\Lambda_{p1}, \\ -1 & \text{for } (l + \frac{1}{2})\Lambda_{p1} < x < (l+1)\Lambda_{p1}, \end{cases} \\ & \text{where } l = 0, \pm 1, \pm 2, \cdots \text{ in all cases,} \end{aligned} \tag{4.7}$$

and

$$\begin{aligned} f_A(x) =& \frac{4}{\pi} \sum_{n=1,3,5,\ldots} \frac{\sin(nk_A x)}{n} = \\ =& \begin{cases} +1 & \text{for } l\Lambda_A < x < (l + \frac{1}{2})\Lambda_A, \\ 0 & \text{for } x = \frac{1}{2}l\Lambda_A, \\ -1 & \text{for } (l + \frac{1}{2})\Lambda_A < x < (l+1)\Lambda_A, \end{cases} \\ & \text{where } l = 0, \pm 1, \pm 2, \cdots \text{ in all cases,} \end{aligned} \tag{4.8}$$

are the Fourier series describing the square gratings with angular spatial frequencies k_{p1} and k_A, respectively. By using only the lowest order terms of both series, Equation 4.6 can be approximated by:

$$\begin{aligned} f_{\mathrm{sg}}(x) &\approx \frac{h}{4}[1+\frac{4}{\pi}\sin(k_{p1}x)][1+\frac{4}{\pi}\sin(k_A x)] = \\ &= \frac{h}{4}[1+\frac{4}{\pi}\sin(k_{p1}x)+\frac{4}{\pi}\sin(k_A x) \\ &\qquad +\frac{16}{\pi^2}\sin(k_{p1}x)\sin(k_A x)]. \end{aligned} \tag{4.9}$$

Here, the first two sines after the last equal sign represent the original gratings. The cross-term is the result of the modulation (multiplication) of the plasmonic grating by the alignment grating. This term can be rewritten as:

$$\begin{aligned} \sin(k_{p1}x)\sin(k_A x) = \frac{1}{2}\{&\cos[(k_A-k_{p1})x] \\ &-\cos[(k_{p1}+k_A)x]\}. \end{aligned} \tag{4.10}$$

The modulation thus leads to two additional angular spatial frequencies, $k_{p2} = |k_A - k_{p1}|$ and $k_{p3} = |k_{p1} + k_A|$. This is mathematically similar to the generation of sidebands in radio-frequency amplitude modulation. Furthermore, as $k_{p1} = 14k_A$ (i.e. the plasmonic angular spatial frequency is the 14^{th} harmonic of the alignment angular spatial frequency), the sidebands are at $k_{p2} = 13k_A$ and $k_{p3} = 15k_A$, which can also been seen as the 13^{th} and 15^{th} harmonic of the alignment angular spatial frequency.

Light can couple in on all gratings present at the Au surface, as long as Equation 4.5 holds. For the segmented grating, this means that light can couple to SPPs using the three gratings with angular spatial frequencies k_{p1}, k_{p2}, and k_{p3}.

Using Equation 4.5 and using the permittivity for Au, calculated from the n- and k-values obtained via ellipsometry, light with a wavelength of 650 nm couples to SPPs on the grating with angular spatial frequency k_{p1} (which is the *original*, non-segmented plasmonic grating) for an incident angle of 27.7°, with respect to the surface normal. Using this incident angle, the wavelengths required to couple light to SPPs on the two other plasmonic 'sideband' gratings can be calculated. For the same incident angle, this leads to SPR wavelengths at 612 nm (for k_{p2}) and 695 nm (for k_{p3}). Table 4.1 lists the grating spatial frequencies expressed in terms of the long period alignment grating k_A, the corresponding spatial period, and the calculated and measured SPR wavelength.

The calculated SPR wavelengths are close to the measured ones. The incident angle used in the calculation (27.7°) is slightly different from the incident angle in the measurement (27°). This difference may be due to the fact that, strictly speaking, Equation 4.5 is only valid for flat surfaces and is only a good approximation for grating amplitudes smaller than about 7 nm [33].

4.C TRANSIENT GRATING MEASUREMENT

Since we had some doubts about the accuracy with which the thickness of the Au layer was initially determined, an additional measurement on the flat part

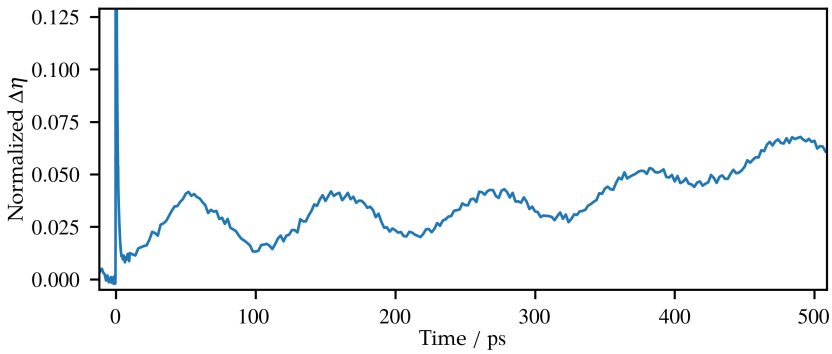

Figure 4.18: Measured time-dependent diffracted signal from an unstructured part of the sample, after excitation by two synchronized 400 nm pulses, creating a transient grating. The measured diffraction is normalized to the electron peak at 0 ps delay.

of the sample, where no grating is present, was performed. Figure 4.18 shows the measured, normalized, time-dependent diffraction, η, of a 655 nm pulse, after excitation by *two* 400 nm pump pulses. These pulses create a transient grating at the sample, with a pitch of about 3 µm. The measurement shows an oscillatory signal with a period of 107 ps $\pm$ 2 ps, corresponding to a frequency of 9.3 GHz $\pm$ 0.2 GHz. This corresponds to the LW frequency measured at the segmented grating. We are thus led to conclude that the thickness of the Au layer is 172 nm $\pm$ 3 nm, assuming the speed of sound in the layer is still 3240 m s^{-1}, rather than the 192 nm that was measured using a profiler (Tencor P-7, KLA).

5

WAVELENGTH-DEPENDENT OPTICAL DETECTION OF STRAIN WAVES NEAR INTRINSIC AND ARTIFICIAL OPTICAL RESONANCES

ABSTRACT

Laser-induced, ultrafast strain waves are potentially interesting for subsurface metrology in the semiconductor industry. These waves are commonly detected by measuring their effect on the reflectance of a material. The changes in reflectance are typically small, making detection difficult. In this letter, we compare the strain-wave-induced changes in reflectance at and around an interband transition and a surface plasmon polariton resonance. Both are present on an Au-covered segmented grating, at different wavelengths. Using a white light continuum probe pulse, we measure the ultrafast reflectance changes over a broad wavelength range. We find that the strain-wave-induced changes at the interband transition are only about 37 % smaller than those measured with probe wavelengths close to a surface plasmon polariton resonance. This contrasts with the different appearance of the surface plasmon polariton resonance and the interband transition in the static reflectance spectrum of the sample. Our results show that the static reflectance spectrum is not a good predictor for the strain-wave-induced reflectance changes and emphasize the importance of experiments to find the optimum wavelength to detect strain waves.

This chapter has been published, in modified form, in Optics Letters, Vol. 50, Issue 5, 1445-1448 (2025) [18]

5.1 INTRODUCTION

Ultrafast strain waves, generated and detected with ultrashort optical pulses [12, 62], can penetrate optically opaque layers to measure layer thickness [73] and detect subsurface structures [74, 75]. This hybrid optical and acoustic technology is a promising candidate for subsurface metrology in the semiconductor manufacturing industry, for example, for wafer alignment [4, 15]. Unfortunately, achieving the signal-to-noise ratio (SNR) required for the detection of strain waves in these applications is challenging. Strain waves can dynamically alter the complex refractive index of a material and, thus, its reflectance, which can be measured using an ultrashort laser pulse. However, the magnitude of these changes may be small or even non-existent for specific probe wavelength and acoustic frequency combinations [76].

Interestingly, strain-wave-induced reflectance changes can non-trivially depend on the probe wavelength, which may provide an easy path towards increasing signal strength. Probing with wavelengths close to the interband transition (IBT) in aluminium, for example, has shown to dramatically modify the strain-wave-induced reflectance changes [77]. A similar, strong wavelength dependence in the detection of strain waves has also been observed when probing close to surface plasmon polariton resonances (SPRs). Surface plasmon polaritons are collective oscillations of free electrons in a metal, coupled to an electromagnetic wave. They can be used to enhance the detection of strain waves on, for example, flat surfaces [78, 79] or metallic gratings [17]. Although the latter require on surface modifications, they have an advantage over the intrinsic IBT: They can be tailored to be resonant for a specific (optical) wavelength range.

For metrology applications, however, a quantitative analysis of the enhancements due to the naturally occurring IBTs and the 'artificial' SPRs is essential. This is challenging, as it should ideally be conducted using a single sample under the same experimental conditions. Such a comparison is also interesting because the two resonances manifest themselves differently in the linear reflectance spectrum of gold. The IBT shows up as a gradually decreasing reflectance when the wavelength decreases from 600 nm to 475 nm, while the SPR has a sharp dip in the reflectance.

In this chapter, we show the strain-wave-induced changes in reflectance of an Au-covered segmented grating, for probe wavelengths between 465 nm and 755 nm. This wavelength range simultaneously covers the IBT of Au at approximately 520 nm (2.4 eV, [80]) and three SPRs at 615 nm, 652 nm, and 695 nm [47] (2.0 eV, 1.9 eV, and 1.78 eV, respectively).

We observe time-dependent oscillatory changes in reflectance near both the IBT and near the SPRs, that correspond to a 9.5 GHz longitudinal wave (LW) excited by the pump pulse. The largest change in the reflectance is measured on the *slope* of the SPR, at a wavelength of 649 nm. Near the IBT, the amplitude of the reflectance has a maximum at a probe wavelength of 510 nm (2.43 eV), and the amplitude is about 37 % smaller than that measured close to the SPR. This difference in the strain-wave-induced reflectance changes measured around the SPR and IBT contrasts with the large difference in shape of the static reflectance spectrum around these optical resonances. It shows that for resonances that have different physical origins, the static reflectance spectrum is not a good predictor of the relative strength of the optical changes induced by the strain waves. It thus highlights the need

to perform wavelength-dependent measurements to maximize the strain-wave-induced reflectance changes.

5.2 EXPERIMENTAL METHODS

The sample is a segmented grating, similar to what is sometimes used in the semiconductor industry for wafer alignment. The grating is covered by 172 nm of Au, and is shown schematically in Figure 5.1B and C. The segmented grating is a short-period grating ($\Lambda_{SPP} = 430\,\text{nm}$), capable of sustaining surface plasmon polaritons (SPPs) in the visible, amplitude modulated with a long-period grating ($\Lambda = 6020\,\text{nm}$). Due to the amplitude modulation, the grating also contains "side-band gratings" at the sum and difference spatial frequencies of the two gratings [47]. At these sidebands, SPPs can also be excited, giving a total of *three* SPRs, at 615 nm, 652 nm, and 695 nm, in line with earlier experiments, for *p*-polarized light with an angle of incidence (AOI) of 26° with respect to the surface normal. The SPRs can be seen as dips in the reflectance of the sample as shown in Figure 5.6B.

In the experiments, 400 nm pulses, with a peak fluence of about $6.2\,\text{mJ}\,\text{cm}^{-2}$, generate strain waves in the sample. The pump polarization is parallel to the grating lines and cannot excite SPPs on the sample.

The 1200 nm output of an optical parametric amplifier (OPA) is focussed into a 2 mm thick barium fluoride (BaF_2) crystal to generate a white light continuum (WLC) probe pulse. Figure 5.1A shows a part of the spectrum of a typical WLC pulse. A broadband beam splitter, reflecting about 70 %, splits the WLC into two, where the transmitted part is measured as a reference spectrum. The reflected part is focussed onto the sample, such that the probe spot diameter is about 6.5 times smaller than the pump. The probe AOI is about 26° with respect to the surface normal, in the plane perpendicular to the grating lines, as shown schematically in Figure 5.1B. The reflection from the sample is collimated and measured by the spectrometer. Any probe light *diffracted* from the sample is blocked. The spectrometer is build around a high-speed CMOS camera (Andor Zyla 4.2 PLUS, Oxford Instruments). More information about the setup can be found in Section 5.A, and about the data processing in Section 5.B.

5.3 RESULTS AND DISCUSSION

In Figure 5.2A, we plot the pump-induced relative changes in reflectance as a function of probe wavelength, for pump-probe delays between −5 ps and +10 ps In this time window, the large and rapid changes in reflectance, followed by a slower decay, are caused by electron gas heating and cooling [24]. We note that a clear positive chirp is visible, as there is a wavelength-dependent shift in time of the abrupt reflectance change toward more negative delays, for decreasing probe wavelength.

Despite the chirp, the individual wavelength components are still able to probe a rapid (rise time <300 fs) change in reflectance when the pump pulse arrives. For the shortest wavelengths, up to 510 nm, the reflectance rapidly increases by up to 25 %, and then decays almost linearly to an increase of about 2.5 % at 10 ps. For wavelengths between 510 nm and 600 nm, the reflectance initially *decreases* by up to

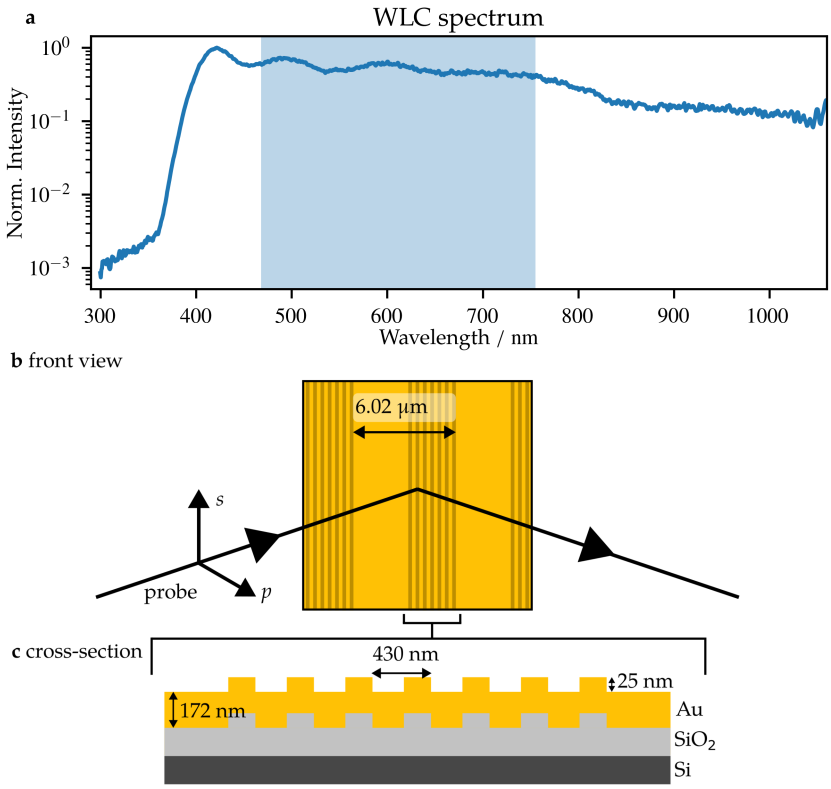

Figure 5.1: A. Visible part of the WLC spectrum, the shaded area indicates the wavelength range used in the experiments. B. Front view of the segmented grating, on which the probe light is incident. C. Schematic cross-section of the sample.

15 %, before recovering to a decrease of about 1 %, which is consistent with earlier results [25, 81]. The zero-crossing between the positive and negative changes in reflectance shifts from 510 nm to 500 nm in this time interval. The change in sign of the reflectance change as a function of wavelength around the IBT, is caused by *Fermi smearing* [25, 81–84].

For wavelengths longer than 600 nm, the initial change in reflectance is still negative, but its amplitude decreases with increasing wavelength: The effects of Fermi smearing decrease as the photon energies become (much) smaller than the IBT threshold energy [81]. Furthermore, the initial reflectance change appears to recover faster for longer wavelengths.

The heating of the electron gas also affects the three SPRs: Figure 5.2B shows both the static reflectance spectrum, and the reflectance spectrum 500 fs after the pump pulse, for wavelengths between 590 nm and 715 nm. The absorption dips in the reflectance spectrum become a bit more shallow and their central wavelengths shift to slightly longer wavelengths, as is shown in the inset. The change in shape is commonly attributed to a change in the imaginary part of the dielectric function of the metal, whereas the shift is attributed to a change in the real part [58, 85, 86].

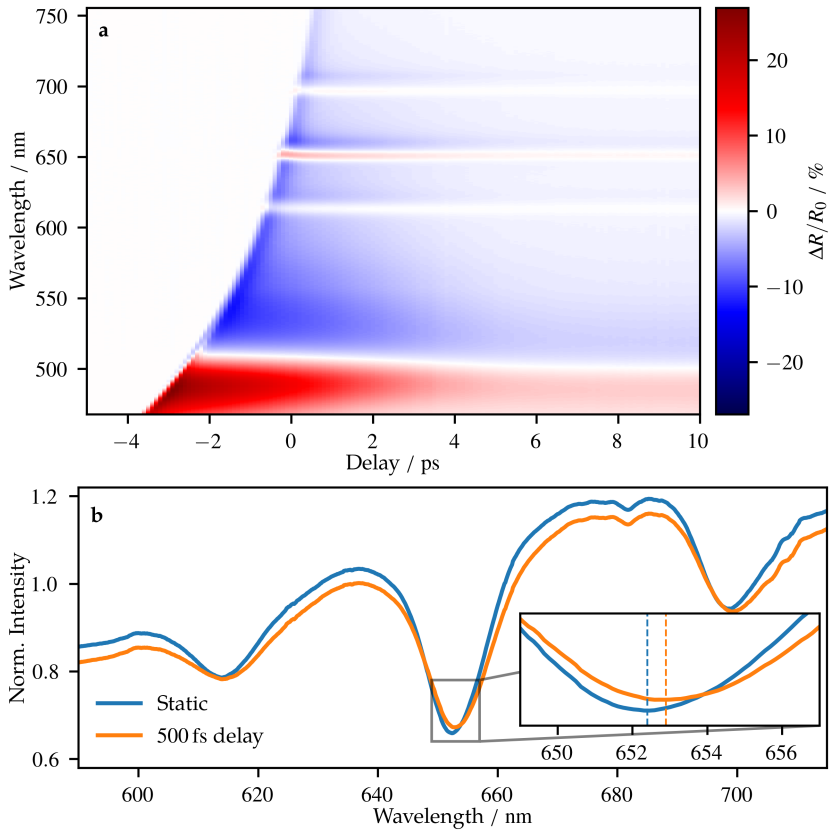

Figure 5.2: A. Relative change in reflectance as function of pump-probe time delay and probe wavelength. B. Part of the static and pumped (delay 500 fs) reflectance spectrum, normalized by the reference spectrum. The inset highlights the change in shape and central wavelength of the SPR.

After a few ps, the changes have mostly decayed, the residual change in reflectance is due to the lattice heating.

The remaining energy in the lattice dissipates into the substrate over several nanoseconds, resulting in a slowly decreasing reflectance change, present at all wavelengths. This thermal background masks the fast strain-wave-induced reflectance changes. To show these, we filter the reflectance changes using an 8^{th}-order high-pass zero-phase digital Butterworth filter, with a cut-off frequency of 6 GHz. This also removes the low-frequency surface acoustic wave (SAW) [47] as we focus only on the LWs.

Figure 5.3 shows the filtered reflectance changes as a function of probe wavelength and pump-probe delay time, on a timescale of 700 ps. Strain-wave-induced oscillations in the reflectance, with a period of 105 ps, are visible for probe wavelengths shorter than 550 nm and near the three SPRs, at 615 nm, 650 nm, and 695 nm. The oscillation period of 105 ps matches the roundtrip time of the longitudinal acoustic wave in the 172 nm thick Au layer [47]. Around all three SPRs, the phase

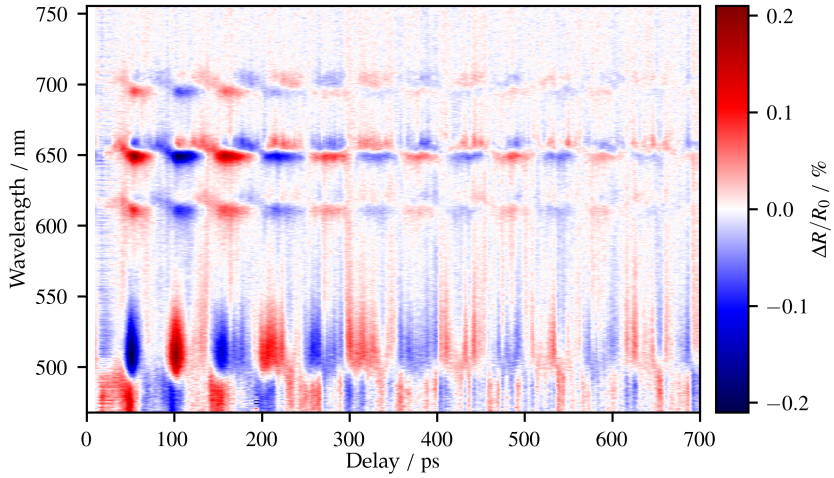

Figure 5.3: High-pass filtered reflectance changes for *p*-polarized probe light as a function of pump-probe time delay and probe wavelength. A 5 × 5 smoothing filter has been applied.

of the oscillation changes abruptly when the wavelength changes from below to above each resonance. Interestingly, a similar phase jump is present near the IBT, at about 500 nm.

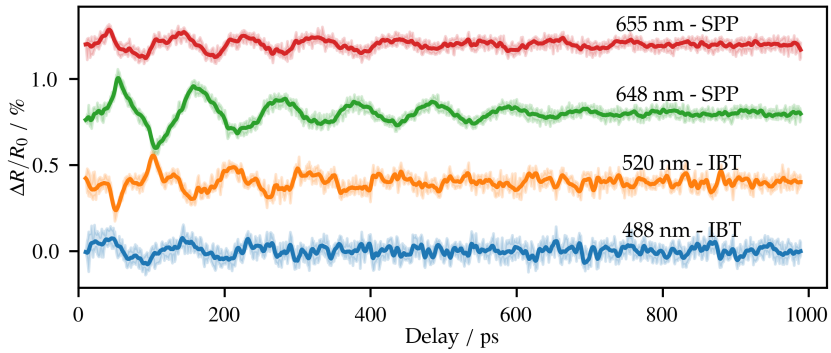

Figure 5.4: High-pass filtered reflectance changes of selected wavelengths, the shaded area indicates the minimum and maximum values of the 5 wavelengths closest to the indicated wavelength. The curves are offset for visibility.

In Figure 5.4, we plot the reflectance changes as a function of delay time for probe wavelengths of 480 nm, 520 nm, 648 nm, and 655 nm. Each curve is the average of five wavelengths closest to, and including, the indicated wavelength, and the maximum and minimum values within those pixels are shown by the shaded areas. The figure highlights that the oscillations of the reflectance changes measured on either side of the resonance or transition have an almost opposite phase.

For small delays (< 250 ps), the reflectance change at 648 nm is a more or less triangularly shaped wave, indicating that it consists of the fundamental longitudinal

mode and odd higher modes [87]. Only the odd modes are excited because the thermal stress in the layer is nearly constant as a function of depth [88]. The latter is caused by the rapid transfer of absorbed energy from close to the surface, deeper into the layer due to ballistic electron transport and electron energy diffusion [25]. Interestingly, the reflectance change measured at 520 nm, with photon energies just below the IBT threshold energy, has a different temporal shape.

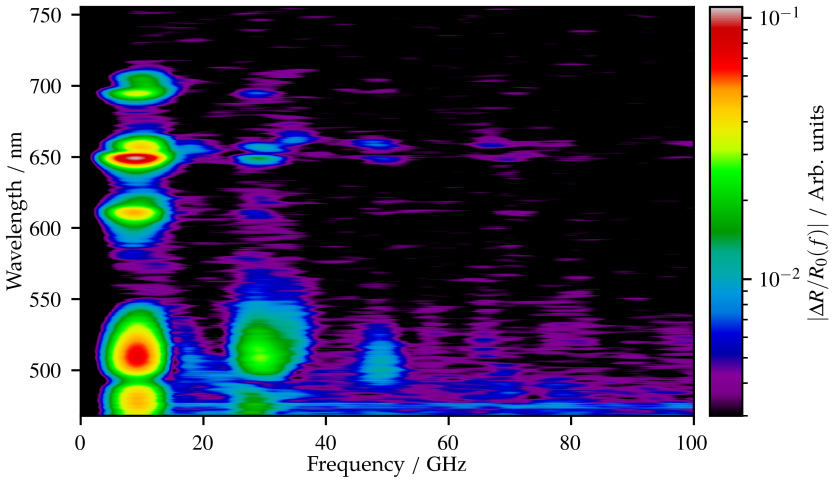

Figure 5.5: Amplitude of the reflectance changes in the first 300 ps as a function of strain-wave frequency and probe wavelength. A 5 × 5 smoothing filter has been applied.

Figure 5.5 shows the fast Fourier transform (FFT) of the first 300 ps of the reflectance changes of all measured wavelengths, for *p*-polarized light. A Hann window is used to reduce windowing artefacts. We measure the highest amplitude for the fundamental LW frequency of 9.5 GHz at 649 nm, on the short-wavelength side of the strongest SPR at 650 nm. The strain-wave-induced reflectance changes at the other two SPRs also show a larger amplitude on the short-wavelength side.

Naively, we would expect a π phase shift when comparing the probe wavelengths below and above the SPRs. Instead, we measure a 0.7π phase shift, for each of the three resonances. The most likely explanation for this is that the strain wave changes the complex dielectric function by some complex value $\delta\epsilon$. The real part of $\delta\epsilon$ affects the central wavelength of the SPR. A shifting central wavelength can result in opposite reflectance changes on either side of the SPRs. This would imply that the phase changes by exactly π over the SPR. However, the *imaginary* part of $\delta\epsilon$ results in a change in reflectance that is symmetric around the central wavelength of the SPR [78]. The combined contribution of $\delta\epsilon$ can result in an apparent total change less than π.

Near the IBT, the fundamental mode reaches its highest amplitude at 510 nm (2.43 eV), corresponding to a photon energy approximately equal to the IBT threshold energy of 2.4 eV. Interestingly, the strain-wave-induced changes are about 37 % smaller for wavelengths at and close to the IBT than for those near the largest SPR (at 649 nm). This is in remarkable contrast with the reflectance changes induced by the *electron dynamics* immediately following the pump pulse illumination. There,

the reflectance changes near the IBT are significantly larger than those near any of the SPRs.

The third- and fifth-order harmonic modes, at frequencies of 28.5 GHz and 47 GHz, respectively, have the largest amplitude reflectance changes at 510 nm. The amplitude at this probe wavelength, relative to the first-order mode, is much higher than near any of the SPRs.

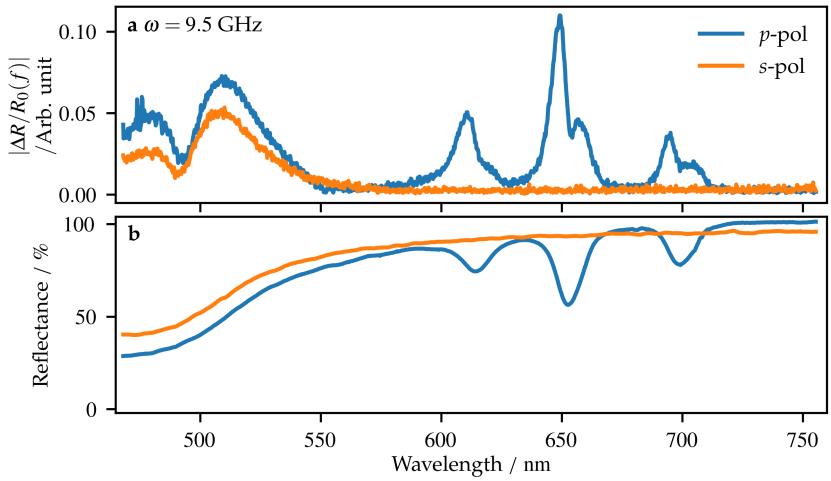

Figure 5.6: A. Amplitude of reflectance changes induced by the 9.5 GHz strain wave, for s- and p-polarized probe light. A moving average has been applied using 2 neighbouring values. B. The static reflectance, for s- and p-polarized light, as a function of wavelength, for an AOI of 26°, see also Section 5.D.

For s- and p-polarized probe light, we plot in Figure 5.6A the FFT amplitude of the reflectance changes at 9.5 GHz as a function of probe wavelength. The changes in reflectance for s-polarized light in the time domain are shown in Section 5.C. As mentioned before, significant reflection changes occur near the SPRs for p-polarized light and are, as expected, absent for s-polarized light. Around the IBT, strain-wave-induced reflectance changes are present for both polarizations.

In Figure 5.6B, we plot the static reflectance of the sample for s- and p-polarized light. The SPRs, visible as dips in the p-polarized reflectance spectrum, coincide with the regions of enhanced strain-wave-induced reflectance changes. Upon careful inspection, these changes peak at wavelengths that are actually on the slope of the dips. However, near the IBT, such sharp features are absent in the static reflectance spectra, yet large strain-wave-induced changes are measured there.

5.4 CONCLUSION

The results show that the shape of the static linear reflectance spectrum around SPRs and IBT is not a good predictor of the amplitude of the strain-wave-induced reflectance changes. Whereas the SPRs are sharp and the IBT manifests itself as a more gradual change in reflectance, the strain-wave-induced reflectance changes are only about 37 % smaller near the IBT, compared to the amplitude near the SPRs.

However, the temporal shape of the reflectance changes is significantly different when probing around the IBT compared to the SPRs. In absence of a model that can accurately predict these signals, the conclusion is that wavelength-dependent measurements are required to determine the maximum strain-wave-induced reflectance changes when resonances of a different nature are present.

5.A EXPERIMENTAL SETUP

The setup is shown schematically in Figure 5.7. The output of a Ti:sapphire amplified laser system (Astrella-USP, Coherent) with a central wavelength of 800 nm, pulse energy of 6.3 mJ, pulse duration of 35 fs, and a repetition rate of 1 kHz is split into two using a 85:15 (R:T) beam splitter. The transmitted part is used as pump and is frequency-doubled using a β-barium borate (BBO) crystal. Remaining 800 nm light is removed via several dichroic mirrors, high-reflective only for 400 nm. The pump laser wavelength of 400 nm was chosen as gold absorbs this wavelength much stronger than 800 nm, the fundamental laser wavelength. A computer-controlled delay line (M-521.D, Physik Instrumente) varies the arrival time of the pump pulses at the sample. A mechanical chopper, synchronized to the pulse train, blocks every other shot, reducing the repetition rate to 500 Hz. The pulses are weakly focussed onto the sample, incident at an angle of about 6° with respect to the surface normal of the sample. The spots are slightly elliptical, with full-width at half maximum (FWHM) axes of 380 μm and 300 μm. The pump pulse polarization is parallel to the grating lines of the sample, such that they cannot excite SPPs. The pump peak fluence is 6.2 mJ cm^{-2}, about 60 % is absorbed. When all the absorbed energy is converted into heat, the 172 nm Au layer will expand by 212 pm (or about 0.12 %).

The stronger, reflected part of the output of the laser pumps a three-stage optical parametric amplifier (OPA, TOPAS-HE, Light Conversion). The output wavelength of the OPA is set to 1200 nm. The pulse energy of the output is reduced to a few μJ, by reflecting the beam off several beam splitters. A GaAs wafer, used as a long-pass filter, removes any remaining visible light from the pulses and a half-wave plate controls the polarization of the pulses. The pulses are focussed by a 100 mm focal distance lens into a 2 mm thick BaF_2 crystal, creating a single filament. BaF_2 was chosen for its ability to also generate wavelengths in the blue region [43]. The crystal is moved in a plane perpendicular to the beam direction in Lissajous figures, to avoid the accumulation of damage at a single position inside the crystal and to slow the degradation of the WLC spectrum [44]. The WLC is collimated using a 75 mm achromatic lens. A wire-grid polarizer (WP25M-UB,Thorlabs) removes any unwanted polarization. The transmitted part of a beam splitter (BST-10, Thorlabs) is measured by the spectrometer as a reference. The reflected part is focussed onto the sample by an achromatic lens (focal distance 200 mm). The spot size has a FWHM diameter of 45 μm.

In the spectrometer, light diffracts off a blazed grating (GR25-0305, Thorlabs) with 300 lines per mm. The diffracted light is focussed onto the complementary metal-oxide-semiconductor (CMOS) sensor (Andor Zyla 4.2 Plus, Oxford Instruments) by a system of two cylindrical lenses. The light is focussed by the first lens ($f = 75$ mm) in the horizontal direction, where the wavelengths are dispersed due to the grating. The axis of curvature of the second lens ($f = 50$ mm) is rotated by 90° with respect

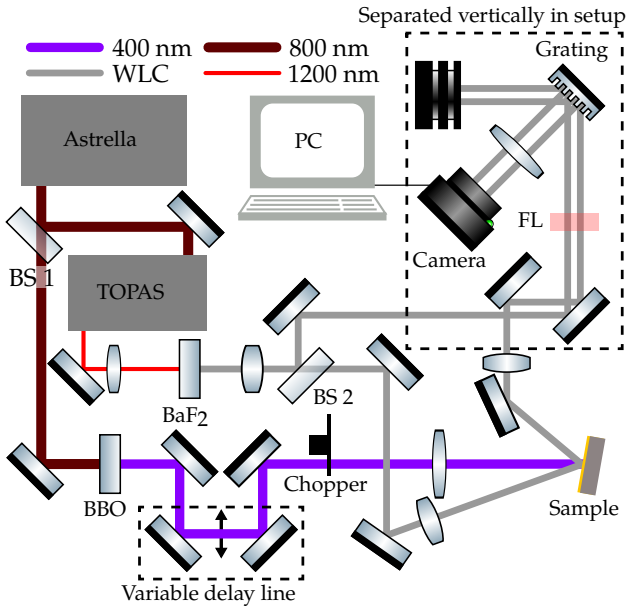

Figure 5.7: BS 1: 85:15 (R:T) 800 nm beam splitter, BS 2: broadband 70:30 (R:T) beam splitter, BaF_2 : barium fluoride, BBO : β-barium borate, FL: Long-pass filter (Thorlabs, FEL-450).

to the first. This lens focusses the light onto *several* pixels in the vertical direction, where the wavelengths are *not* dispersed. After each exposure, the camera sums the intensity counts of each column of these pixels and the results are sent to the computer afterwards. The two active area consists of 2048 columns of 30 pixels in height, so ultimately 2048 numbers are sent to the computer. This increases the total amount of light that can be measured and therefore increases the SNR of the measured spectra.

The spectrometer records spectra with 2048 pixels between 468 nm and 755 nm. The pump wavelength (400 nm) is outside this range and a long-pass (with a cut-off wavelength of 450 nm) filter (FEL-450, Thorlabs), placed before the diffraction grating, blocks any scattered pump light.

5.B DATA PROCESSING

The sample reflectance spectrum and the reference spectrum are measured for each probe pulse simultaneously, by using two vertically separated active areas on the camera sensor. We divide the reflection spectrum by the reference, to correct for any spectral fluctuations in the WLC. To minimize the pixel-to-pixel mismatch between the two spectra, we numerically shift one with respect to the other. The optimal shift is found by minimizing the mean square difference between the absorption spectra of a reference material (RM-DG, Starna) measured by the two spectrometer channels. This reference material is also used to calibrate the wavelength axis of the measurements. The relative change in reflectance is calculated from two

consecutive probe pulses, one after excitation of the sample with a pump pulse, the other without.

The measurements are taken in a 'slow-scanning' approach, where the spectra of 2000 probe shots are recorded at a position of the delay line. The delay line then proceeds to the next position. These 2000 recorded spectra result in 1000 spectra of relative changes in reflectance, which are then averaged. The range of delays is scanned twice–first in ascending order, and then in descending order. The presented relative changes in reflection are the average of the two scans.

Outlier WLC probe pulses, characterized by a spectrum with significantly more or less light than average, are excluded from the data set. To identify these outliers, the counts of all pixels in a single reference spectrum are summed. The mean and standard deviation of these summed counts are then calculated across all acquired reference spectra of that measurement (where all delays are scanned twice).

The outliers are discarded if the sum of counts of the reference spectrum deviates by more than five times the standard deviation of the mean. Since this can happen to either the probe pulse that measures the reflectance of the pumped sample or the unperturbed sample, both are excluded. The average reflectance change for that position is then calculated using the remaining spectra.

5.c s-polarized probe

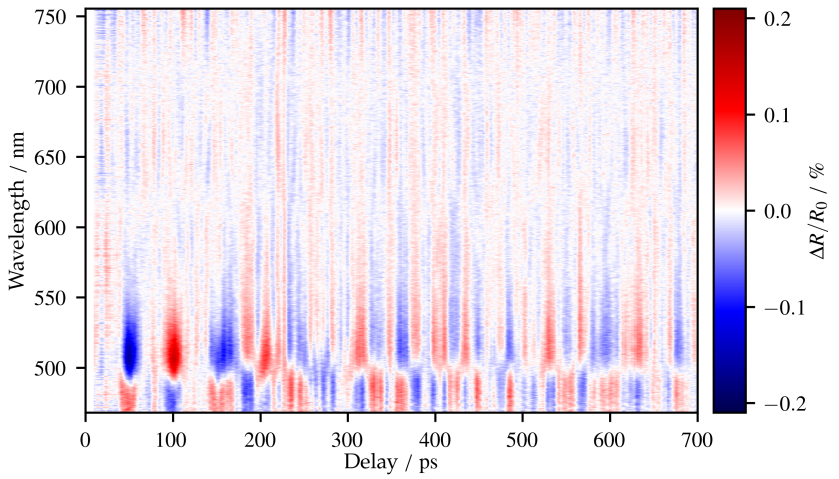

Figure 5.8: High-pass filtered reflectance changes for *s*-polarized probe light as function of pump-probe delay and wavelength. A 5 × 5 uniform filter has been applied.

Figure 5.8 shows the high-pass (cut-off frequency 6 GHz) filtered reflectance changes measured with *s*-polarized light. The pump fluence is equal to the other measurements, at 9.0 mJ cm^{-2}. As expected, no strain-wave-induced reflectance changes are observed near the wavelengths where, for *p*-polarized light, SPPs are excited. The LWs are measured only near the IBT, and only for the first 200 ps. We have identified two possible causes responsible for the absence of clear strain-wave-induced changes for delays larger than 200 ps. Firstly, the amplitude of the

strain-wave-induced relative reflectance changes is lower for *s*-polarized light, causing the signal at longer time delays to become indistinguishable from noise. Secondly, there is less reference light since the transmission of the used beam splitter (BST10, Thorlabs) is different for *s*- and *p*-polarization. Lower reference light affects the achievable SNR negatively. Nevertheless, in the first 200 ps, the temporal shape of the reflectance changes resembles that observed with *p*-polarized light.

5.D CALCULATION OF REFLECTANCE SPECTRUM

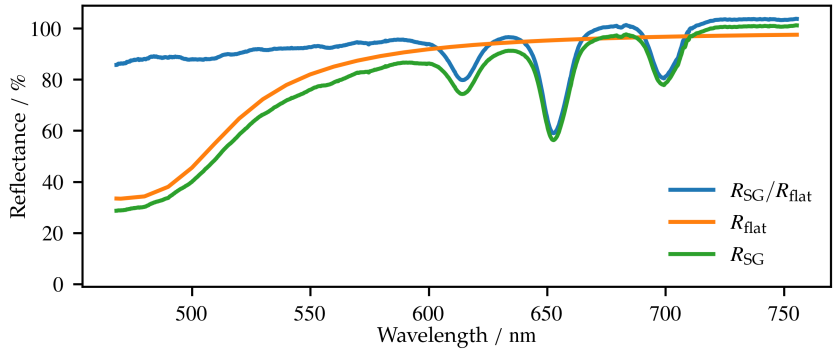

Figure 5.9: Plot of the calculated reflectance, at an angle of incidence of 26° with respect to the surface normal, for *p*-polarized light of the segmented grating (green), obtained by multiplying the measured ratio of reflectances of the segmented grating and a flat part of Au (blue) with the calculated reflectance of Au (orange).

The reflectance spectrum of the segmented grating, for *p*-polarized light, is shown in green in Figure 5.9. It was calculated by measuring the ratio of the reflectance of the Au-covered segmented grating and the reflectance of a flat part of the sample, also covered by the same layer of Au. This measurement was performed in the same setup as described earlier, but without any pump light. For wavelengths longer than 700 nm, the ratio is slightly larger than 100 %, most likely due to a small change in alignment from moving the sample vertically, such that a flat part of the sample could be exposed to the probe light. This ratio is shown in Figure 5.9 in blue. To find the true reflectance of the segmented grating, we multiplied the measured ratio with the calculated reflectance of Au. The reflectance of Au was calculated using the Fresnel equation for *p*-polarized light at an angle of incidence of 26° using n and k values from [89].

Figure 5.10 shows the same as Figure 5.9, but for *s*-polarized light. The ratio of reflectance of the segmented grating and the reflectance of a flat part were measured on a different, linear spectroscopy setup. This setup consists of a fibre-coupled halogen light source and a fibre-coupled spectrometer (AVASPEC-ULS2048CL-EVO, Avantes). For *s*-polarized light, the difference between the reflectance of the grating and the flat part comes from light diffracted off the grating.

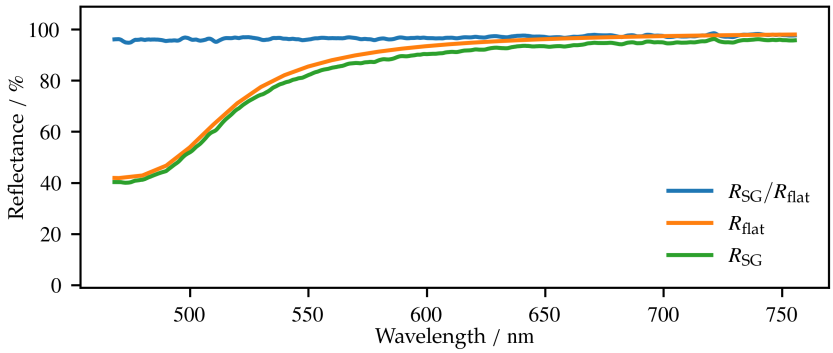

Figure 5.10: Plot of the calculated reflectance, at an angle of incidence of 26° with respect to the surface normal, for *s*-polarized light of the segmented grating (green), obtained by multiplying the measured ratio of reflectances of the segmented grating and a flat part of Au (blue) with the calculated reflectance of Au (orange).

6

BROADBAND OPTICAL DETECTION OF STRAIN WAVES IN A THIN RUTHENIUM FILM

ABSTRACT

Optical detection of ultrafast strain waves is difficult, as the wavelength-dependent optical response to these waves is not known for many materials. Here, we investigate the strain-wave-induced changes in reflectance of a 30 nm ruthenium layer for wavelengths between 475 nm and 1000 nm using an ultrafast spectrometer. For wavelengths shorter than 900 nm, a train of individual strain-wave-induced changes in reflectance is observed. These changes become shorter and sharper in time, as the probe wavelength decreases. Consequently, the peak of the spectrum of the reflectance change induced by the first strain-wave reflection shifts to higher frequencies for shorter probe wavelengths. We find that the maximum detectable strain-wave frequency is inversely proportional to the optical penetration depth of the probe wavelength. Surprisingly, gaps are measured for some strain-wave frequencies at specific probe wavelengths, even though these frequencies are below the maximum detectable frequency.

A manuscript based on this chapter is in preparation.

6.1 INTRODUCTION

RUTHENIUM (Ru) is a relatively new material in the semiconductor industry. It is a candidate to replace copper as a material for interconnects, the 'wires' connecting transistors and different layers in semiconductor chips. Copper suffers from 'graininess', as these interconnects become more narrow ($< 20\,\text{nm}$), which increases resistivity [90]. Ruthenium suffers less from this problem and has, for these narrow wires, a lower resistivity than copper [19, 91]. Furthermore, ruthenium may be used as a selective etch masks (hard mask) in semiconductor device manufacturing, to protect areas from being etched [92–94].

In both cases, a relatively thick ($> 50\,\text{nm}$) layer of ruthenium may be deposited onto the wafer on which semiconductor devices are fabricated, covering the wafer completely. Unfortunately, such ruthenium layers are opaque for most wavelengths. This can make optical metrology, especially alignment metrology, of these wafers challenging.

In alignment metrology, the position of the wafer is determined using several 'alignment markers', just before exposure in a photolithography machine. The position of these markers is determined with sub-nanometre accuracy via the diffraction of (visible) light [4].

It has been shown that such gratings, buried underneath opaque layers, can be optically detected with the help of ultrafast laser-induced strain waves [15, 16]. One of the main challenges here is the optical detection of the strain waves with a sufficiently high signal-to-noise ratio (SNR) in a limited amount of time. In general, increasing the SNR can be done by either decreasing noise or increasing signal. One method to increase the SNR in the optical detection of strain waves, is to probe with wavelengths close to optical resonances. These resonances, such as surface plasmon polariton resonances (SPRs) [17, 47, 78] or etalons [95], can increase the change in reflectance induced by the strain wave, when it is close to the surface of the opaque layer.

Improving the optical response to strain waves starts with selecting the 'proper' probe wavelength, where the change in reflectance, induced by the strain wave, is largest. Although there is some research on the behaviour of ruthenium under femtosecond illumination [96–100], there is no study of the broadband optical response of ruthenium to ultrafast strain waves. The best way to determine the proper probe wavelength is through experiments, as the linear optical reflection spectrum is not a good predictor for the strength of the strain-wave-induced change in reflectance [18].

Here, we present a study of the strain-wave-induced changes in reflectance, as a function of probe wavelength and pump-probe delay time, of an approximately 30 nm thick ruthenium layer on sapphire, for two wavelength ranges, namely from 475 nm to 760 nm and from 730 nm to 1000 nm. We find that the strain-wave-induced reflectance changes show a strong dependence on the optical probe wavelength. Not only the amplitude but also the temporal shape of the induced changes varies with probe wavelength. For probe wavelengths shorter than 900 nm, we observe a train of strain-wave-induced changes in reflectance, spaced 10 ps apart, while for the longer probe wavelengths, the change more or less resembles a damped sinus. The changes in reflectance become shorter and sharper in time, for shorter probe wavelengths. This is also reflected in the spectrum of

the in reflectance induced by the first reflection of the strain wave, which contains higher frequencies when measured at shorter probe wavelengths. We find that the maximum detectable frequency, as a function of probe wavelength, more or less corresponds to the time it takes for the strain wave to propagate over a distance that corresponds to the optical penetration depth. Lastly, we find that the spectrum contains some gaps, most notably at a probe wavelength of 600 nm, where the frequencies below 150 GHz are only very weakly present.

6.2 METHODS

An amplified laser system (Astrella, Coherent) generates a 1 kHz pulse train consisting of 35 fs, 6 mJ pulses with a central wavelength of 800 nm. This pulse train is split into two beams by an 85 : 15 (R:T) beam splitter.

The weaker part is frequency-doubled by a β-barium borate (BBO) crystal, such that its central wavelength is 400 nm, and is used to pump the sample. Every other pulse is blocked by an optical chopper, synchronized to the pulse train, such that the repetition rate is reduced to 500 Hz. A mechanical delay line (M-521.D, Physik Instrumente) varies the optical path length of the pump pulse. The pump pulse polarization is vertical with respect to the laser table and is weakly focussed onto the sample. The full-width at half maximum (FWHM) axes of the elliptic spot are 400 μm and 500 μm. The pump peak fluence is 9.4 mJ cm^{-2}.

The stronger part, reflected by the beam splitter, pumps a three-stage optical parametric amplifier (OPA) (TOPAS-HE, Light-Conversion). About 1 μJ to 2 μJ of the OPA's signal pulse, tuned to 1200 nm, is used to generate a white light continuum (WLC) in either a barium fluoride (BaF_2) or a sapphire crystal. Barium fluoride is used for wavelengths between 470 nm and 760 nm [43]. For the longer-wavelength measurements, a sapphire crystal was used to generate the WLC probe pulse. For this wavelength range, using sapphire results in less pulse-to-pulse fluctuations in spectrum and intensity, compared to BaF_2. After the generation crystal, the WLC pulse is collimated and focussed onto the sample, with an angle of incidence of about 25° with respect to the surface normal. The pulse is horizontally polarized, i.e., in the plane formed by the surface normal of the sample and the propagation direction of the probe pulse. The FWHM spot size of the probe pulse on the sample is approximately circular with a diameter of about 45 μm.

After the sample, the reflected probe pulse is collimated and measured by the spectrometer. The spectrometer consists of a grating with 300 lines per mm and a lens system, comprising two cylindrical lenses, with an effective focal distance of 75 mm that focusses the dispersed pulse onto a camera (Andor Zyla 4.2 Plus, Oxford Instruments). A reference measurement of the WLC is recorded by the same spectrometer, but at a different active area on the camera. For this, part of the WLC pulse is split off using a beam splitter, before it probes the sample. More details can be found elsewhere [18].

When the crystal that is used to generate the WLC is changed, the spectrometer grating is rotated to ensure that the wavelength range of interest is captured by the camera. Also, the beam splitter that splits the reference from the probe beam is swapped and the spectrometer is calibrated again. Table 6.1 lists the wavelength ranges and the configurations that are used.

Table 6.1: Configuration of the experimental setup for the different wavelength ranges.

Wavelength range	WLC crystal (thickness)	Beam splitter (R:T)
470 nm to 760 nm	BaF_2 (2 mm)	Thorlabs BST10 (70:30)
730 nm to 1000 nm	Sapphire (5 mm)	Thorlabs UFBS8020 (80:20)

The ruthenium film was deposited onto a sapphire substrate, via magnetron sputtering at an argon plasma pressure of 2×10^{-3} mbar, with a rate of approximately $0.25\,\mathrm{nm\,s^{-1}}$. The substrate was chemically cleaned using a solution of ammonium hydroxide (NH_4OH) and hydrogen peroxide in water and, subsequently, rinsed in isopropanol and dried using N_2 gas.

6.3 RESULTS

Ruthenium has a strong electron-phonon coupling constant [101, 102], which means that the most of the pump pulse energy, initially absorbed by the free electron gas, is transferred to the lattice within the first picosecond after illumination with the pump pulse. We present and briefly discuss the pump-induced changes in reflectance during the first few picoseconds after illumination in Section 6.A. The rapid transfer of energy to the lattice results in (i) limited initial energy diffusion deeper into the layer, as most of the energy is deposited close to the surface as a result from the short penetration depth of the pump light, and (ii) the generation of very-high-frequency strain waves at the surface and back interface of the layer. The amplitude of the strain wave generated at the surface is much larger than that of the strain wave generated at the back surface due to the short penetration depth of the 400 nm pump wavelength and the limited energy diffusion of the electron gas during the first picoseconds.

In Figure 6.1, we show the measured relative changes in reflectance, averaged over a 2.1 nm wide band, as a function of pump-probe delay, at probe wavelengths of 500 nm, 700 nm, and 900 nm. The measurements are shifted in time such that the onset of the initial changes is at 0 ps. The reflectance for 700 nm and 900 nm increases abruptly at 0 ps pump-probe delay time, while the reflectance at 500 nm abruptly decreases and also recovers immediately. These changes are mostly related to the electron dynamics and are discussed in Section 6.A. After the rapid increase, the reflectance at 700 nm and 900 nm decays exponentially, on a timescale of about 40 ps, from values of about 2 % and 4.2 %, to 1.2 % and 3 %, respectively. This is the result of the redistribution of energy *within* the ruthenium layer, via electron gas diffusion, from near the surface, where most of the energy is initially deposited, deeper into the layer. The reflectance at 500 nm is, however, mostly constant in time, at a level slightly lower than its static reflectance. Furthermore, the exponential decay is absent.

At 11 ps, all three wavelengths show a rapid change in reflectance. For 900 nm, the change is a decrease in reflectance lasting a few picoseconds, superimposed on the exponential decay. For 700 nm, the change is bipolar: first a decrease in reflectance, followed by an increase, relative to the exponential decay. At 500 nm, the change consists of two small increases in the reflectance, with a dip in the middle. These

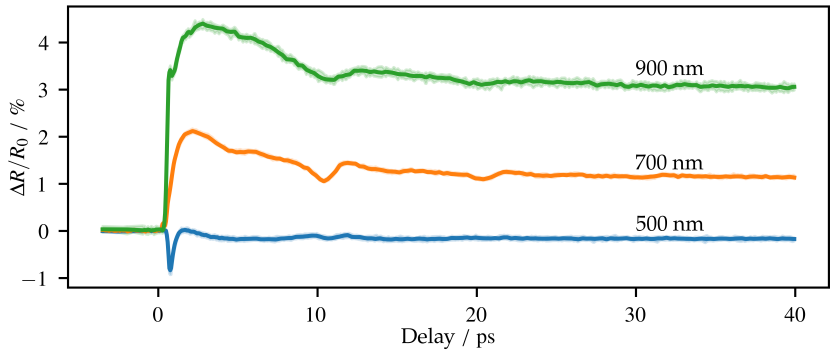

Figure 6.1: Changes in reflectance of a 30 nm ruthenium film as a function of delay with a 400 nm pump pulse, for three probe wavelengths of 500 nm, 700 nm, and 900 nm.

rapid changes are induced by a strain wave, generated by the thermal expansion of the hot lattice, returning to the surface, where it was generated, after being (partially) reflected at the back interface of the ruthenium layer and the sapphire substrate.

A similar rapid change in reflectance is visible at 21 ps for probe wavelengths of 700 nm and 900 nm. These changes are again caused by the strain wave as it has completed its second round trip. The amplitude of the changes is smaller, as the strain wave is, again, only partially reflected at the back interface. From the roundtrip time of 10.0 ps and the speed of sound of ruthenium of 5970 m s^{-1} [29], we calculate a layer thickness of 29.9 nm, close to the value of the intended 30 nm thickness.

To investigate the probe-wavelength-dependence of the strain-wave-induced changes in reflectance, we remove the thermal background by fitting an exponential decay to the change in reflectance for every measured probe wavelength. In Figure 6.2a and b, we plot the strain-wave-induced changes in reflectance as a function of time, on the horizontal axis, and as a function of probe wavelength, on the vertical axis, obtained from the long-wavelength measurement (a) and short-wavelength measurement (b). A decrease in reflectance is indicated by the colour blue, white indicates little or no change and red indicates an increase in reflectance. The amplitudes shown in panel a (and c) are multiplied by a factor of 1.36 to account for an apparent difference in pump fluence, see Section 6.C for more information.

In Figure 6.2a and b, we again observe the first reflection of the strain wave at around 11 ps. For a probe wavelength of 1000 nm, the strain wave induces a decrease in reflectance, lasting about 4 ps, centred at 11 ps. The duration of this decrease in reflectance gradually becomes shorter for shorter probe wavelengths. At 760 nm, the shortest wavelength shown in panel a, the strain-wave-induced decrease in reflectance only lasts about 2 ps. For the shorter probe wavelengths shown in panel b, this trend continues: the induced change in reflectance becomes sharper and shorter for shorter wavelengths. In addition to this, the strain-wave-induced change in reflectance becomes gradually asymmetric for probe wavelengths shorter than 860 nm. The reflectance change is almost bipolar between 750 nm and 620 nm. For

probe wavelengths short than 620 nm, an increase in reflectance is observed before the rapid decrease centred at 11 ps. Furthermore, the amplitude of this change at 11 ps also decreases for shorter probe wavelengths. At 500 nm, the change in reflectance only consists of two positive shoulders, at about 9.5 ps and 12 ps, this can be seen best in Figure 6.1.

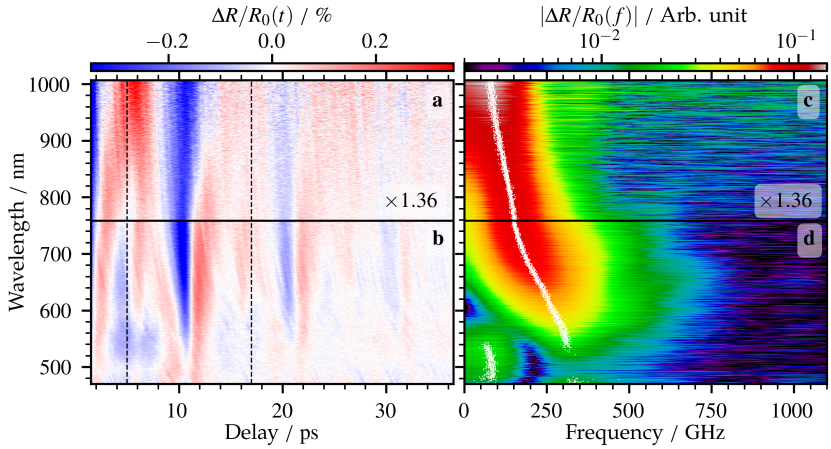

Figure 6.2: a and b: Measured strain-wave-induced changes in reflectance of a 30 nm thick layer of ruthenium on sapphire, after removing the thermal background. c and d: FFT amplitudes of a time interval around the first strain-wave-induced change in reflectance, at 11 ps, shown in a and b. This interval, from 5 ps to 17 ps, is indicated by the vertical black dashed lines in a and b. The white dots indicate the frequency with the highest amplitude for every wavelength. The amplitudes in a and c are multiplied by a factor of 1.36, see Section 6.C.

We use a fast Fourier transform (FFT) algorithm to calculate the Fourier transform of the time-dependent change in reflectance in an interval centred at 11 ps, the middle of the strain-wave-induced change in reflectance, for all probe wavelengths. This interval starts at 5 ps and ends at 17 ps, is shown with two dashed vertical lines in Figure 6.2. A Hann window is used to reduce windowing effects in the Fourier transform.

Figure 6.2c and d show the amplitude of the Fourier transform as a function of frequency on the horizontal axis, and of probe wavelength on the vertical axis. The amplitude is shown in a logarithmic colour scale, shown above the plot. The frequency with the highest amplitude is indicated with a white dot, for every probe wavelength. At a probe wavelength of 1000 nm, the spectrum of the strain-wave-induced change in reflectance peaks at approximately 80 GHz and extends to 400 GHz. As the probe wavelength decreases, the peak of the spectrum shifts to higher frequencies. At 760 nm, at the intersection between the two sets of measurements, the calculated spectrum peaks at 150 GHz. Between 590 nm and 700 nm, the highest frequencies contained in the high-frequency tail even approach 800 GHz. It is important to note that these changes are correlated with the probe wavelength, as the same strain wave is probed by every wavelength.

The *peak* of the spectrum reaches its highest frequency of 300 GHz around 560 nm. However, the maximum spectral amplitude starts decreasing for probe wavelengths

shorter than 650 nm, corresponding to smaller strain-wave-induced changes in reflectance. Surprisingly, there are several gaps in the strain-wave spectrum for these shorter wavelengths. The first gap is at the lowest frequencies, below 150 GHz, for probe wavelengths between 590 nm and 620 nm. The second gap is present at 200 GHz, for wavelengths shorter than 540 nm. This shows that there is not a simple relation between optical probe wavelength and the magnitude of the strain-wave-induced changes in reflectance.

Finally, we note that the noise floor at the longer probe wavelengths, especially in panel c of Figure 6.2, is higher than for the shorter wavelengths. This is mainly due to the low quantum efficiency of the silicon complementary metal-oxide-semiconductor (CMOS) camera used in the spectrometer, which results in a lower SNR for the longer wavelengths.

The Fourier transform of the full time interval is shown in Section 6.B. It contains the same frequencies, but the spectrum is now modulated at 100 GHz, due to the second and third reflections of the strain wave that arrive at 10 ps intervals.

6.4 DISCUSSION

The maximum optically detectable strain-wave frequency is, according to [103], given by either the Brillouin frequency or by a frequency inversely proportional to the penetration depth of the probe wavelength. We will first discuss the Brillouin oscillation and frequency.

We assume an infinitely short, plane, strain wave is propagating in a transparent, isotropic material, with a (real) refractive index n. A probe pulse, with wavelength λ_0, is (at normal incidence) incident on the strain wave and is partially reflected. The reflected field is constant, if the strain wave does not change while it propagates. A detector, only sensitive to the intensity of the reflected probe pulse, then measures a signal constant in time. However, typically we measure a strain wave in a *layer*, where the surface also reflects part of the light. The probe reflection from the surface interferes with the probe reflection from the strain wave and changes the measured intensity. Since the strain wave moves at the speed of sound, v_s, in the material, the path length of the probe's reflection off the strain wave changes too, with twice the speed of sound, as the probe has to travel to and from the strain wave. When the path length difference equals one wavelength in the material, λ_0/n, the phase of the probe's reflection is the same, and the reflections constructively interfere. The time it takes for the intensity to complete one period of oscillation, the Brillouin oscillation period, is then given by $t_B = \lambda_0/(2nv_s)$. This also implies that the Brillouin oscillation frequency, $f_B = 2nv_s/\lambda_D$, is the *only* frequency that is measured, and is independent of the shape of the strain wave.

Now, consider a material that strongly absorbs, and in which light has a finite penetration depth. In this case, we can only measure the strain wave if it is inside the optical penetration depth at the probe wavelength, δ_p in the material. Furthermore, the distance of the strain wave to the surface not only influences the phase of the field reflected from the strain wave, but also the *amplitude* of this field. Again, we consider an infinitely short strain wave. Assuming a relatively long penetration depth, this very-high-frequency strain wave will result in a change in reflectance that is 'smeared' out in time. In contrast, a probe pulse with a short penetration depth only measures the strain wave if it is very close to the surface, resulting in a

short time when the reflectance is affected by the strain wave. So, the time it takes for the infinitely short strain wave to propagate through this volume determines the maximum frequency with which we can detect the strain wave. This frequency is then given by $f_p = v_s/\delta_p$.

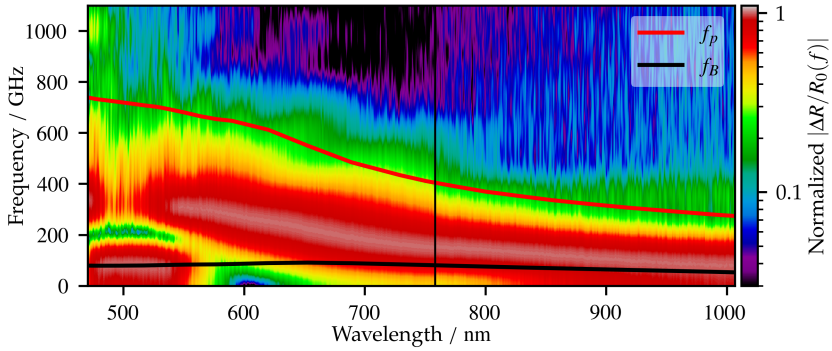

Figure 6.3: Strain-wave amplitude, normalized to the maximum amplitude for every wavelength, as a function of frequency (vertical) and wavelength (horizontal). The spectra are smoothed in the horizontal direction by a moving average over 10 spectra. The Brillouin frequency, f_B, (black line) and the frequency associated with the penetration depth, f_p, (red line) are calculated using the refractive index of ruthenium taken from [23].

In Figure 6.3, we plot the amplitude of the Fourier transform of the first strain-wave-induced change reflectance as a function of probe wavelength and frequency, similar to Figure 6.2 c and d, but mirrored and rotated. For each optical probe wavelength, we have normalized the spectrum to the maximum amplitude of that probe wavelength. As a result, we can more easily compare the differences in the strain-wave spectra measured at different probe wavelengths. The spectra are smoothed by applying a moving average over 10 spectra in the horizontal direction. On top of these spectra, the Brillouin frequency, f_B, and the frequency associated with the penetration depth, f_p are plotted as a function of probe wavelength, in black and red, respectively. These are calculated using the complex refractive index, $\tilde{n}$, given by [23] and the speed of sound, $v_s = 5970\,\mathrm{m\,s^{-1}}$, taken from [29]. As can be seen, the frequency associated with the penetration depth more or less follows the envelope of the measured strain-wave frequencies, showing that the optical penetration depth is what limits the highest detectable strain-wave frequency.

We would like to point out that the largest strain-wave-induced changes in reflectance are *not* necessarily measured at the shortest probe wavelengths. For example, in Figure 6.2d, it seems that the highest frequencies are observed between 600 nm and 700 nm, but this mainly caused by the larger amplitude of the strain-wave-induced at those wavelengths, compared to the shortest wavelengths. Both f_B and f_p are calculated without knowledge of the (probe-wavelength dependent) 'strain-optic' coefficient, $\partial\tilde{n}/\partial\eta$, where η is the strain.

Independent of that, it sometimes may be beneficial to probe (a bit) deeper into the material. Consider the stress in the material, in the direction perpendicular to the surface, [100]:

$$\sigma_z = \sigma_{\text{str}} - \sigma_{\text{thermal}}, \tag{6.1}$$

$$\sigma_{\text{str}} = (\lambda + 2\mu)\eta_z, \tag{6.2}$$

where σ_{str} is the stress associated with the strain, σ_{thermal} the thermal stress, λ the Lamé's first parameter, μ the shear modulus, and η the strain. At a free surface, the stress σ_z must be zero [12], in that case, the stress induced from strain equals the thermal stress. Moreover, the thermal stress only varies slowly in time, meaning that the amplitude of the strain wave is zero at the surface. This results also in an almost perfect reflection of the strain wave at a free surface. So, it may be beneficial to probe with wavelengths that penetrate a bit deeper into the material, or to change the free surface to an interface, with different boundary conditions [104], though this may result in a lower maximum strain-wave frequency that can be detected.

Finally, there are some gaps in the spectrum, which are visible in Figure 6.3 at, for example, the low frequencies, for probe wavelengths around 600 nm, or at the frequencies around 200 GHz for probe wavelengths between 480 nm and 550 nm. Furthermore, we find that the vanishing of the amplitude of the low strain-wave frequencies around a probe wavelength of 600 nm is accompanied by a phase shift of the low-frequency components, when comparing the phase of these frequencies for probe wavelengths above and below 600 nm.

We plot the high-pass and low-pass filtered changes in reflectance as function of time (horizontal) and probe wavelength (vertical), for the short-wavelength set of measurements, in Figure 6.4 a and b, respectively. The changes are shown in a linear colour scale shown next to panels a and b. An 8^{th}-order, zero-phase, digital filter is used, with cut-on and cut-off frequencies of 150 GHz, which is in the gap between the first and second peak of the spectrum, as seen in Figure 6.8. In panel a, the high-pass filtered changes are becoming sharper for the shorter probe wavelengths, since higher strain-wave frequencies are detected. However, in panel b, the phase of the (slow) oscillation changes at a probe wavelength around 600 nm. This is indicated by black dashed lines, which follow the peaks and valleys of the low-frequency oscillatory change in reflectance.

We speculate that both the vanishing amplitude at and the change in phase for certain strain-wave frequencies may be related to what is described in [76]. In that article, the authors describe the relation between the measured strain-wave-induced changes in reflectance as a function of strain-wave frequency and the frequency components of the strain wave with a frequency-dependent transfer function. This transfer function depends on the wave number of the optical probe, wave number of the strain wave in the medium, the dielectric function of the medium and its derivative with respect to strain. In their description, the transfer function, for all strain-wave frequencies, is always a purely imaginary number. So, for a fixed probe wavelength, the transfer function, for increasing strain-wave frequency, may cross zero and continue on the other side of the imaginary axis. This would result in a π-phase shift for the higher frequencies, for which the transfer function amplitude is larger than zero. Conversely, the same may happen when the probe wavelength is varied, for a fixed strain-wave frequency.

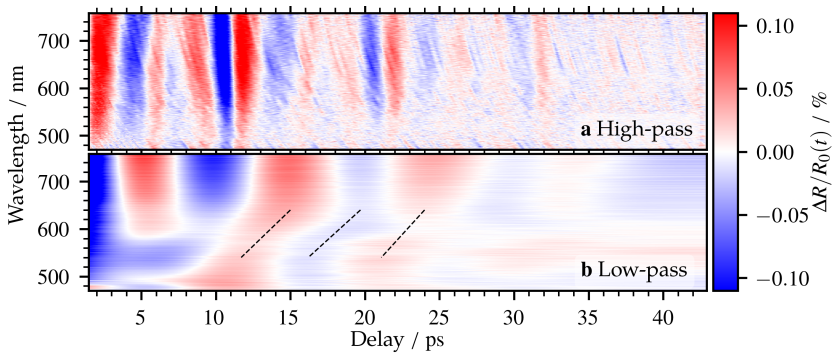

Figure 6.4: a. High-pass filtered (cut-on frequency: 150 GHz) strain-wave-induced changes in reflectance for the short-wavelength set of measurements. b. Low-pass filtered (cut-off frequency: 150 GHz) strain-wave-induced changes. The black dashed lines show the change in the phase of the low-frequency oscillations around 600 nm.

6.5 CONCLUSIONS

We have measured the ultrafast strain-wave-induced changes in reflectance of a 30 nm ruthenium layer on a sapphire substrate, as a function pump-probe delay time and probe wavelength. Two sets of measurements were conducted, one for wavelengths between 480 nm and 760 nm, the other for wavelengths between 730 nm and 1000 nm. For all probe wavelengths, we detect strain-wave-induced changes in reflectance, with a period of 10 ps. The strain-wave-induced changes are slow oscillations with a 10 ps period for the wavelengths around 1000 nm. But for wavelengths shorter than 900 nm, a train of isolated strain-wave-induced changes in reflectance is measured, spaced 10 ps apart. These individual pulses contain frequencies up to 800 GHz, for wavelengths around than 650 nm. However, the amplitude of the changes in reflectance decreases for wavelengths shorter than 600 nm. Furthermore, we find that the maximum detectable frequency, as function of probe wavelength, corresponds to the time it takes for the strain wave to propagate through the optical penetration depth at that probe wavelength. Finally, we observe some frequency components that have a very low amplitude. Most notably, almost no strain-wave-induced change in reflectance is measured for strain-wave frequencies below 150 GHz for probe wavelengths around 600 nm. This absence of signal is accompanied by a phase shift, when we compare the low-frequency changes in the reflectance at probe wavelengths above and below the probe wavelength of 600 nm.

6.A ELECTRON DYNAMICS

Ultrafast strain waves are generated by the rapid expansion of the ruthenium layer due to heating of the metal lattice after illumination with the pump pulse. The pump pulse energy is initially absorbed by the free electron gas and is transferred to the lattice via electron-phonon coupling. In this section, we probe the reflectance during the first few picoseconds after illumination, where the electron dynamics are expected to be strongest.

We plot the pump-induced changes in reflectance as a function of pump-probe delay, for four probe wavelengths, 480 nm, 580 nm, 650 nm, and 730 nm, in Figure 6.5a. The measured changes in reflectance are shifted in time such that the onset of the changes is approximately the same, i.e., the chirp in the white light probe pulse has been corrected afterwards.

The reflectance of the shortest probe wavelength shown, 480 nm, initially decreases and reaches a minimum of about 0.2 % lower than its static reflectance at about 200 fs. After that, the change in reflectance becomes positive and reaches a constant value of 0.1 % at 500 fs. At 580 nm, the change in reflectance also reaches a minimum at 200 fs, at −0.7 %. It recovers slightly, but the change remains negative at about −0.4 % after the minimum. At 650 nm, the reflectance shown a similar change as at 480 nm, although the change in reflectance is about 0.5 % after 1 ps. The change in reflectance at 730 nm is strictly positive. However, at 200 fs, the change shows a 'wobble', before increasing to its maximum value of 1.2 % at 1 ps.

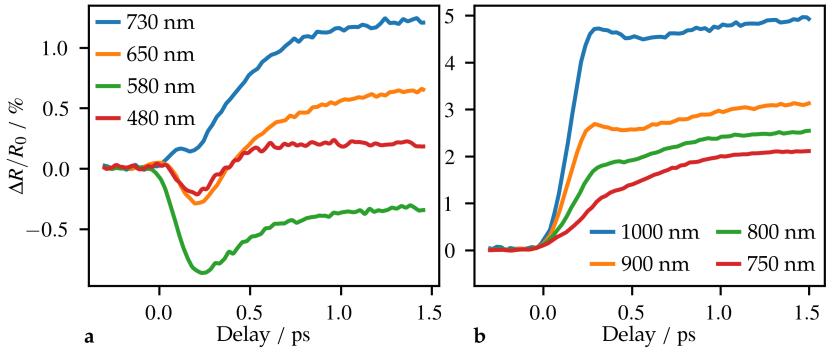

Figure 6.5: a. Measured changes in reflection of the 30 nm ruthenium layer as a function of pump-probe delay, for probe wavelengths of 730 nm, 650 nm, 580 nm, and 480 nm. b. Same for probe wavelengths of 100 nm, 900 nm, 800 nm, and 750 nm, which were obtained in a separate measurement.

In Figure 6.5b, the changes in reflectance as a function of pump-probe delay, of four longer probe wavelengths, of 750 nm, 800 nm, 900 nm, and 1000 nm, are plotted. The reflectance at 750 nm increases gradually, until it reaches a level about 2 % higher than the static reflectance. The reflectance for the longest wavelengths, 800 nm, 900 nm, and 1000 nm increases more abruptly and almost like a step-function when the ruthenium is illuminated by the pump pulse. The reflectance reaches a constant level of 2.2 %, 2.8 %, and 4.7 % for wavelengths of 800 nm, 900 nm, and 1000 nm, respectively.

The wavelengths, shown in Figure 6.5a, have been selected as they are representative of four regimes observed in the full measurement, which is shown in Figure 6.6a. Here, the changes in reflectance, as a function of pump-probe delay (horizontal axis) and probe wavelength (vertical axis), are shown in colour. Red indicates an increase in reflectance, blue a decrease in reflectance and white indicates little or no change. Also, the chirp of the WLC pulse has been corrected by fitting a fifth-order polynomial to the onset of the change for each probe wavelength. This onset is defined as the first point to cross the threshold of 5 % of the maximum amplitude of the change in reflectance for that probe wavelength. The first regime,

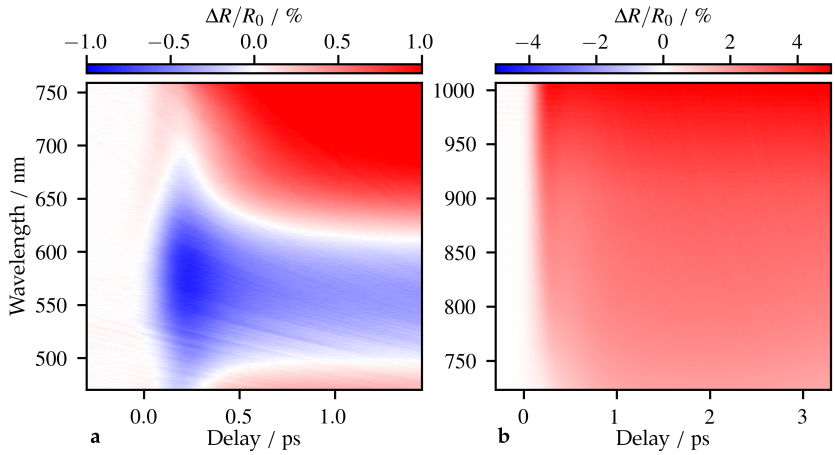

Figure 6.6: Changes in reflectance as a function of probe wavelength and pump-probe delay time, where the chirp is removed. Panel a shows the short-wavelength measurement, panel b the long-wavelength measurement.

represented by 480 nm, contains the shortest probe wavelengths up to 490 nm and shows, initially, a decrease in reflectance. After the initial decrease, the reflectance for these wavelengths recovers to a slight increase. The second regime contains wavelengths between 490 nm and 630 nm, which show a strictly negative change in reflectance. The third regime contains wavelengths between 630 nm and 690 nm that show a similar change in reflectance as the first regime, initially negative but later positive. The change in reflectance of wavelengths longer than 690 nm, in the fourth regime, is only positive. Also, the longer wavelengths shown in Figure 6.6b belong to this regime.

The evolution of the temperature in metals, shortly after illumination by an intense fs pulse, is often described by the two-temperature model (TTM) [24]. In this model, the free electron gas and the metal crystal lattice are treated as separate but coupled thermodynamic systems, each with its own temperature, T_e and T_l, respectively. The laser energy is absorbed by the electron gas and transferred to the lattice via electron-phonon scattering. The TTM, in one dimension, can be written as a function of two coupled heat equations as [24]:

$$C_e(T_e)\frac{\partial T_e}{\partial t} = \frac{\partial}{\partial z}\left(\kappa_e(T_e, T_l)\frac{\partial T_e}{\partial z}\right) - G\,(T_e - T_l) + S(z,t), \tag{6.3}$$

$$C_l\frac{\partial T_l}{\partial t} = G\,(T_e - T_l)\,. \tag{6.4}$$

Here, C_e and C_l are the heat capacities of the electron gas and lattice, respectively, κ_e is the electron thermal conductivity, G is the electron-phonon coupling constant and $S(z,t)$ is the absorbed laser energy density.

This system is solved numerically, using a forward difference method. The layer is treated as free standing and Neumann boundary conditions (no heat flux through the boundaries) are used. The electron heat capacity as a function of electron gas temperature and the electron thermal conductivity as function of electron gas and lattice temperatures are taken from [102]. The electron-phonon coupling constant

$G = 1.85 \times 10^{18}\,\mathrm{W\,m^{-3}\,K^{-1}}$ is taken from [26]. By multiplying the absorption profile as a function of depth with a Gaussian intensity distribution in time, the absorbed pump laser energy is calculated. The absorption profile is calculated with the transfer-matrix method (TMM) python package [22] for a 30 nm ruthenium thin film on a sapphire substrate. The n, k values of Ru are obtained via ellipsometry of a Ru layer deposited using the same process as is used here. The Gaussian intensity distribution has a FWHM pulse length of 60 fs, peaks at 250 fs, and has a (peak) fluence of 9.4 mJ cm^{-2}, matching the experimental parameters.

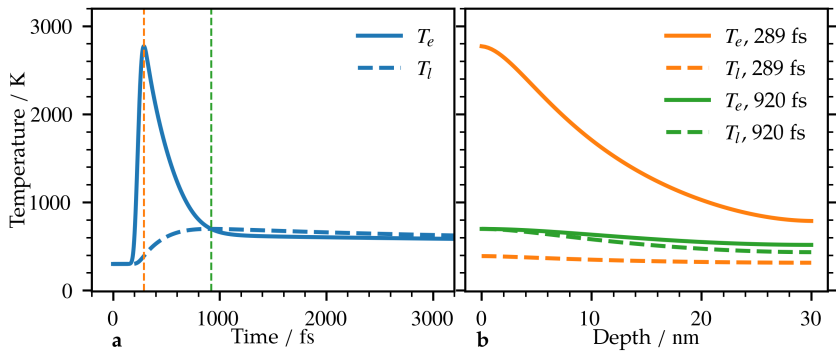

Figure 6.7: a. Calculated electron (solid lines) and lattice (dashed lines) temperatures as function of time at the surface and, b. as a function of depth for $t = 289$ fs and $t = 920$ fs. The vertical dashed lines in a. indicate the peak of the electron temperature at $t = 289$ fs (orange dashed line) and the moment the lattice and electron gas are in thermal equilibrium at the surface, at $t = 920$ fs (green dashed line).

Figure 6.7a shows the calculated electron gas and lattice temperature at the surface of the Ru layer, as a function of time. The electron temperature at the surface peaks at 289 fs, only 40 fs after the peak of the laser pulse, at 2770 K. After this, the electron temperature decreases rapidly as energy is transferred to the lattice, as the electron-phonon coupling in Ru is very strong. As a result, the lattice temperature increases by almost 400 K in the 500 fs after the peak of the laser pulse. At the surface, the lattice and electron gas are in *local* thermal equilibrium after 920 fs, at a temperature of 630 K. The deposited energy is still mainly concentrated near the surface, where most of the pulse energy is absorbed. From this moment on, the energy will be distributed evenly throughout the layer, by the electron gas, as the lattice does not conduct heat in this formulation of the TTM (see Equation Equation 6.4). As a result, the electron gas temperature is higher than the lattice temperature, near the back interface of the layer, while it is lower than the lattice temperature near the surface of the layer. This can be seen in Figure 6.7b, where the electron gas and lattice temperatures as a function of depth are plotted, at 289 fs and 920 fs. At the surface, the electron gas and lattice temperatures are in equilibrium, but deeper in the layer the electron temperature is still higher.

When comparing the electron and lattice temperatures at the surface, shown in Figure 6.7, with the measured changes in reflectance, shown in Figure 6.5, it is remarkable that, for wavelengths longer than ~ 700 nm, the drastic increase in electron temperature is not reflected in the change in reflectance. For the shorter wavelengths, this typical 'electron' peak in the reflectance appears to be present. This

appears to be in agreement with results from XUV Optics group at the University of Twente [96].

Finally, the lattice temperature distribution within the layer, as a function of time, also determines how the strain waves are generated. As soon as the lattice temperature starts to increase, the lattice starts to expand. Only the surface and the interface with the substrate are free to move, hence that is where strain waves will be generated. The lattice temperature from the surface increases from its initial temperature (300 K) to almost 700 K in about 500 fs. The surface will thus rapidly start to expand and generates a high-frequency strain wave. The back interface, in the same time, reaches a lattice temperature of just over 400 K, and also generates a strain wave, but with a lower amplitude compared to the one generated at the surface.

6.B FOURIER TRANSFORM OF FULL TIME INTERVAL

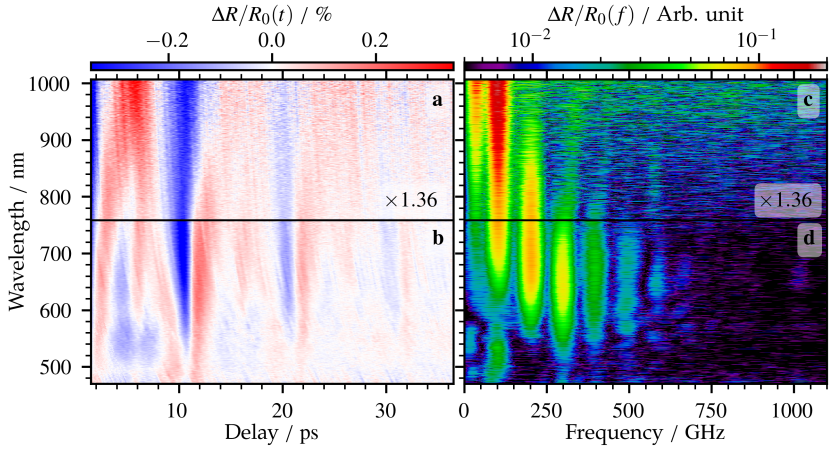

Figure 6.8: a and b: Measured strain-wave-induced changes in reflectance of a 30 nm thick layer of ruthenium on sapphire, after removing the thermal background. c and d: FFT amplitudes of the full time interval shown in a and b. The amplitudes in a and c are multiplied by a factor of 1.36, see Section 6.C.

The FFT of the 35 ps interval is shown in Figure 6.8. It largely resembles the spectrum of the first echo (Figure 6.2), but is modulated by 100 GHz, due to the 10 ps roundtrip time. Nonetheless, frequency components up to 600 GHz are still visible for probe wavelengths around 650 nm.

6.C SCALING OF THE LONGER-WAVELENGTH MEASUREMENT

There is a distinct difference in the amplitude of the changes in reflectance between the short-wavelength measurement, for wavelengths between 408 nm and 760 nm, and the long-wavelength measurement, between 730 nm and 1000 nm. By scaling the latter by a factor of 1.36, the measurements overlap quite well, as can be seen in Figure 6.9a and b. In Figure 6.9a, the change in reflectance, including thermal

background, is shown for a probe wavelength of 740 nm from the short- and long-wavelength, in blue and orange, respectively. Figure 6.9b, shows the background-removed changes in reflectance, induced by the strain wave, for probe wavelengths 730 nm, 740 nm, and 750 nm. The short-wavelength measurement is shown in blue and the long-wavelength measurement is shown in orange. The difference between the two sets of measurements are very small.

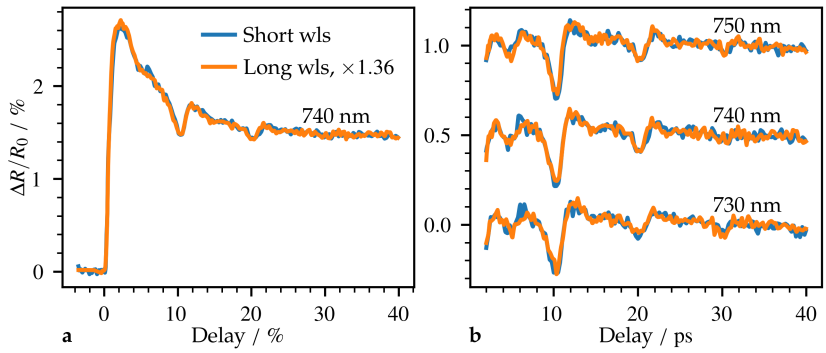

Figure 6.9: a. Comparison between the change in reflectance measured at 740 nm from the short-wavelength measurement (blue) and measured at the same wavelength from the long-wavelength measurement (orange), that is scaled by 1.36. b. Comparison between the strain-wave-induced reflectance changes at 730 nm, 740 nm, and 750 nm from the short- (blue) and long-wavelength (orange) measurement. The data from the long-wavelength measurement is scaled by 1.36, again. The curves are offset for visibility.

BIBLIOGRAPHY

[1] NVIDIA Corporation and Kristin Uchiyama. *NVIDIA Blackwell Platform Arrives to Power a New Era of Computing*. Tech. rep. NVIDIA Corporation, Mar. 2024.

[2] Sean Hollister. *Nvidia Reveals Blackwell B200 GPU, the 'World's Most Powerful Chip' for AI*. The Verge. Mar. 2024. URL: https://www.theverge.com/2024/3/18/24105157/nvidia-blackwell-gpu-b200-ai (visited on 11/15/2024).

[3] Hassan Mujtaba. *NVIDIA's Fully-Enabled Blackwell B200 GPUs Consume Up To 1200W, Completely Different Architecture From Hopper*. Mar. 2024. URL: https://wccftech.com/nvidia-fully-enabled-blackwell-b200-gpus-consume-1200w-completely-different-architecture-from-hopper/ (visited on 11/16/2024).

[4] Arie J den Boef. "Optical Wafer Metrology Sensors for Process-Robust CD and Overlay Control in Semiconductor Device Manufacturing". In: *Surface Topography: Metrology and Properties* 4.2 (Feb. 2016), p. 023001. DOI: 10.1088/2051-672x/4/2/023001.

[5] *What Is the Rayleigh Criterion?* URL: https://www.asml.com/en/technology/lithography-principles/rayleigh-criterion (visited on 11/20/2024).

[6] Rayleigh. "XXXI. *Investigations in Optics, with Special Reference to the Spectroscope*". In: *The London, Edinburgh, and Dublin Philosophical Magazine and Journal of Science* 8.49 (Oct. 1879), pp. 261–274. DOI: 10.1080/14786447908639684.

[7] César Javier Lockhart de la Rosa and Gouri Sankar Kar. *2D-material Based Devices in the Logic Scaling Roadmap*. URL: https://www.imec-int.com/en/articles/introducing-2d-material-based-devices-logic-scaling-roadmap (visited on 02/11/2025).

[8] Chris Mellor. *SK Hynix Breaks Barriers with 321-Layer 3D NAND*. Aug. 2023. URL: https://blocksandfiles.com/2023/08/09/sk-hynix-321-layer-flash-chip-sample/ (visited on 01/30/2025).

[9] Ashwath Rao and Neil Shah. *Scaling to 1,000-Layer 3D NAND in the AI Era*. Tech. rep. Counterpoint, Lam Research, July 2024.

[10] Bryon Moyer. *NAND Flash Targets 1,000 Layers*. Dec. 2024. URL: https://semiengineering.com/nand-flash-targets-1000-layers/ (visited on 01/30/2025).

[11] *3D Flash Memory "BiCS FLASH™" | KIOXIA - United States (English)*. URL: https://americas.kioxia.com/en-us/business/memory/bics.html (visited on 01/29/2025).

[12] C. Thomsen, H. T. Grahn, H. J. Maris, and J. Tauc. "Surface Generation and Detection of Phonons by Picosecond Light Pulses". In: *Phys. Rev. B* 34.6 (Sept. 1986), pp. 4129–4138. DOI: 10.1103/PhysRevB.34.4129.

[13] Stephen Edward. "Detection of Hidden Gratings Using Light and Sound". PhD thesis. 2020.

[14] Vanessa Verrina. "Laser-Induced Ultrasound for the Detection of Buried Micro- and Nano-Structures". PhD thesis. Amsterdam: University of Amsterdam, 2021.

[15] Stephen Edward, Hao Zhang, Irwan Setija, Vanessa Verrina, Alessandro Antoncecchi, Stefan Witte, and Paul Planken. "Detection of Hidden Gratings through Multilayer Nanostructures Using Light and Sound". In: *Phys. Rev. Applied* 14.1 (July 2020), p. 014015. DOI: 10.1103/PhysRevApplied.14.014015.

[16] V. Verrina, S. Edward, H. Zhang, S. Witte, and P. C. M. Planken. "Photoacoustic Detection of Low Duty Cycle Gratings through Optically Opaque Layers". In: *Appl. Phys. Lett.* 117.5 (Aug. 2020), p. 051104. DOI: 10.1063/5.0016078.

[17] Guido de Haan, Vanessa Verrina, Aurèle J. L. Adam, Hao Zhang, and Paul C. M. Planken. "Plasmonic Enhancement of Photoacoustic-Induced Reflection Changes". In: *Appl. Opt.* 60.24 (Aug. 2021), p. 7304. DOI: 10.1364/AO.432659.

[18] Thomas J. van den Hooven and Paul C.M. Planken. "Wavelength-Dependent Optical Detection of Strain Waves near Intrinsic and Artificial Optical Resonances". In: *Opt. Lett.* 50.5 (Jan. 2025), pp. 1445–1448. DOI: 10.1364/OL.551109.

[19] Sara Paolillo, Danny Wan, Frédéric Lazzarino, Nouredine Rassoul, Daniele Piumi, and Zsolt Tőkei. "Direct Metal Etch of Ruthenium for Advanced Interconnect". In: *Journal of Vacuum Science & Technology B, Nanotechnology and Microelectronics: Materials, Processing, Measurement, and Phenomena* 36.3 (May 2018), 03E103. DOI: 10.1116/1.5022283.

[20] Eugene Hecht. *Optics*. 4th ed. Harlow: Pearson, 2014.

[21] Max Born, Emil Wolf, and A. B Bhatia. *Principles of Optics*. 2019.

[22] Steven J. Byrnes. *Multilayer Optical Calculations*. Dec. 2020. DOI: 10.48550/arXiv.1603.02720. arXiv: 1603.02720 [physics]. (Visited on 12/02/2024).

[23] Edward D. Palik. *Handbook of Optical Constants of Solids*. 1. Aufl. s.l.: Elsevier professional, 1997.

[24] S.I. Anisimov, B.L. Kapeliovich, and T.L. Perel'man. "Electron Emission from the Metal Surfaces Induced by Ultrashort Lasers Pulses". In: *Zhurnal Ehksperimental'noj i Teoreticheskoj Fiziki*. Ehlektronnaya Ehmissiya s Poverkhnosti Metallov Pod Dejstviem Ul'trakorotkikh Lazernykh Impul'sov 66.2 (1974), pp. 776–781.

[25] J. Hohlfeld, S.-S. Wellershoff, J. Güdde, U. Conrad, V. Jähnke, and E. Matthias. "Electron and Lattice Dynamics Following Optical Excitation of Metals". In: *Chemical Physics* 251.1-3 (Jan. 2000), pp. 237–258. DOI: 10.1016/S0301-0104(99)00330-4.

[26] Mischa Bonn, Daniel N. Denzler, Stephan Funk, Martin Wolf, S.-Svante Wellershoff, and Julius Hohlfeld. "Ultrafast Electron Dynamics at Metal Surfaces: Competition between Electron-Phonon Coupling and Hot-Electron Transport". In: *Phys. Rev. B* 61.2 (Jan. 2000), pp. 1101–1105. DOI: 10.1103/PhysRevB.61.1101.

[27] Wolfgang S. M. Werner, Kathrin Glantschnig, and Claudia Ambrosch-Draxl. "Optical Constants and Inelastic Electron-Scattering Data for 17 Elemental Metals". In: *Journal of Physical and Chemical Reference Data* 38.4 (Dec. 2009), pp. 1013–1092. DOI: 10.1063/1.3243762.

[28] *ElementData Source Information—Wolfram Language Documentation*. URL: https://reference.wolfram.com/language/note/ElementDataSourceInformation.html (visited on 02/26/2025).

[29] Gregory V. Samsonov. *Handbook of the Physicochemical Properties of the Elements*. New York, NY: Springer, 1968.

[30] Chemical Rubber Company. *CRC Handbook of Chemistry and Physics: A Ready-Reference Book of Chemical and Physical Data*. Ed. by David R. Lide. 85. ed. Boca Raton: CRC Press, 2004.

[31] Lukas Novotny and Bert Hecht. *Principles of Nano-Optics*. Cambridge: Cambridge University Press, 2006.

[32] Jean-Jacques Greffet. "Introduction to Surface Plasmon Theory". In: *Plasmonics*. Ed. by Stefan Enoch and Nicolas Bonod. Vol. 167. Berlin, Heidelberg: Springer Berlin Heidelberg, 2012, pp. 105–148. DOI: 10.1007/978-3-642-28079-5_4.

[33] Heinz Raether. *Surface Plasmons on Smooth and Rough Surfaces and on Gratings*. Springer Tracts in Modern Physics 111. Berlin Heidelberg: Springer, 1988.

[34] Robert W. Boyd. *Nonlinear Optics*. Third edition. Amsterdam: Elsevier, 2008.

[35] Gadi Fibich and Alexander L. Gaeta. "Critical Power for Self-Focusing in Bulk Media and in Hollow Waveguides". In: *Opt. Lett.* 25.5 (Mar. 2000), p. 335. DOI: 10.1364/OL.25.000335.

[36] R. R. Alfano and S. L. Shapiro. "Observation of Self-Phase Modulation and Small-Scale Filaments in Crystals and Glasses". In: *Phys. Rev. Lett.* 24.11 (Mar. 1970), pp. 592–594. DOI: 10.1103/PhysRevLett.24.592.

[37] Maximilian Bradler. "Bulk Continuum Generation: The Ultimate Tool for Laser Applications and Spectroscopy: From New Insights to Ultrafast Amplifiers and Spectrometers". PhD thesis. Ludwig-Maximilians-Universität München, 2014. DOI: 10.5282/EDOC.17456.

[38] Paul A. Elzinga, Fred E. Lytle, Yanan Jian, Galen B. King, and Normand M. Laurendeau. "Pump/Probe Spectroscopy by Asynchronous Optical Sampling". In: *Appl Spectrosc* 41.1 (Jan. 1987), pp. 2–4. DOI: 10.1366/0003702874868025.

[39] Donna Strickland and Gerard Mourou. "Compression of Amplified Chirped Optical Pulses". In: *Optics Communications* 56.3 (Dec. 1985), pp. 219–221. DOI: 10.1016/0030-4018(85)90120-8.

[40] Giulio Cerullo and Sandro De Silvestri. "Ultrafast Optical Parametric Amplifiers". In: *Review of Scientific Instruments* 74.1 (Jan. 2003), pp. 1–18. DOI: 10.1063/1.1523642.

[41] Valentin G. Dmitriev, Gagik G. Gurzadjan, and David N. Nikogosjan. *Handbook of Nonlinear Optical Crystals*. 3. rev. ed., softcover reprint of the hardcover 3rd ed. 1999. Springer Series in Optical Sciences 64. Berlin: Springer, 2010.

[42] G. de Haan, E. Abram, T. J. van den Hooven, and P. C. M. Planken. "Plasmonic Enhancement of Photoacoustic Strain-Waves on Gold Gratings". In: *AIP Advances* 12.2 (Feb. 2022), p. 025227. DOI: 10.1063/5.0070630.

[43] Audrius Dubietis, Gintaras Tamošauskas, Rosvaldas Šuminas, Vytautas Jukna, and Arnaud Couairon. "Ultrafast Supercontinuum Generation in Bulk Condensed Media". In: *Lith. J. Phys.* 57.3 (Oct. 2017). DOI: 10.3952/physics.v57i3.3541.

[44] Bernhard Lang. "Photometrics of Ultrafast and Fast Broadband Electronic Transient Absorption Spectroscopy: State of the Art". In: *Review of Scientific Instruments* 89.9 (Sept. 2018), p. 093112. DOI: 10.1063/1.5039457.

[45] Andor and Oxford Instruments. *Introducing the ZL41 Wave Family*. Aug. 2024. (Visited on 08/22/2024).

[46] Alexander Scheeline. "How to Design a Spectrometer". In: *Appl Spectrosc* 71.10 (Oct. 2017), pp. 2237–2252. DOI: 10.1177/0003702817720468.

[47] Thomas J. van den Hooven and Paul C.M. Planken. "Surface-Plasmon-Enhanced Strain-Wave-Induced Optical Diffraction Changes from a Segmented Grating". In: *Photoacoustics* 31 (June 2023), p. 100497. DOI: 10.1016/j.pacs.2023.100497.

[48] Guanghua Yang, Jing Li, Yu Wang, Minxia Ding, and Lina Zhong. "Analytic Design of Segmented Phase Grating for Optical Sensing in High-Precision Alignment System". In: *Sensors* 21.11 (May 2021), p. 3805. DOI: 10.3390/s21113805.

[49] M. Miyasaka, H. Saito, T. Tamura, T. Uchiyama, Paul Hinnen, Hyun-Woo Lee, Marc van Kemenade, Mir Shahrjerdy, and Robert van Leeuwen. "The Application of SMASH Alignment System for 65-55-Nm Logic Devices". In: *Advanced Lithography*. Ed. by Chas N. Archie. San Jose, CA, Mar. 2007, 65180H. DOI: 10.1117/12.711059.

[50] MGMM (Mark) Van Kraaij. "Forward Diffraction Modelling:Analysis and Application to Grating Reconstruction". In: (2011). DOI: 10.6100/IR702579.

[51] R. Ritchie, E. Arakawa, J. Cowan, and R. Hamm. "Surface-Plasmon Resonance Effect in Grating Diffraction". In: *Phys. Rev. Lett.* 21.22 (Nov. 1968), pp. 1530–1533. DOI: 10.1103/PhysRevLett.21.1530.

[52] Ye-Yung Teng and Edward A. Stern. "Plasma Radiation from Metal Grating Surfaces". In: *Phys. Rev. Lett.* 19.9 (Aug. 1967), pp. 511–514. DOI: 10.1103/PhysRevLett.19.511.

[53] Francisco Jose Torcal-Milla, Luis Miguel Sanchez-Brea, and Eusebio Bernabeu. "Diffraction of Gratings with Rough Edges". In: *Opt. Express* 16.24 (Nov. 2008), p. 19757. DOI: 10.1364/OE.16.019757.

[54] Joseph W. Goodman. *Introduction to Fourier Optics*. 2. ed. McGraw-Hill Series in Electrical and Computer Engineering. New York: McGraw-Hill, 1996.

[55] Itai Epstein, Ido Dolev, Doron Bar-Lev, and Ady Arie. "Plasmon-Enhanced Bragg Diffraction". In: *Phys. Rev. B* 86.20 (Nov. 2012), p. 205122. DOI: 10.1103/PhysRevB.86.205122.

[56] O.T.A. Janssen, H.P. Urbach, and G.W. t Hooft. "On the Phase of Plasmons Excited by Slits in a Metal Film". In: *Opt. Express* 14.24 (Nov. 2006), p. 11823. DOI: 10.1364/OE.14.011823.

[57] Akbar Safari, Robert Fickler, Enno Giese, Omar S. Magaña-Loaiza, Robert W. Boyd, and Israel De Leon. "Measurement of the Photon-Plasmon Coupling Phase Shift". In: *Phys. Rev. Lett.* 122.13 (Apr. 2019), p. 133601. DOI: 10.1103/PhysRevLett.122.133601.

[58] Rogier Groeneveld, Rudolf Sprik, and Ad Lagendijk. "Ultrafast Relaxation of Electrons Probed by Surface Plasmons at a Thin Silver Film". In: *Phys. Rev. Lett.* 64.7 (Feb. 1990), pp. 784–787. DOI: 10.1103/PhysRevLett.64.784.

[59] Nir Rotenberg, Markus Betz, and Henry M. van Driel. "Ultrafast Control of Grating-Assisted Light Coupling to Surface Plasmons". In: *Opt. Lett., OL* 33.18 (Sept. 2008), pp. 2137–2139. DOI: 10.1364/OL.33.002137.

[60] Qing Li et al. "Generation and Control of Ultrashort-Wavelength Two-Dimensional Surface Acoustic Waves at Nanoscale Interfaces". In: *Phys. Rev. B* 85.19 (May 2012), p. 195431. DOI: 10.1103/PhysRevB.85.195431.

[61] Osamu Matsuda, Maria Cristina Larciprete, Roberto Li Voti, and Oliver B. Wright. "Fundamentals of Picosecond Laser Ultrasonics". In: *Ultrasonics* 56 (Feb. 2015), pp. 3–20. DOI: 10.1016/j.ultras.2014.06.005.

[62] Pascal Ruello and Vitalyi E. Gusev. "Physical Mechanisms of Coherent Acoustic Phonons Generation by Ultrafast Laser Action". In: *Ultrasonics* 56 (Feb. 2015), pp. 21–35. DOI: 10.1016/j.ultras.2014.06.004.

[63] H.-N. Lin, H. J. Maris, L. B. Freund, K. Y. Lee, H. Luhn, and D. P. Kern. "Study of Vibrational Modes of Gold Nanostructures by Picosecond Ultrasonics". In: *Journal of Applied Physics* 73.1 (Jan. 1993), pp. 37–45. DOI: 10.1063/1.353859.

[64] A.M. Aindow, R.J. Dewhurst, and S.B. Palmer. "Laser-Generation of Directional Surface Acoustic Wave Pulses in Metals". In: *Optics Communications* 42.2 (June 1982), pp. 116–120. DOI: 10.1016/0030-4018(82)90378-9.

[65] Z.H. Shen, B.Q. Xu, X.W. Ni, J. Lu, and S.Y. Zhang. "Theoretical Study on Line Source Laser-Induced Surface Acoustic Waves in Two-Layer Structure in Ablative Regime". In: *Optics & Laser Technology* 36.2 (Mar. 2004), pp. 139–143. DOI: 10.1016/j.optlastec.2003.08.001.

[66] Taiki Saito, Osamu Matsuda, Motonobu Tomoda, and Oliver B. Wright. "Imaging Gigahertz Surface Acoustic Waves through the Photoelastic Effect". In: *J. Opt. Soc. Am. B* 27.12 (Dec. 2010), p. 2632. DOI: 10.1364/JOSAB.27.002632.

[67] I. A. Viktorov. *Rayleigh and Lamb Waves: Physical Theory and Applications*. New York: Springer Science + Business Media, 2013.

[68] O.B. Wright and V.E. Gusev. "Ultrafast Acoustic Phonon Generation in Gold". In: *Physica B: Condensed Matter* 219–220 (Apr. 1996), pp. 770–772. DOI: 10.1016/0921-4526(95)00880-2.

[69] Vasily V. Temnov, Christoph Klieber, Keith A. Nelson, Tim Thomay, Vanessa Knittel, Alfred Leitenstorfer, Denys Makarov, Manfred Albrecht, and Rudolf Bratschitsch. "Femtosecond Nonlinear Ultrasonics in Gold Probed with Ultrashort Surface Plasmons". In: *Nat Commun* 4.1 (June 2013), p. 1468. DOI: 10.1038/ncomms2480.

[70] Jincheng Wang, Jian Wu, and Chunlei Guo. "Resolving Dynamics of Acoustic Phonons by Surface Plasmons". In: *Opt. Lett.* 32.6 (Mar. 2007), p. 719. DOI: 10.1364/OL.32.000719.

[71] Nir Rotenberg, Jan N. Caspers, and Henry M. van Driel. "Tunable Ultrafast Control of Plasmonic Coupling to Gold Films". In: *Phys. Rev. B* 80.24 (Dec. 2009), p. 245420. DOI: 10.1103/PhysRevB.80.245420.

[72] Vasily V. Temnov. "Ultrafast Acousto-Magneto-Plasmonics". In: *Nature Photon* 6.11 (Nov. 2012), pp. 728–736. DOI: 10.1038/nphoton.2012.220.

[73] O.B Wright, T. Hyoguchi, and K. Kawashima. "CHARACTERIZATION OF TRANSPARENT AND OPAQUE THIN FILMS USING LASER PICOSECOND ULTRASONICS". In: *Nondestructive Testing and Evaluation* 7.1-6 (June 1992), pp. 149–163. DOI: 10.1080/10589759208952995.

[74] B. C. Daly, N. C. R. Holme, T. Buma, C. Branciard, T. B. Norris, D. M. Tennant, J. A. Taylor, J. E. Bower, and S. Pau. "Imaging Nanostructures with Coherent Phonon Pulses". In: *Applied Physics Letters* 84.25 (June 2004), pp. 5180–5182. DOI: 10.1063/1.1764599.

[75] Alessandro Antoncecchi, Hao Zhang, Stephen Edward, Vanessa Verrina, Paul C. M. Planken, and Stefan Witte. "High-Resolution Microscopy through Optically Opaque Media Using Ultrafast Photoacoustics". In: *Opt. Express* 28.23 (Nov. 2020), p. 33937. DOI: 10.1364/OE.405875.

[76] Chuan He, Oliver Ristow, Martin Grossmann, Delia Brick, Yuning Guo, Martin Schubert, Mike Hettich, Vitalyi Gusev, and Thomas Dekorsy. "Acoustic Waves Undetectable by Transient Reflectivity Measurements". In: *Phys. Rev. B* 95.18 (May 2017), p. 184302. DOI: 10.1103/PhysRevB.95.184302.

[77] A. Devos and A. Le Louarn. "Strong Effect of Interband Transitions in the Picosecond Ultrasonics Response of Metallic Thin Films". In: *Phys. Rev. B* 68.4 (July 2003), p. 045405. DOI: 10.1103/PhysRevB.68.045405.

[78] F. Noll, N. Krauß, V. Gusev, T. Dekorsy, and M. Hettich. "Surface Plasmon-Based Detection for Picosecond Ultrasonics in Planar Gold-Dielectric Layer Geometries". In: *Photoacoustics* 30 (Apr. 2023), p. 100464. DOI: 10.1016/j.pacs.2023.100464.

[79] Martin van Exter and Ad Lagendijk. "Ultrashort Surface-Plasmon and Phonon Dynamics". In: *Phys. Rev. Lett.* 60.1 (Jan. 1988), pp. 49–52. DOI: 10.1103/PhysRevLett.60.49.

[80] N. Egede Christensen and B. O. Seraphin. "Relativistic Band Calculation and the Optical Properties of Gold". In: *Phys. Rev. B* 4.10 (Nov. 1971), pp. 3321–3344. DOI: 10.1103/PhysRevB.4.3321.

[81] R. W. Schoenlein, W. Z. Lin, J. G. Fujimoto, and G. L. Eesley. "Femtosecond Studies of Nonequilibrium Electronic Processes in Metals". In: *Phys. Rev. Lett.* 58.16 (Apr. 1987), pp. 1680–1683. DOI: 10.1103/PhysRevLett.58.1680.

[82] V. V. Kruglyak, R. J. Hicken, P. Matousek, and M. Towrie. "Spectroscopic Study of Optically Induced Ultrafast Electron Dynamics in Gold". In: *Phys. Rev. B* 75.3 (Jan. 2007), p. 035410. DOI: 10.1103/PhysRevB.75.035410.

[83] C.-K. Sun, F. Vallée, L. H. Acioli, E. P. Ippen, and J. G. Fujimoto. "Femtosecond-Tunable Measurement of Electron Thermalization in Gold". In: *Phys. Rev. B* 50.20 (Nov. 1994), pp. 15337–15348. DOI: 10.1103/PhysRevB.50.15337.

[84] Ryosuke Hayashi, Atsushi Iwasaki, Parinda Vasa, and Kaoru Yamanouchi. "Determination of Electron and Phonon Temperatures in Gold Thin Film Irradiated with an Ultrashort Laser Pulse". In: *AIP Advances* 12.9 (Sept. 2022), p. 095207. DOI: 10.1063/5.0090466.

[85] A. Devizis, V. Vaicikauskas, and V. Gulbinas. "Ultrafast Pump-Probe Surface Plasmon Resonance Spectroscopy of Thin Gold Films". In: *Appl. Opt.* 45.11 (Apr. 2006), p. 2535. DOI: 10.1364/AO.45.002535.

[86] Alexandre A. Kolomenskii, Ryan Mueller, Joshua Wood, James Strohaber, and Hans A. Schuessler. "Femtosecond Electron-Lattice Thermalization Dynamics in a Gold Film Probed by Pulsed Surface Plasmon Resonance". In: *Appl. Opt.* 52.30 (Oct. 2013), p. 7352. DOI: 10.1364/AO.52.007352.

[87] Martin Schubert, Martin Grossmann, Chuan He, Delia Brick, Patricia Scheel, Oliver Ristow, Vitalyi Gusev, and Thomas Dekorsy. "Generation and Detection of Gigahertz Acoustic Oscillations in Thin Membranes". In: *Ultrasonics* 56 (Feb. 2015), pp. 109–115. DOI: 10.1016/j.ultras.2014.06.018.

[88] Florian Hudert, Axel Bruchhausen, Daniel Issenmann, Olivier Schecker, Reimar Waitz, Artur Erbe, Elke Scheer, Thomas Dekorsy, Adnen Mlayah, and Jean-Roch Huntzinger. "Confined Longitudinal Acoustic Phonon Modes in Free-Standing Si Membranes Coherently Excited by Femtosecond Laser Pulses". In: *Phys. Rev. B* 79.20 (May 2009), p. 201307. DOI: 10.1103/PhysRevB.79.201307.

[89] Robert L. Olmon, Brian Slovick, Timothy W. Johnson, David Shelton, Sang-Hyun Oh, Glenn D. Boreman, and Markus B. Raschke. "Optical Dielectric Function of Gold". In: *Physical Review B* 86.23 (Dec. 2012), p. 235147. DOI: 10.1103/PhysRevB.86.235147.

[90] P. Kapur, J.P. McVittie, and K.C. Saraswat. "Technology and Reliability Constrained Future Copper Interconnects. I. Resistance Modeling". In: *IEEE Trans. Electron Devices* 49.4 (Apr. 2002), pp. 590–597. DOI: 10.1109/16.992867.

[91] Daniel Gall. "The Search for the Most Conductive Metal for Narrow Interconnect Lines". In: *Journal of Applied Physics* 127.5 (Feb. 2020), p. 050901. DOI: 10.1063/1.5133671.

[92] William J. Mitchell, Brian J. Thibeault, Demis D. John, and Thomas E. Reynolds. "Highly Selective and Vertical Etch of Silicon Dioxide Using Ruthenium Films as an Etch Mask". In: *Journal of Vacuum Science & Technology A: Vacuum, Surfaces, and Films* 39.4 (July 2021), p. 043204. DOI: 10.1116/6.0001030.

[93] Zhiying Chen, Alok Ranjan, and Peter Ventzek. "Ruthenium Hard Mask Process". US20200051833A1. Feb. 2020.

[94] Yen-Tien Lu, Kai-Hung YU, and Angelique RALEY. "Method for Using Ultra Thin Ruthenium Metal Hard Mask for Etching Profile Control". WO2021021456A1. Feb. 2021.

[95] Komal Chaudhary, Maksym Illienko, Thomas J. van den Hooven, Stefan Witte, and Paul Planken. "Optically Enhancing and Controlling Photoacoustic Signals Using Ultra-Thin Semiconductor Coatings on Metal Surfaces". In: *Opt. Express* 33.1 (Jan. 2025), p. 199. DOI: 10.1364/OE.544902.

[96] Fedor Akhmetov, Igor Milov, Sergey Semin, Fabio Formisano, Nikita Medvedev, Jacobus M. Sturm, Vasily V. Zhakhovsky, Igor A. Makhotkin, Alexey Kimel, and Marcelo Ackermann. "Laser-Induced Electron Dynamics and Surface Modification in Ruthenium Thin Films". In: *Vacuum* 212 (June 2023), p. 112045. DOI: 10.1016/j.vacuum.2023.112045.

[97] Fedor Akhmetov, Jan Vorberger, Igor Milov, Igor Makhotkin, and Marcelo Ackermann. "Ab Initio-Simulated Optical Response of Hot Electrons in Gold and Ruthenium". In: *Opt. Express* 32.11 (May 2024), p. 19117. DOI: 10.1364/OE.522772.

[98] Lorenzo Cruciani, Stefan Van Vliet, Alessandro Troglia, Roland Bliem, Klaasjan Van Druten, and Paul Planken. "Femtosecond Laser-Induced Emission of Coherent Terahertz Pulses from Ruthenium Thin Films". In: *J. Phys. Chem. C* (Nov. 2023), acs.jpcc.3c05525. DOI: 10.1021/acs.jpcc.3c05525.

[99] Lorenzo Cruciani, Marnix Vreugdenhil, Stefan Van Vliet, Ester Abram, Dries Van Oosten, Roland Bliem, Klaasjan Van Druten, and Paul Planken. "Direct Laser Patterning of Ruthenium below the Optical Diffraction Limit". In: *Applied Physics Letters* 124.17 (Apr. 2024), p. 171902. DOI: 10.1063/5.0205538.

[100] G. de Haan, T. J. van den Hooven, and P. C. M. Planken. "Ultrafast Laser-Induced Strain Waves in Thin Ruthenium Layers". In: *Opt. Express* 29.20 (Sept. 2021), p. 32051. DOI: 10.1364/OE.438286.

[101] Fedor Akhmetov, Igor Milov, Igor A. Makhotkin, Marcelo Ackermann, and Jan Vorberger. "Electron-Phonon Coupling in Transition Metals beyond Wang's Approximation". In: *Phys. Rev. B* 108.21 (Dec. 2023), p. 214301. DOI: 10.1103/PhysRevB.108.214301.

[102] Yu. Petrov, K. Migdal, N. Inogamov, V. Khokhlov, D. Ilnitsky, I. Milov, N. Medvedev, V. Lipp, and V. Zhakhovsky. "Ruthenium under Ultrafast Laser Excitation: Model and Dataset for Equation of State, Conductivity, and Electron-Ion Coupling". In: *Data in Brief* 28 (Feb. 2020), p. 104980. DOI: 10.1016/j.dib.2019.104980.

[103] P. Babilotte, P. Ruello, D. Mounier, T. Pezeril, G. Vaudel, M. Edely, J-M. Breteau, V. Gusev, and K. Blary. "Femtosecond Laser Generation and Detection of High-Frequency Acoustic Phonons in GaAs Semiconductors". In: *Phys. Rev. B* 81.24 (June 2010), p. 245207. DOI: 10.1103/PhysRevB.81.245207.

[104] Maksym Illienko, Matthias C. Velsink, and Stefan Witte. "Understanding Photoacoustic Signal Formation in the Presence of Transparent Thin Films". In: *Photoacoustics* 38 (Aug. 2024), p. 100617. DOI: 10.1016/j.pacs.2024.100617.

SUMMARY

BROADBAND OPTICAL DETECTION OF ULTRAFAST STRAIN WAVES IN METALS

The transistors in semiconductor devices are expected to continue to decrease in size and both the transistors and the devices are expected to increase in complexity, in the coming years. Since these devices are produced layer-by-layer, the vertical alignment of the features in every layer, with respect to the layer below it, is crucial to make working devices. To align the layers as well as possible, the position and deformation of the wafer is measured just before the patterns are transferred to the layer via lithographic exposure. The wafer is aligned by measuring the position of several alignment markers, which are gratings etched into the silicon wafer, with (sub-)nanometre accuracy via the diffraction of visible light.

In some production process steps, for example in the production of 3D NAND, a thick, opaque layer is deposited onto the wafer, also covering the alignment markers. This layer prohibits the diffraction of light from the original markers, since they are buried underneath the opaque layers. As a result, their position cannot be determined with the required accuracy.

It has been demonstrated that ultrafast, laser-induced strain waves can be used to detect the alignment grating buried underneath opaque layers. This works as follows: A strain wave is generated at the surface of the opaque layer, by rapid heating of the volume near the surface following absorption of a femtosecond laser pulse. The strain wave propagates down through the opaque layer, and through the product layers below it, towards the buried grating. There, it reflects, copying the shape, and in particular the spatial periodicity, of the buried grating onto its wavefront. The reflected strain wave propagates up through all layers. At the surface of the opaque layer, the wave modifies the optical properties and also deforms the surface, with the same spatial periodicity as the buried grating. A time-delayed probe pulse can diffract from these periodic modifications, and thus the buried grating can be detected.

The diffraction efficiency is unfortunately too low for the practical application of this method to detect buried gratings. Since the generation of strain waves is limited by the materials used in the production of semiconductors, which cannot be changed, only the detection of strain waves can be improved. In this thesis, we present research into improving the optical detection of ultrafast strain waves in the metals gold and ruthenium, by investigating the wavelength dependence of the detection process.

In Chapter 4, the surface plasmon polariton-enhancement of the strain-wave-induced changes in diffraction and reflectance of a gold-covered, segmented grating are investigated. The segmented grating combines the previously discovered enhancement of strain-wave-induced reflectance changes of a plasmonic grating, with a long-period alignment grating. In practice, the segmented grating is a sub-wavelength-period grating that is amplitude modulated with a longer-period grating. Surprisingly, the spatially modulated grating leads to *three* surface plasmon polariton resonances, as the spatial frequency sidebands can also be used to

generate surface plasmon polaritons. By using a tunable probe pulse, the strain-wave-induced changes in reflectance and diffraction of the segmented grating are measured as a function of probe wavelength. Probing with wavelengths close to the resonances results in changes in reflectance, induced by longitudinal strain waves, that are up to a factor of 36 larger than at wavelengths far away from the resonances. In diffraction, the changes are up to an additional factor of 2.6 larger than in reflection.

Detection of strain waves by changing the optical wavelength of the probe pulse is rather time-consuming and limited in spectral resolution. To investigate the wavelength-dependence of optical strain-wave detection more efficiently, an ultrafast reflection spectrometer was build. The spectrometer uses a white light continuum probe pulse to simultaneously measure the (strain-wave-induced) reflectance changes over a range of about 300 nm. Chapter 3 describes the spectrometer, including the laser system used to generate the ultrashort laser pulses. The spectrometer decreases the required measurement time drastically, while also improving spectral resolution, compared to the previous single-wavelength measurements.

In Chapter 5, the spectrometer is used to measure strain-wave-induced changes in reflectance of the gold-covered, segmented grating, for wavelengths between 470 nm and 760 nm. This range includes the three surface plasmon polariton resonances, but also includes the s/p- to d-band interband transition of gold, for wavelengths around 520 nm. We find that the strain-wave-induced changes in reflectance for probe wavelengths near the interband transition were, surprisingly, almost as large as those near the surface plasmon polariton resonances. This is somewhat unexpected, as there are large differences in the reflection spectrum between wavelengths near the surface plasmon polariton resonances and around the interband transition. Near the surface plasmon polariton resonances, the reflectance rapidly changes as a function of wavelength, but near the interband transition, the reflectance only gradually increases with wavelength.

Finally, the wavelength-dependence of the optical detection of ultrafast strain waves in a 30 nm ruthenium layer is investigated and presented in Chapter 6. For this, two sets of measurement, for probe wavelengths between 470 nm and 760 nm and between 730 nm and 1000 nm, were combined. We find that the strain-wave-induced changes become sharper and shorter as the probe wavelength decreases. This corresponds to an increase of the maximum strain-wave frequency that can be optically detected, for shorter probe wavelengths. We find that this frequency is inversely proportional to the optical penetration depth of the probe wavelength. Surprisingly, there are some gaps in the measured strain-wave spectrum. For strain-wave frequencies lower than 150 GHz, no changes are measured for probe wavelengths around 650 nm. Similarly, there are no changes for frequencies around 200 GHz for wavelengths between 475 nm and 545 nm. The absence of changes for these frequencies at probe wavelengths is accompanied by a change in phase for frequencies lower than 200 GHz at wavelengths shorter than 580 nm.

In conclusion, the results presented in this thesis show that the optical response of metals, such as gold and ruthenium, to strain waves strongly depends on the optical wavelength that is used to probe the strain waves. Furthermore, we have shown that it typically is not possible to predict the strength of the optical response from the reflectance spectrum, which highlights the importance of wavelength-dependent experiments.

SAMENVATTING

BREEDBANDIGE OPTISCHE DETECTIE VAN ULTRASNELLE AKOESTISCHE GOLVEN IN METALEN

De verwachting is dat transistoren in halfgeleiderproducten de komende jaren verder zullen krimpen. Tegelijkertijd zullen dat zowel de transistoren als de producten in complexiteit toenemen. Aangezien deze producten laag voor laag op een wafer worden gefabriceerd, is de onderlinge verticale uitlijning van deze lagen essentieel voor het fabriceren van werkende producten. Om de lagen zo goed mogelijk uit te lijnen, worden de positie en vervorming van de wafer opgemeten. Dit gebeurt net voordat de patronen van de te fabriceren laag op de wafer worden overbracht in de belichtingsstap van het fotolithografische proces. Voor de uitlijning wordt de positie van meerdere zogenoemde 'uitlijningsmarkeringen' (alignment markers), dit zijn tralies geëtst in de wafer, met nanometer precisie gemeten via de diffractie van zichtbaar light aan deze markeringen.

Tijdens het productieproces van sommige producttypes, zoals bijvoorbeeld 3D NAND, wordt er een (relatief) dikke, ondoorzichtige laag op de wafer gedeponeerd, die ook de uitlijningsmarkeringen bedekt. Deze laag verhindert de diffractie van licht aan de originele markeringen, aangezien die bedolven zijn door de ondoorzichtige laag. Hierdoor kan de positie van de markeringen niet met de benodigde precisie bepaald worden.

Het is reeds gedemonstreerd dat ultrasnelle akoestische golven, opgewekt met ultrakorte laserpulsen, kunnen worden gebruikt om de bedolven markeringen te detecteren. Dit werkt als volgt: De akoestische golf wordt aan het oppervlak van de ondoorzichtige laag opgewekt, door de snelle verhitting van dit volume door absorptie van een femtoseconde laserpuls. De golf propageert naar beneden, richting de markering, door de ondoorzichtige laag en de overige lagen van het product. Wanneer de akoestische golf bij de markering is, zal deze reflecteren, waarbij de vorm van de markering, en met name de ruimtelijke periodiciteit, in het gereflecteerde golffront wordt gekopieerd. De gereflecteerde golf propageert vervolgens terug naar boven. De golf, wanneer deze aan het oppervlak van de ondoorzichtige laag is, verandert de optische eigenschappen en vervormt het oppervlak, met dezelfde ruimtelijke periodiciteit als de bedolven markering. De diffractie van een tijdsvertraagde tweede puls aan deze periodische veranderingen kan vervolgens worden gebruikt om het verborgen tralie te detecteren.

De diffractieëfficientie is, helaas, te laag om deze methode in de praktijk toe te passen. Aangezien de generatie van de akoestische golven is gelimiteerd door de gebruikte materialen, die niet zomaar gewijzigd kunnen worden, kan alleen de detectie van de akoestische golven worden verbeterd. In dit proefschrift presenteren we onderzoek naar het verbeteren van de optische detectie van ultrasnelle akoestische golven in de metalen goud en ruthenium, door de golflengteafhankelijkheid van het detectieproces te onderzoeken.

In Chapter 4 wordt de versterking van veranderingen, veroorzaakt door akoestische golven, in reflectie en diffractie, via oppervlakte-plasmon-polariton-resonanties,

aan een met goud bedekt en gesegmenteerd tralie onderzocht. Het gesegmenteerde tralie combineert de eerder ontdekte versterking van reflectieveranderingen, veroorzaakt door akoestische golven, van een plasmonisch tralie met een tralie met een langere periode, zoals gebruikt als uitlijningsmarkeringen. In de praktijk is het gesegmenteerde tralie een tralie met een zeer korte periode, dat amplitude-gemoduleerd wordt met een tralie met een langere periode. Verrassend genoeg leidt de amplitudemodulatie tot drie oppervlakte-plasmon-polariton-resonantie, aangezien de ruimtelijke frequentiezijbanden, die door de modulatie zijn ontstaan, ook kunnen worden gebruikt om oppervlakte-plasmon-polaritonen op te wekken. De veranderingen in reflectie en diffractie, veroorzaakt door de akoestische golven, worden gemeten als functie van de sondegolflengte, met behulp van een in golflengte afstembare sondepuls. Voor sondegolflengtes die dicht bij de golflengtes van de resonanties liggen, zijn de veranderingen in reflectie die veroorzaakt worden door longitudinale akoestische golven tot 36 keer groter dan de veranderingen voor golflengtes ver weg van de resonanties. Voor de diffractiemetingen zijn de veranderingen nog tot 2.6 keer groter vergeleken met de reflectiemetingen.

Het meten van de golflengteafhankelijkheid van de detectie van akoestische golven door het veranderen van de golflengte van de sondepuls is helaas tijdsintensief, daarnaast is de spectrale resolutie van deze methode beperkt. Om de golflengteafhankelijkheid efficiënter te meten, is er een spectrometer ontworpen en gebouwd die de ultrasnelle reflectieveranderingen kan meten. Deze spectrometer gebruikt een witlichtcontinuumpuls om reflectieveranderingen (veroorzaakt door de akoestische golven) over een bereik van 300 nm gelijktijdig te meten. In Chapter 3 wordt deze spectrometer en het lasersysteem, dat gebruikt wordt om de ultrakorte pulsen te genereren, beschreven. De spectrometer verkort de meettijd drastisch en verbeterd de spectrale resolutie in vergelijking met de eerder meetmethode.

In Chapter 5 wordt de spectrometer voor het eerst gebruikt om de veranderingen in reflectie, veroorzaakt door akoestische golven, van het met goud bedekte gesegmenteerde tralie te meten, voor golflengtes tussen 470 nm en 760 nm. Dit golflengtebereik omvat de drie oppervlakte-plasmon-polariton-resonanties, maar omvat ook de elektronische interbandovergang van de s/p- naar de d-band in goud, die plaatsvindt voor golflengtes rondom 520 nm. De gemeten veranderingen in reflectie, veroorzaakt door akoestische golven, voor golflengtes rondom de interbandovergang waren verrassend genoeg bijna net zo groot als de gemeten veranderingen rondom de oppervlakte-plasmon-polariton-resonanties. Dit is enigszins onverwacht, aangezien er grote verschillen zijn in het reflectiespectrum tussen de oppervlakte-plasmon-polariton-resonanties en de interbandovergang. Rondom de oppervlakte-plasmon-polariton-resonanties verandert de reflectie zeer snel, als functie van de golflengte, maar in de buurt van de interbandovergang neemt de reflectie slechts geleidelijk toe met de golflengte.

Als laatste wordt de golflengteafhankelijkheid van de optische detectie van ultrasnelle akoestische golven in een 30 nm dikke ruthenium laag onderzocht en dit wordt in Chapter 6 gepresenteerd. In dit hoofdstuk worden twee meetreeksen gecombineerd tot een meetbereik van 470 nm tot 1000 nm. De gemeten reflectieveranderingen, veroorzaakt door akoestische golven, worden scherper en korter naar mate de sondegolflengte korter wordt. Dit komt overeen met een toename van de maximale frequentie van de akoestische golven die gedetecteerd kan worden, voor kortere sondegolflengtes. We stellen vast dat deze frequentie omgekeerd

evenredig is aan de optische penetratiediepte van de gebruikte sondegolflengte. Verrassend genoeg worden er voor sommige golflengtes bij bepaalde frequenties (lager dan de maximale frequentie) geen veranderingen gemeten. Voor frequenties lager dan 150 GHz worden er bijvoorbeeld geen veranderingen gemeten voor golflengtes rondom 650 nm. Hetzelfde geldt voor frequenties rondom 200 GHz voor golflengtes tussen 475 nm en 545 nm. De afwezigheid van veranderingen voor deze frequenties gaat gepaard met een verandering in de fase van de gemeten frequenties korter dan 200 GHz voor golflengtes korter dan 580 nm.

Tot slot laten de resultaten die in dit proefschrift worden gepresenteerd zien dat de optische reactie van metalen, zoals goud en ruthenium, op akoestische golven sterk afhankelijk is van de golflengte waarmee de golven worden gesondeerd. Daarnaast hebben we aangetoond dat het doorgaans niet mogelijk is de sterkte van de optische reactie te voorspellen op basis van het reflectiespectrum, wat het belang van golflengteafhankelijke experimenten onderstreept.

PUBLICATIONS

This thesis is based on the following publications:

[1] Thomas J. van den Hooven and Paul C.M. Planken. "Surface-Plasmon-Enhanced Strain-Wave-Induced Optical Diffraction Changes from a Segmented Grating". In: *Photoacoustics* 31 (June 2023), p. 100497. DOI: 10.1016/j.pacs.2023.100497.
Presented in Chapter 4.

[2] Thomas J. van den Hooven and Paul C.M. Planken. "Wavelength-Dependent Optical Detection of Strain Waves near Intrinsic and Artificial Optical Resonances". In: *Opt. Lett.* 50.5 (Jan. 2025), pp. 1445–1448. DOI: 10.1364/OL.551109.
Presented in Chapter 5.

[3] Thomas J. van den Hooven, Lorenzo Cruciani, and Paul C.M. Planken. "Broadband Optical Detection of Ultrafast Strain Waves in Ruthenium". In preparation.
Presented in Chapter 6

The author contributed to the following published works:

[4] G. de Haan, T. J. van den Hooven, and P. C. M. Planken. "Ultrafast Laser-Induced Strain Waves in Thin Ruthenium Layers". In: *Opt. Express* 29.20 (Sept. 2021), p. 32051. DOI: 10.1364/OE.438286.

[5] G. de Haan, E. Abram, T. J. van den Hooven, and P. C. M. Planken. "Plasmonic Enhancement of Photoacoustic Strain-Waves on Gold Gratings". In: *AIP Advances* 12.2 (Feb. 2022), p. 025227. DOI: 10.1063/5.0070630.

[6] Z. Nie, L. Guery, E. B. Molinero, P. Juergens, T. J. Van Den Hooven, Y. Wang, A. Jimenez Galan, P. C. M. Planken, R. E. F. Silva, and P. M. Kraus. "Following the Nonthermal Phase Transition in Niobium Dioxide by Time-Resolved Harmonic Spectroscopy". In: *Phys. Rev. Lett.* 131.24 (Dec. 2023), p. 243201. DOI: 10.1103/PhysRevLett.131.243201.

[7] Zhonghui Nie, Kevin Murzyn, Leo Guery, Thomas J. van den Hooven, and Peter M. Kraus. "Ultrafast Permittivity Engineering Enables Broadband Enhancement and Spatial Emission Control of Harmonic Generation in ZnO". In: *ACS Photonics* (Nov. 2024), acsphotonics.4c01737. DOI: 10.1021/acsphotonics.4c01737.

[8] Komal Chaudhary, Maksym Illienko, Thomas J. van den Hooven, Stefan Witte, and Paul Planken. "Optically Enhancing and Controlling Photoacoustic Signals Using Ultra-Thin Semiconductor Coatings on Metal Surfaces". In: *Opt. Express* 33.1 (Jan. 2025), p. 199. DOI: 10.1364/OE.544902.

The author contribution are listed in the Table 7.1.

Table 7.1: Research contribution of the publications, TH: Thomas J. van den Hooven, PP: Paul C.M. Planken, LC: Lorenzo Cruciani. From the publications [4-8], marked with a *, only the contributions from TH are listed.

Publication	Conceptualization	Data Acquisition	Data Analysis	Manuscript Preparation	Writing (Original Draft)	Writing (Review)	Supervision
[1]	TH, PP	TH	TH	TH	TH	TH, PP	PP
[2]	TH, PP	TH	TH	TH	TH	TH, PP	PP
[3]	TH, PP	TH, LC	TH	TH	TH	TH, PP, LC	PP
[4]*	-	TH	-	-	-	TH	–
[5]*	-	TH	-	-	-	TH	–
[6]*	-	TH	-	-	-	TH	–
[7]*	-	TH	-	-	-	TH	–
[8]*	-	TH	-	-	-	TH	–

ACRONYMS

ADC	analog-to-digital converter	26
AFM	atomic-force microscopy	40
AOI	angle of incidence	65
ARCNL	Advanced Research Center for Nanolithography	112
BBO	β-barium borate	79
BaF_2	barium fluoride	79
CMOS	complementary metal-oxide-semiconductor	83
CD	critical dimension	1
FFT	fast Fourier transform	82
FWHM	full-width at half maximum	79
IBT	interband transition	102
IC	integrated circuit	1
IoT	internet-of-things	1
LW	longitudinal wave	64
LLM	large language model	1
NA	numerical aperture	2
NIR	near-infrared	30
OPA	optical parametric amplifier	79
QE	quantum efficiency	30
RCWA	rigorous coupled wave analysis	40
SAW	surface acoustic wave	67
SDG	Synchronous Delay Generator	26
SNR	signal-to-noise ratio	78
SPP	surface plasmon polariton	102
SPR	surface plasmon polariton resonance	78
TIR	total internal reflection	18
TMM	transfer-matrix method	89
TTM	two-temperature model	88
UVFS	UV grade fused silica	30
WLC	white light continuum	79

What was the reason to refer to a significant amount of relatively old papers published in the previous century?

— Reviewer 2
(in response to the submission of the manuscript based on Chapter 5)

ACKNOWLEDGMENTS

NA RUIM VIER JAAR als promovendus te hebben gewerkt zit het er nu dan echt op. Dit had ik natuurlijk nooit in m'n eentje kunnen voltooien, dus ik wil graag nog de mensen bedanken die mij hier gebracht hebben.

Paul, als eerste wil ik jou bedanken, want zonder jou had ik hier nu niet gezeten. Ik wil je graag bedanken voor het vertrouwen dat je vanaf het begin in me had, terwijl ik geen enkele experimentele ervaring had. Vanaf het moment dat ik solliciteerde, wist ik dat ik heel veel van jou kon leren. Nu bijna vijf jaar verder weet ik zeker dat ik heel veel van je heb geleerd. Ik denk dat je, zo ongeveer, de beste promotor bent die je als promovendus kan wensen. Ik wil je dan ook de komende jaren nog heel veel (natuurkunde)plezier wensen!

Arie, graag wil ik je bedanken als mijn co-promoter bij een vakgebied wat toch wat verder van ASML staat. Onze meetings waren voor mij altijd een goed moment om weer even te kijken waar ik precies was, en om leuk over wetenschap of juist ASML te praten!

Klaasjan van Druten, als vaste 'gast' in de groep wil ik jou ook graag bedanken. Je goede vragen bij allerlei presentaties en de prettige gesprekken zal ik niet vergeten. Daarnaast wil ik je ook bedanken voor het doorlezen en beoordelen van m'n proefschrift, als onderdeel van de commissie. Daarbij wil ik ook graag de overige commissieleden, Marcelo Ackermann, Daniel Bonn, Gerard Verbiest en Joris van Wezel, van harte bedanken voor hun deelname aan de commissie.

Ook wil ik graag Irwan Setija en Stephen Edward bedanken, als contactpersonen van ASML hebben jullie niet alleen veel bijgedragen aan (de richting van) het onderzoek, maar hebben jullie ook wat leuke onderzoeksprojectjes opgestart. Ook heb ik veel geleerd van jullie hoe het onderzoek in een bedrijf is geörganiseerd.

Guido, je bent misschien al even weg, maar ik ben je nog steeds erg dankbaar! Zonder jou had ik dan ook niet zo'n vliegende start gehad, zelfs met mijn initiëel beperkte experimentele ervaring. Je wist me in een mum van tijd te leren hoe de goede, oude Astrella te bedienen en hoe de TOPAS uit te lijnen. Daarnaast was het ook heel gezellig in en buiten het lab, ondanks de vreemde coronasituatie.

Ester, wat heb ik ook veel geluk gehad met jou in de groep! Met veel plezier kijk ik terug op de vele goede gesprekken die we hebben gehad, over van alles en nog wat. Ook was ik erg blij dat jij *wel* voetbal volgde en op maandag dan ook graag de wedstrijden van het afgelopen weekend wilde nabespreken, ondanks dat je voor die club uit Amsterdam bent. Ik wil je dan ook veel succes wensen bij je volgende stap in de academische wereld in de mooie stad Amsterdam!

Lorenzo, old buddy! It is sad to have seen you leave the Netherlands, but I am very glad that you also are a dr. now! I will miss the coffees we have drunk and the foosball we played. I wish you the best in Rome!

Christoph. For about 2 years, you were the group 'kiddo'. Now you are the most experienced around, how fast the tables turn. I will never forget the 'let's start early with a 1.5 hour coffee break', that we had many times... The discussions on optics, lasers, physics, whatsoever, I will miss them!

Sonia, I still remember your first days, how unsure you were with the old laser, and how quickly that improved. Then, the new laser came and you were the expert, showing everyone how to operate it!

Paul Cannon, I couldn't have been more lucky that you joined, right after Ester left. Another football fan! Besides that, I was also glad to have worked together, unfortunately only for a short time. I feel confident that you handle the Astrella just as well as I have, and I am curious to see the results from your work!

Sarah, ondanks dat je als laatste in de groep bent gekomen, bracht je al vanaf het eerste moment een geweldige energie met je mee! Ik heb dan ook veel vertrouwen dat je zonder problemen je onderzoek zal kunnen doen, ondanks dat je een scheikundige achtergrond hebt.

Thomas Meijvogel, altijd handig, zo'n naamgenoot die nota bene onderdeel is van dezelfde groep. Veel dank voor al je bijdragen in het lab en voor de gezelligheid daarbuiten! Sebastiaan Heerooms, als opvolger van Thomas heb ik je helaas niet lang meegemaakt, maar ik weet zeker dat je de rol als technicus van de groep zeer goed zal vervullen. Natuurlijk kan ik de overige technici niet vergeten: Stefan Lehmann, Arend-Jan, Bartjan, Laurens en Nik. Dank voor de gezelligheid bij de lunches en de hulp in het lab!

Joost, zonder jou was ARCNL er nu niet geweest, dus daar wil ik je heel veel voor bedanken. Daarnaast wil ik je ook bedanken voor de zorg dat het instituut bij elkaar bleef, tijdens de coronaperiode. Wim, als nieuwe directeur was het niet makkelijk om in de voetsporen van de eerste directeur te treden. Het was inspirerend om te zien hoe je binnenkwam en in mum van tijd toch een nieuwe sfeer wist neer te zetten. Veel dank voor de vele gesprekken en je betrokkenheid. Marjan, dit is al vaker, maar zeker nog niet vaak genoeg, gezegd. Zonder jou zou ARCNL er niet zijn! Ik wil je dan ook heel erg bedanken voor al je werk, waarvan een groot gedeelte niet zichtbaar is voor de ARCNL-collega's. Ook de andere groepsleiders van ARCNL wil ik bedanken, jullie drive en kennis, maar ook de interesse in de projecten van anderen, maken het instituut uniek.

Celine, Jusra, Jet, Ellen en Marja, als secretariaat zorgden jullie voor goeie dosis humor en gezelligheid op ARCNL, naast dat jullie ook alles draaiende hielden.

Tot slot wil ik nog de collega's van de AMOLF-supportafdelingen bedanken en in het bijzonder: Marco Seijnen, voor het schrijven van de meetautomatisatie en het integreren van de hardware in het lab! Bob en Igor, heel erg bedankt voor alle hulp in de cleanroom!

Next, I would like to thank my (former) co-workers, with whom I shared the most beautiful office at ARCNL: Maksym, Matthijs, Maisie, Fengling, Matthias, Augustas, Aaron (from Stefan's Witte group), and Parikshit (I'm still not sure how you ended up in our office, but I liked it). I enjoyed our many conversations, work-related and work-unrelated, the beautiful Christmas tree (from November until February), the (unfinished) office calendar, which I think would still be worth it. It is sad to see that, like me, many of you have already left, and the rest will soon be gone as well.

I would also like to thank the colleagues from the HHG group: Sylvianne, Maarten, Nataliia, Zhonghui, Manos, Leo, Francesco, Kevin, Roy, Pieter, Thorben, Brian, and Tanya. Thanks for all the random chats when I was bored and just went into your office. Sylvianne, what a surprise it was that you were also attending CLEO 2023 in San Jose! Nataliia, I wish you the best at ARCNL, for now, and where you will continue with your work! Thanks also Zhonghui, for the interesting work we did together, also for the foosball and the many talks! I wish you all the best with your family in the Netherlands!

Also, I would like to thank the people who joined me in participating in the OR: Roland, Zhouping, Ellen, Stan, and Dion. I enjoyed working with you to improve the working conditions, and make ARCNL a little bit better!

The former Foosball buddies: Jan Matthijssen, Zeudi, Lucas, thank you for the good foosball times and the interesting talks! Reynolds, I have to say that I really enjoyed seeing you adapt to the best foosball tactics, 0 aiming, 10000 power. Also, many thanks for the good advices and nice talks. Many thanks Ester PP for all the weird chats, many beers and laughs. To all other colleagues from ARCNL, whom I forgot to name, I also thank you, since without *all* of you, the institute would not be as it is! I already miss you!

Vervolgens wil ik mijn paranimfen Matthijs Velsink en Thomas Edridge bedanken voor hun tijd en geduld. Matthijs, het was altijd heerlijk met jou te kunnen klagen over zure reviewers, (zelfgeschreven) matige Pythoncode, kapotte apparatuur, bureaucratie en noem maar op. Ook was de trip naar Taiwan een onvergetelijk succes! Thomas, wat is het mooi dat jij ook een PhD bent gaan doen! Het eindeloze geklaag (wederom) deed me erg goed, net als de vele memes, biertjes, pasta's en sciencefiction meuk.

Dank voor de mannen van Club Volt uit Delft, zonder was dit niet mogelijk geweest! Heel veel dank voor alle mooie feestjes, borrels, uitjes en reizen, voor jullie support en enthousiasme, voor het proberen te begrijpen van wat ik nu eigenlijk aan het doen ben. Ook wil ik Bestuur 85 bedanken, al vanaf ons bestuursjaar hebben we een zeer goede band en dat heeft zeer vele mooie avonden, maar ook serieuze gesprekken opgeleverd! Mark Weijerman en Thomas Edridge, veel dank dat ik jullie huis als m'n tweede thuis mocht gebruiken! Ik hoop dat jullie het net zo leuk vonden als ik. Marc Bathelt, als een van m'n oudste vrienden kan je natuurlijk ook niet ontbreken. Dank voor alle steun en alle biertjes die we samen hebben genuttigd! Jan Karel en Ward, heel veel dank voor de leuke tijd op de JP Heijestraat!

Als laatste wil ik m'n ouders en familie bedanken. Mijn vader Jan, mijn bonusmoeder Wil, mijn moeder Martine en bonus-vader Jan-Willem, jullie wil ik graag bedanken voor wie ik nu ben, zonder jullie was ik hier niet geweest. Ook wil ik m'n bonusfamilie bedanken, Paul en Cathelijne, Caroline en Hugo (en de kids), Remco, Ilona en Can.

Pap, zonder jou had ik nooit de studie natuurkunde gekozen, maar wat was dat (achteraf) een goede keuze! Mijn liefde voor natuurkunde en techniek heb ik dan zeker ook van jou. Met je enthousiasme en interesse voor mijn onderzoek vond ik altijd een luisterend oor bij jou. Mam, van jou heb ik dan misschien wat minder natuurkunde geërfd, maar wel net zo goed liefde voor de cijfers! Daarnaast wil ik je ook bedenken voor een rotsvast vertrouwen mij, tijdens elke stap die ik maak.

COLOPHON

This thesis is typeset using a modified version of typographical look-and-feel `classicthesis` developed by André Miede and Ivo Pletikosić. The style is inspired by Robert Bringhurst's seminal book on typography *The Elements of Typographic Style*. The body text is set in 9 pt TEXGyre (TG) Pagella.

This thesis is printed by ProefschriftMaken.nl on 115 g m^{-2} Silk MC paper. The cover is printed on 250 g m^{-2} Sulphate cardboard.

The front cover is a measurement of the change in reflectance of a 35 nm ruthenium film on crystalline silicon, following a 400 nm pump pulse, as a function of wavelength (vertical) and pump-probe delay time (horizontal) in an alternative colour map. The data is acquired using the same experimental setup as described in Chapter 6. The temporal resolution is 25 fs per pixel and the spectral resolution is about 0.2 nm per pixel.

The back cover is a modification of Figure 6.2b, set in the same colour map as the front cover, but in a slightly different scale.